

## ABSTRACT

SANDUKAS, STEFAN. Development and Analysis of Bioactive CaP Coatings for Biomedical Implants. (Under the direction of Dr. Afsaneh Rabiei.)

Hydroxyapatite ( $\text{Ca}_{10}(\text{PO}_4)_6(\text{OH})_2$ , HA) and other calcium phosphate coatings have been established as being highly effective for enhancing bone-bonding to orthopedic and dental implants. Commercially-produced HA coatings exhibit weak adhesion to substrate surfaces as well as poor mechanical properties, arising from a non-homogeneous microstructure. This research investigates the development of improved HA coatings on metallic and polymeric substrates by physical vapor deposition methods.

In the preliminary study, functionally-graded hydroxyapatite coatings doped with silver (FGHA-Ag) on titanium substrates, deposited by ion beam assisted deposition (IBAD), were studied in terms of microstructure, dissolution behavior and biological response. It was determined that release of Ag from FGHA-Ag coatings was controlled by the functionally graded microstructure, with Ag being released rapidly at first and gradually decreasing. FGHA-Ag1 and FGHA-Ag2 coatings, with 1 and 3 wt% Ag respectively, were found to promote optimal osteoblast attachment and growth, whereas FGHA-Ag3 coating was determined to exhibit toxicity to osteoblast cells, as a result of high Ag content (6.6 wt%). It was concluded that optimal Ag-doping is between 1 and 3 wt%, in order to release Ag at a sufficient rate to produce an antibacterial effect, while maintaining an Ag concentration that does not inhibit growth of osteoblast cells.

The main focus of this research has been on development and optimization of crystalline HA coatings on polymer (polyetheretherketone, PEEK) substrates. As PEEK is a relatively new biomaterial, bioactive-coating of PEEK is not well studied and has yet to be optimized. HA coatings were deposited by RF magnetron sputtering in order to produce thin, well-adhered coatings with uniform, homogenous microstructures. Due to the amorphous nature of sputtered HA films and the temperature sensitivity of PEEK, lower temperature heat treatment methods of HA crystallization were explored, and yttria-stabilized zirconia (YSZ) was used as a thermal barrier coating between the PEEK substrate and the HA coating.

The dual-layer coating of approximately 1.2 $\mu$ m, consisting of a YSZ layer of  $\sim$  450nm and an HA layer of  $\sim$  750nm, initially exhibited an average adhesion strength of 15.1 MPa to the PEEK substrate. Plasma activation of the PEEK substrates before deposition resulted in an increase in coating adhesion strength to 33.4 MPa, which is significantly higher than that of existing HA-coated PEEK materials.

Microstructural and compositional analysis by SEM and XRD revealed that the YSZ layer exhibited a crystalline structure as-deposited, with columnar-shaped grains oriented along the growth direction, while the HA layer was amorphous as-deposited. Post-deposition heat treatments of hydrothermal, laser and microwave annealing were studied for the purpose of forming a crystalline HA coating layer, which is necessary in order to provide long-term stability of the coating. Of the three methods, microwave annealing was determined to be the most effective, producing a crystalline HA microstructure without causing damage to the PEEK substrates or weakening the adhesive or cohesive strengths of the coating. SEM observation of the coating cross-

sections revealed that after microwave annealing, the HA coating exhibited a columnar crystalline microstructure, similar to that of the underlying YSZ crystalline layer. It is suggested that the existence of the crystalline YSZ layer aids in the formation of the HA layer upon heating. SEM-EDX showed that the HA coating layer has a Ca:P ratio close to that of stoichiometric HA, before and after crystallization, while FTIR revealed that the HA is hydroxyl-deficient, indicating a need for water vapor exposure, either during or after heat treatment. Finally, culture tests showed a significant increase in initial cell attachment and growth on microwave-annealed coating surfaces, suggesting that this surface is more stable and provides increased surface area for cell attachment compared with uncoated PEEK and amorphous HA surfaces.

© Copyright 2012 by Stefan Sandukas

All Rights Reserved

Development and Analysis of Bioactive CaP Coatings for Biomedical Implants

by  
Stefan Sandukas

A dissertation submitted to the Graduate Faculty of  
North Carolina State University  
in partial fulfillment of the  
requirements for the degree of  
Doctor of Philosophy

Mechanical Engineering

Raleigh, North Carolina

2012

APPROVED BY:

---

Dr. Afsaneh Rabiei  
Chair of Advisory Committee

---

Dr. Carl Koch

---

Dr. Gracious Ngaile

---

Dr. Alexei Saveliev

## DEDICATION

To my family, especially my mom, brother and grandmother!

## BIOGRAPHY

Stefan Sandukas was born in Raleigh, North Carolina in 1981. He received his Bachelor's and Master's degrees from the Materials Science and Engineering Department at North Carolina State University in December 2002 and December 2005, respectively. Starting in August 2006, he joined Dr. Rabiei's research group, the Advanced Materials Research Laboratory (AMRL), and has enjoyed learning to approach real world problems from a multidisciplinary perspective, incorporating aspects of materials science, mechanical and biomedical engineering. Stefan will begin his new job as a semiconductor process engineer at Intel in New Mexico in August 2012.

## ACKNOWLEDGEMENTS

First and foremost, I would like to express my deep gratitude to Dr. Rabiei, my research adviser, for her continued support, advice and patience over the last several years. Without her sincere encouragement and excellent advice, this research would have been impossible. Dr. Rabiei's dedication to her students is inspirational and has enriched my life as I have had the opportunity to conduct research at national laboratories both in the US and overseas.

I would like to offer my sincere thanks to my committee members Dr. Koch, Dr. Ngaile, Dr. Saveliev and Dr. Kuznetsov for their valuable time and advice in completing this work.

I am pleased to acknowledge the National Science Foundation for the financial support (Grant No: CMMI - 0600596 and IREE - 0738365 ) and Oak Ridge National Laboratory for access to the research facilities of the Center for Nanophase Materials Sciences (CNMS) and the Shared Research Equipment user facility (SHaRE), (Grant No: CNMS-2005-070 and CNMS-2007-096). Special thanks to Dr. Laura Edwards, Dr. Christopher Rouleau, Dr. Andrew Payzant, Dr. Jason Fowlkes, Dr. Dale Hensley, Dr. Darrell Thomas, and Dr. David Joy for their training and assistance in completing the research at ORNL.

I would like to sincerely thank Dr. Yamamoto for her advice and hospitality as I conducted research in the Biometal Group, within the National Institute for Materials Science (NIMS) in Tsukuba, Japan.

I was fortunate to have access to the research facilities of the Nanofabrication Facility (NNF) and Analytical Instrumentation Facility (AIF) at NCSU. Special thanks to Dr. Marcio Cerullo and Mr. Henry Taylor of the NNF, as well as Dr. Roberto Garcia and Mr. Chuck Mooney of the AIF, who were of great help to me for their assistance and training.

Thanks also go to all the members of our research group including former graduate students Dr. Xiao Bai and Dr. Lakshmi Vendra, and current graduate students Mr. Matias Garcia Avila and Ms. Shuo Chen for their friendship, assistance and suggestions in completing this work. I would like to thank Mr. Rufus Richardson and Mr. Mike Breedlove at machine shop for their assistance in manufacturing tools for our experiments, as well as the MAE staff of the main office for their help in processing the orders and shipping associated with this project.

Finally, I wish to thank my family and friends for their unconditional support and encouragement, without which I could never have reached this awesome moment.

# TABLE OF CONTENTS

LIST OF FIGURES .....	ix
LIST OF TABLES.....	xiii
LIST OF ABBREVIATIONS.....	xiv
CHAPTER 1: INTRODUCTION .....	1
1.1. Spinal deformities, diseases and instability.....	1
1.2. Biomedical implants used in spinal fusion procedures .....	2
1.3. Biocompatibility .....	7
1.4. Materials used in spinal fusion cages.....	11
1.5. Hydroxyapatite coatings.....	14
1.5.1. Functionally Graded Hydroxyapatite (FGHA) Coatings.....	16
1.5.2. Hydroxyapatite coatings doped with antibacterial agents .....	19
1.6. Yttria-stabilized zirconia intermediate layer .....	20
1.7. Deposition of HA/YSZ bilayer coating by RF magnetron sputtering.....	21
1.8. Crystallization of hydroxyapatite coating on PEEK.....	24
1.9. Objectives .....	28
CHAPTER 2: LITERATURE REVIEW.....	30
2.1. PEEK.....	30
2.1.1. Physical and chemical properties of PEEK.....	31
2.1.2. Processing of PEEK.....	37
2.1.3. Mechanical properties of PEEK.....	41
2.1.4. PEEK composites.....	44
2.1.5. Resistance to radiation, elevated temperature, and chemical sterilization .....	48
2.1.6. Imaging Properties.....	50
2.1.7. Biocompatibility of PEEK .....	53
2.1.8. PEEK in spinal implants.....	57
2.1.9. Plasma activation of PEEK surfaces.....	60
2.2. Bioactive coatings .....	62
2.2.1. Hydroxyapatite coatings.....	63
2.2.2. Commercially-produced hydroxyapatite coatings.....	66
2.2.3. Experimental methods of applying HA coatings.....	69
2.2.4. Bioactive coatings on PEEK substrates .....	75
2.2.5. Yttria-stabilized zirconia in bioactive coatings.....	78
2.2.6. Low temperature crystallization of Hydroxyapatite Coatings .....	86
2.3. Summary .....	92

CHAPTER 3: FUNCTIONALLY-GRADED HYDROXYAPATITE COATINGS WITH AG-DOPING ON TITANIUM SUBSTRATES.....	94
3.1. Introduction.....	94
3.2. Materials and Methods.....	95
3.2.1. Preparation of Titanium substrates.....	95
3.2.2. Processing of Coatings .....	96
3.3. Analysis of FGHA-Ag coatings .....	101
3.3.1. TEM Analysis of coatings.....	101
3.3.2. Cell detachment study.....	101
3.3.3. Measurement of shear force necessary to detach a cell from surface.....	103
3.3.4. Measurement of cell adhesive area.....	105
3.3.5. Cell Count .....	106
3.3.6. Cell Viability Study .....	107
3.3.7. Silver Release Test .....	107
3.3.8. Surface Profilometry.....	109
3.4. Results.....	110
3.4.1. TEM of coating and coating/substrate interface .....	110
3.4.2. Evaluation of cell affinity to coating surfaces by cell detachment shear force measurement.....	113
3.4.3. Cell culture assay .....	115
3.4.4. WST-1 Assay .....	120
3.4.5. Ag release test.....	121
3.4.6. Surface Roughness .....	122
3.5. Discussion .....	123
3.6. Summary .....	126
CHAPTER 4: HYDROXYAPATITE COATINGS ON PEEK SUBSTRATES .....	128
4.1. Introduction.....	128
4.2. Materials and Methods.....	129
4.2.1. Preparation of PEEK substrates.....	129
4.2.2. Plasma activation of PEEK substrates .....	132
4.2.3. Conditioning of sputtering targets before use .....	134
4.2.4. Radio Frequency Magnetron Sputtering System.....	135
4.2.5. Coating Deposition.....	136
4.2.6. Post-deposition heat treatment of coatings.....	140
4.3. Analysis techniques .....	142
4.3.1. Determination of deposition rate .....	142
4.3.2. Coating adhesion strength .....	145
4.3.3. Optical Microscopy.....	147
4.3.4. X-ray diffraction.....	147
4.3.5. Scanning Electron Microscopy.....	148
4.3.6. Scanning Electron Microscopy with energy dispersive X-ray (EDX).....	148
4.3.7. Fourier transform infrared spectroscopy .....	149

4.3.8. Cell Culture Tests.....	149
4.4. Results.....	150
4.4.1. Deposition Rate.....	150
4.4.2. Physical and Mechanical Properties.....	155
4.4.3. Optical Microscopy.....	158
4.4.3. Microstructural Observation.....	167
4.4.5. Compositional Analysis.....	175
4.4.6. Biological Response.....	182
4.5. Discussion.....	184
4.6. Summary.....	191
CHAPTER 5: CONCLUSIONS.....	193
CHAPTER 6: SUGGESTIONS FOR FUTURE RESEARCH.....	197
REFERENCES.....	198

## LIST OF FIGURES

Figure 1-1.	Spinal fusion cage (PROT Lumbar Cage manufactured by Merries International Inc.) .....	4
Figure 1-2.	Spinal fusion cage inserted between two vertebrae in the lumbar spine ...	5
Figure 1-3.	Cross-sectional image of human vertebra.....	10
Figure 1-4.	Fluorescent images of HEPM cells cultured for 24 h on FGHA coating (right) compared with Ti control (left). Stains: DAPI-Nucleus (Blue), FITC-Actin (Green), TRITC-6,4 Integrin (Orange-Red).....	18
Figure 1-5.	Schematic diagram of RF Magnetron sputtering process.....	24
Figure 2-1.	PEEK molecular repeat structure .....	32
Figure 2-2.	Polymerization Reaction of PEEK.....	32
Figure 2-3.	PEEK orthorhombic unit cell .....	35
Figure 2-4.	DSC Trace of PEEK-OPTIMA LT-1 rod .....	36
Figure 2-5.	Injection-molded PEEK component .....	41
Figure 2-6.	SEM Image of PEEK/HA composite fracture surface .....	47
Figure 2-7.	Radiograph of titanium spinal fusion cage inserted between two lumbar vertebrae .....	51
Figure 2-8.	Radiographs (a,b) and CT scans (c,d) of anterior cervical fusion using PEEK fusion cage.....	53
Figure 2-9.	Plasma-spray apparatus used in depositing HA coating onto carbon-fiber reinforced PEEK substrates .....	67
Figure 2-10.	SEM micrograph of plasma-sprayed HA coating/Ti interface .....	68
Figure 2-11.	SEM images of HA coating deposited onto Ti substrates by pulsed laser deposition: a) cross-sectional view; b) top view of coating surface .....	72

Figure 2-12. SEM images of Ti/HA coating on CFR-PEEK (a) cross section, (b) top view .....	78
Figure 2-13. Structure zone model (SZM) for sputtered thin films .....	83
Figure 2-14. SEM Image of YSZ coating cross-section .....	85
Figure 3-1. Image of IBAD system at ORNL .....	97
Figure 3-2. Diagram of IBAD chamber and components.....	98
Figure 3-3. Custom-built stainless steel substrate holder for Ti substrates .....	99
Figure 3-4. Example of force–displacement curve obtained from detachment of a single cell adhered to coating surface .....	104
Figure 3-5. Series of images captured from video during cell detachment process. Tip comes into contact with cell (A) shear force is applied to cell as X-Y stage is moved right (B) cell is fully detached as tip has moved across cell adhesive area (C).....	104
Figure 3-6. Linear regression for silver content vs. absorbance at 550nm.....	109
Figure 3-7. TEM cross-sectional micrographs of FGHA-Ag1, FGHA-Ag2 and FGHA-Ag3 coatings .....	111
Figure 3-8. Summary of cell detachment shear force measurements, showing average shear force (normalized by cell adhesive area) applied to cells to detach from the surface .....	113
Figure 3-9. Optical micrographs of sample surfaces A) FGHA coating (top left), B) FGHA-Ag1 coating (top right), C) FGHA-Ag2 coating (bottom left), and D) FGHA-Ag3 coating (bottom right) after 24-hour cell culture .....	116
Figure 3-10. Optical micrographs of sample surfaces A) FGHA coating (top left), B) FGHA-Ag1 coating (top right), C) FGHA-Ag2 coating (bottom left), and D) FGHA-Ag3 coating (bottom right) after 4-day cell culture .....	117
Figure 3-11. Optical micrographs of sample surfaces A) FGHA coating (top left), B) FGHA-Ag1 coating (top right), C) FGHA-Ag2 coating (bottom left), and D) FGHA-Ag3 coating (bottom right) after 7-day cell culture .....	118

Figure 3-12. Average number of MC 3T3 osteoblast cells counted on each of coating surface at different incubation times.....	119
Figure 3-13. Relative viability of cells by WST-1 assay .....	120
Figure 3-14. Release of Ag <sup>+</sup> ions from each of the Ag-doped FGHA coatings immersed in USP water over time.....	121
Figure 3-15. Surface roughness average (R <sub>a</sub> ) of each coating surface measured before and after immersion in culture medium. ....	122
Figure 4-1. PEEK rods of 1 ft length and ½” diameter before cutting.....	130
Figure 4-2. PEEK substrates of ½” diameter, ¼” height .....	131
Figure 4-3. Grinding and polishing station (Buehler) .....	131
Figure 4-4. Sonic cleaner (Buehler).....	132
Figure 4-5. RF plasma barrel reactor.....	133
Figure 4-6. Hydroxyapatite sputter target [Kurt J. Lesker Co.] .....	134
Figure 4-7. Ytria-stabilized zirconia sputter target [Kurt J. Lesker Co.].....	135
Figure 4-8. Image of RF Magnetron Sputtering system at NNF Cleanroom NCSU.....	138
Figure 4-9. Image of inside of RF Magnetron Sputter Chamber.....	139
Figure 4-10. Surface Profilometer (Veeco Dektak 150).....	144
Figure 4-11. Schematic diagram of stud-pull coating adhesion tester.....	146
Figure 4-12. Image of stud-pull coating adhesion tester.....	146
Figure 4-13. HA deposition rate vs. RF Power .....	151
Figure 4-14. HA deposition rate vs. Time .....	152
Figure 4-15. Coating thickness vs. time for YSZ and HA targets.....	154
Figure 4-16. Plot of plasma treatment time versus coating adhesion strength .....	157
Figure 4-17. Coating pull-off area for fully delaminated coating.....	160

Figure 4-18. Coating pull-off area for partially delaminated coating.....	160
Figure 4-19. Optical micrograph of as-deposited coating top surface .....	162
Figure 4-20. Optical micrograph of microwave-annealed coating top surface .....	163
Figure 4-21. Optical micrograph of coating removal caused by microwaving.....	164
Figure 4-22. Optical image of coating ablation by KrF laser .....	165
Figure 4-23. Optical image of top coating surface after microwave anneal.....	166
Figure 4-24. SEM Image of as-deposited YSZ/HA coating and PEEK substrate .....	167
Figure 4-25. SEM Image of as-deposited YSZ/HA coating cross-section .....	169
Figure 4-26. SEM images of A) YSZ and B) HA coatings separately .....	170
Figure 4-27. SEM image of HA/YSZ coating cross section after hydrothermal treatment .....	172
Figure 4-28. SEM image of HA/YSZ coating cross section after microwaving.....	173
Figure 4-29. High magnification SEM image of microwave-annealed YSZ/HA coating cross-section.....	174
Figure 4-30. XRD Spectrum of as-deposited YSZ/HA coating on PEEK substrate .....	176
Figure 4-31. XRD Spectrum of 48-hour hydrothermally-annealed YSZ/HA coating ....	177
Figure 4-32. XRD Spectra of HA/YSZ coating after microwave annealing .....	178
Figure 4-33. FTIR Spectra on various surfaces.....	180
Figure 4-34. Initial osteoblast cell attachment to sample surfaces.....	183
Figure 4-35. dsDNA concentration on sample surfaces at day 1 and day 3.....	183

## LIST OF TABLES

Table 1-1.	Mechanical properties of human hard tissue .....	10
Table 2-1.	Typical physical and mechanical properties of PEEK .....	33
Table 2-2.	Properties of medical-grade PEEK resins .....	38
Table 2-3.	Physical and Mechanical Properties of unfilled and CFR-PEEK compared with UHMWPE and PMMA .....	46
Table 2-4.	Selected properties of YSZ thermal barrier coating .....	79
Table 2-5.	Hydrothermal parameter for annealing of HA thin films .....	89
Table 2-6.	Laser parameters for annealing of HA thin films.....	91
Table 3-1.	Deposition parameters for Ag-doped FGHA coatings.....	100
Table 3-2.	Composition of FGHA coatings as determined by XPS .....	101
Table 4-1.	RF Magnetron Sputtering Deposition Parameters.....	137
Table 4-2.	Deposition rates for YSZ and HA coatings .....	154
Table 4-3.	Coating adhesion strength on PEEK substrates of varied surface roughness .....	155
Table 4-4.	Effect of plasma treatment on coating adhesion strength .....	156
Table 4-5.	Coating Adhesion strength before and after heat-treatment methods.....	158
Table 4-6.	Summary of Coating Adhesion Tests .....	161
Table 4-7.	Crystalline peaks identified in as-deposited YSZ/HA coating .....	176
Table 4-8.	Crytalline peaks identified in hydrothermal-annealed YSZ/HA coating..	177
Table 4-9.	Crystalline peaks identified in microwave-annealed YSZ/HA coating .....	178

## LIST OF ABBREVIATIONS

CFR – carbon fiber-reinforced

CT – computed tomography

CVD – chemical vapor deposition

DSC – differential scanning calorimetry

EDX – energy dispersive X-ray spectroscopy

FGHA – functionally-graded hydroxyapatite

FTIR – Fourier transform infrared spectroscopy

HA – hydroxyapatite

HEPM – human embryonic palatal mesenchyme

IBAD – ion beam assisted deposition

MRD – magnetic resonance imaging

ORNL – Oak Ridge National Laboratory

PAEK – poly-aryl-ether-ketone

PEEK – poly-ether-ether-ketone

PET – poly-ethylene-terephthalate

PLD – pulsed laser deposition

PLLA – poly-L-lactic acid

PMMA – poly-methyl-methacrylate

PS – poly-styrene

PVD – physical vapor deposition

SEM – scanning electron microscopy

TEM – transmission electron microscopy

XPS – X-ray photoelectron spectroscopy

XRD – X-ray diffraction

## CHAPTER 1: INTRODUCTION

### 1.1. Spinal deformities, diseases and instability

Back pain is now one of the most prevalent and costly health problems in the world, resulting in more lost productivity than any other medical condition [1,2,3]. Approximately 85% of people in the United States report having back pain at some point in their lives [4]. Although many instances of back pain are temporary, chronic back pain is an increasing problem; one study reports that patients suffering from chronic back pain increased from 3.9% to 10.2% between 1992 and 2006 [5]. Conditions causing such problems include degenerative disc disease, spinal disc herniation, discogenic pain, spinal tumor, vertebral fracture, scoliosis, kyphosis (Scheuermann's disease), spondylolisthesis, spondylosis, posterior Rami Syndrom, and other degenerative spinal conditions. In all of these conditions, the cause of pain and instability can be traced to one or more problematic spinal segments; a spinal segment consists of two vertebrae, separated by an intervertebral disc.

Approximately 25% of those who suffer from these conditions will undergo spinal surgery. In many cases, the problems arising from an instable spinal segment can be resolved by a procedure known as spinal fusion. Spinal fusion is the surgical immobilization of two or more adjacent bones of the spinal column (vertebrae). Multiple bones are fused or made to grow together to become one solid bone [6]. For spinal fusion procedures specifically, the total number of primary lumbar and cervical

procedures in the United States grew from 121,400 to 281,300 between 1990 and 2003.

The growing need for spinal surgery instrumentation and fixation devices has sparked increased research aimed at advancing materials used in these applications in recent years. As a result of the increased demand, the production of many variations of spinal fusion cages by several implant manufacturers has grown rapidly over the last 20 years; the global market for spine implants has been reportedly increasing at a rate of over 20% per year [7].

## **1.2. Biomedical implants used in spinal fusion procedures**

While implant design and manufacturing technology has improved over the past few years, several problems still exist and failed spinal fusion procedures are not uncommon. Among adults undergoing surgery for spinal deformations, 9% of patients will undergo a subsequent revision procedure at some point in their lives [8]. Common reasons for reoperation include pseudoarthrosis (non-fusion of the two vertebrae often due to an ineffective spinal fusion implant), painful or protruding implants, and implant removal. Because implant failure is one of the primary causes leading to the need for revision surgery, the improvement of current spinal implants can result in a significantly higher success rate in spinal surgery and greatly reduce the costs, health risks and patient discomfort that arises from additional surgical procedures [8].

Spinal implants were developed as early as the 1930s and used in surgical

procedures aimed at stabilizing vertebral segments in order to correct segmental dysfunction or instability. Early spinal implants consisted of pedicle screws and small plates, secured to the two adjacent vertebrae of the problematic spinal segment to limit motion. These screws and fixation plates were metallic, constructed of either stainless steel or cobalt-chromium alloys. While they were successful to a degree in limiting lateral motion, these fixation systems were problematic in that they failed to prevent the unstable spinal segment from experiencing the vertical compression forces transmitted through the spine, and this led to very long recovery times and often to failure of the fusion procedure altogether.

Currently, the primary implant component used in a spinal fusion procedure is the interbody fusion cage. An interbody fusion cage is a prosthesis implanted between unstable vertebrae (in the place of the problematic biological intervertebral disc) to maintain foraminal height and decompression. They are cylindrical or square-shaped devices, and are usually threaded. The modern titanium intervertebral cage was invented by orthopedist and veterinarian, George Bagby. Bagby first developed a threaded stainless steel cage to treat “wobbler’s syndrome” in horses, a condition where cervical spine degeneration produced segmental instability and spinal cord compression, eventually necessitating destruction of the horse [9, 10]. Following successful clinical results in animals, Bagby and other clinicians (including Steven Kuslich, Gary Michelson, and Charles Ray, who came to have fusion cages named after them as well) developed different versions of Bagby's basic design for human

application and began clinical testing in 1989 [9,10]. Based on successful data from these trials, the United States Food and Drug Administration approved these titanium cages for posterior interbody “standalone” use in 1996, and have since also approved these cages for anterior interbody placement [9].

Several varieties of the interbody fusion cage now exist including the Harms cage, Ray cage, Pyramesh cage, InterFix cage, and Lordotic LT cage, all of which are made from titanium; the SynCage, made from Polyetheretherketone, the Brantigan cage, made from carbon fiber; and the Cortical Bone Dowel, which is cut from allograft femur [105]. The cages can be packed with different types of bone graft material in order to promote arthrodesis (joint fusion).



Figure 1-1. Spinal fusion cage (PROT Lumbar Cage manufactured by Merries International Inc.) [11]

The PROT Lumbar Cage (shown above) is just one of many designs of lumbar interbody fusion cages, which are used in the fusion of vertebrae in the lumbar (lower back) region of the spine. As seen in Figure 1-1, spinal fusion cages are often designed with macroscopic surface features, such as threaded columns or ridged surfaces, in order to enhance the mechanical bonding (interlocking) of newly formed bone to the surface of the implant.

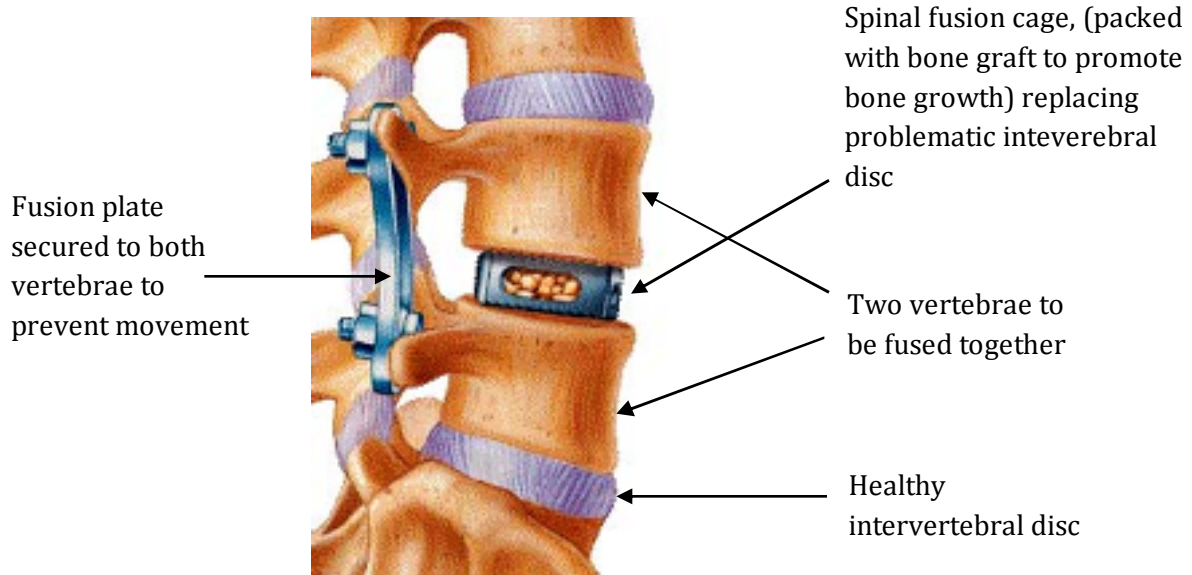


Figure 1-2. Spinal fusion cage inserted between two vertebrae in the lumbar spine [12]

Shown above, the spinal fusion cage is implanted in the place of a deteriorating intervertebral disc during spinal surgery. In many cases, the hollow spinal fusion cage is packed with bone graft to promote bone in-growth and to speed the fusion process between the adjacent vertebrae. A bone graft refers to bone transplanted from a donor

site to a recipient site; the transplanted bone can originate from several different sources including:

**1. Autologous (or autogenous) bone grafting** refers to utilizing bone obtained from the same patient receiving the graft. Bone is harvested from non-essential bones, such as from the iliac crest (pelvic rim), the fibula, the ribs, the mandible and even parts of the skull. Block grafts, in which a small block of bone is placed whole in the area being grafted, most often use autogenous bone because there is less risk of the graft rejection due to the graft originating from the patient's own body [13]. A negative aspect of autogenous bone grafts is that an additional surgical site is required [14].

**2. Allograft bone** is also taken from human bone, however the difference is that allograft is harvested from an individual other than the one receiving the graft. Allograft bone is taken from cadavers that have donated their bone to be used for living people in need of bone transplants. Allograft bone comes in three forms: 1) fresh or fresh-frozen bone; 2) freeze-dried bone allograft (FDBA); 3) demineralized freeze-dried bone allograft (DFDBA) [15].

**3. Artificial bone** can be created from ceramics such as calcium phosphates (hydroxyapatite and tricalcium phosphate), bioactive glasses and calcium sulphate. All of these synthetic bone replacements are bioactive, with different degrees of solubility depending on the physiological environment [16].

### 1.3. Biocompatibility

Besides the mechanical capability of spinal fusion implants to provide load sharing, maintain intervertebral disc height and to withstand deformation in order to allow fusion of an instable spinal segment, a primary requirement of material used in spinal fusion cages is a high degree of biocompatibility. Biocompatibility can be defined as “the ability of a material, device or system to perform without a clinically significant host response in a specific application” [7]. While this term is rather broad, biocompatible materials can be further subdivided into being either *bioactive* or *bioinert*. Bioactive materials are those which positively interact with the surrounding tissue on a biological level, while bioinert materials, on the other hand, produce no biological interaction on their own and are simply tolerated by the surrounding tissue. Most materials which meet the mechanical requirements to be used as implants are only bioinert as a result of their chemical dissimilarity to human tissue. For this reason, a great deal of research is directed towards creating a bioactive surface on these bioinert materials through the use of surface modifications, such as coating with a different, bioactive material.

In order to tailor the surface to be bioactive, it must be designed with respect to a specific biological function. In the field of orthopedic and dental implants, the implant is designed to come into contact with and ultimately bond with bone tissue, thus one must consider the types of cells that are involved with the initial attachment and

formation of new bone. The types of cells that are involved in the formation of new bone are listed below:

**Osteoblasts:** bone-forming cells that produce alkaline phosphatase, an enzyme involved in mineralization of bone, as well as in producing bone matrix proteins.

**Osteoclasts:** a type of bone cell that removes bone tissue by removing its mineralized matrix and breaking up the organic bone. This process is known as *bone resorption*.

These two types of cells, osteoblasts and osteoclasts, are responsible for controlling the amount of bone tissue in the body. Bone is a dynamic tissue, constantly being reshaped and reformed in response to mechanical stimuli, or the lack thereof. Osteoblasts are in charge of production of matrix and mineral, and osteoclasts break down the tissue.

**Fibroblasts** are a type of cell that synthesizes the extracellular matrix and collagen, the structural framework for human tissues. Fibroblasts are the most common cells of connective tissue in animals; they are a type of stem cell that can mature into many other types of cells, including osteoblasts or osteoclasts.

All of these types of cells are critical in the process of *osseointegration* of an implant. **Osseointegration** refers to the biological fixation of the implant to the surrounding bone tissue, which is preferable to a mechanical-only fixation. During osseointegration, implanted components become firmly bonded to host bone by on-growth or ingrowth without the use of bone cement [17,18,19].

The above terms describe the biological compatibility of orthopedic and dental implants. Equally important is the mechanical compatibility of the implant. While many materials are sufficiently strong to meet the mechanical requirements of a specific application, it is critical to select a material that does not greatly exceed the strength and stiffness of the surrounding bone in order to avoid *stress shielding*. **Stress shielding** is a phenomenon by which a higher stiffness implant interferes with normal transmission of applied load, bearing more of the load and reducing the amount of load that surrounding bone would normally experience. This removal of mechanical stimulus results in reduction of density and eventual deterioration of the surrounding bone following *Wolff's Law*, which states that bone constantly remodels itself in response to applied loads [20]. In this aspect, it is detrimental to have an implant of much higher stiffness relative to the adjacent to bone, and so materials must be selected that closely match the mechanical properties of bone are desired. Some of the mechanical properties of human bone are listed in Table 1-1.

Table 1-1. Mechanical properties of human hard tissue

<b>Material</b>	<b>Elastic Modulus (GPa)</b>	<b>Tensile Strength (MPa)</b>
Cortical bone	15-20	130 MPa
Cancellous bone	0.3	15
Enamel	80	11.5
Dentin	20	44

As seen in Figure 1-3, the vertebra is a cellular structure, comprised of a high percentage of cancellous bone; which has very low stiffness. Considering its mechanical properties as a composite material, the vertebrae is quite susceptible to stress shielding.

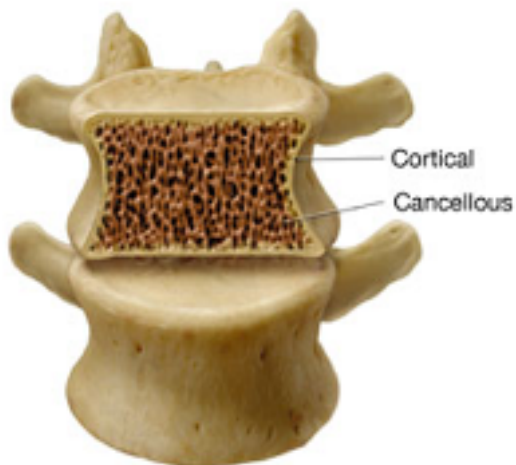


Figure 1-3. Cross-sectional image of human vertebra

#### **1.4. Materials used in spinal fusion cages**

As described previously, the first standalone spinal fusion cages for human applications were developed by George Bagby in 1989 and were constructed of titanium [10]. Throughout the early stages of clinical application and development of varied geometries of the spinal fusion cage, titanium remained the material of choice for construction of the cage. Titanium was initially chosen because of its proven success in orthopedic implants due to its excellent biocompatibility and mechanical properties which are suited for load-bearing applications. Titanium and titanium alloys possess favorable properties of corrosion resistance, biocompatibility (through the formation of a TiO<sub>2</sub> surface oxidation layer), low elastic modulus (compared with other metals) and high strength-to-weight ratio [21]. Titanium is used in several load-bearing orthopedic and dental implants including femoral stems of hip replacements, fracture fixation plates, bone screws and pins, dental posts, and many others. However, in the application of spinal fusion cages, titanium has been shown to have two distinct disadvantages:

- 1. Stiffness mismatch between titanium and human bone;** the high elastic modulus of titanium (~ 100GPa) compared with that of human cortical bone (~ 15 GPa) can cause stress shielding, leading to deterioration of the bone surrounding the implanted titanium cage. This is especially true in the case of spinal implants, where a large volume of the vertebrae are comprised of cancellous bone (elastic modulus ~ 0.3

GPa), a soft, cellular-structured bone that resists shear forces and acts to absorb shock within the spinal column.

**2. The lack of radiolucency of titanium;** titanium, like all metallic materials, is not transparent to radio waves, making radiographic assessment of the degree of bone fusion within the interbody fusion cage a problem for surgeons. Clinical diagnostic imaging tools, including X-rays and computed tomography (CT) scans are obstructed by traditional titanium fusion cages, resulting in the evaluation of arthrodesis (joint fusion) within a titanium cage difficult or impossible [22]. Similarly, titanium produces metallic artifacts in magnetic resonance imaging (MRI). These limitations with respect to clinical assessment during the fusion process represent a significant problem for surgeons and patients, resulting in unnecessarily long recovery times and failure to identify problems with the fusion procedure (mainly pseudoarthrosis) as they occur.

In order to overcome the limitations of spinal fusion cages constructed from titanium, high strength polymer materials have recently been utilized [105]. Traditionally, polymeric materials have lacked the combination of mechanical strength and chemical resistance necessary to be used in load-bearing applications within the body. However, in the last two decades, advances in polymer technology have produced several high-performance thermoplastic resins that meet these requirements, including nylon 6-10, poly-butylene terephthalate (PBT), poly-styrene (PS), poly-etherketone (PEK), poly-etheretherketone(PEEK), and poly-etherketoneetherketoneketone

(PEEK) [105]. Due to a more stable supply and a higher compatibility with reinforcing agents, such as carbon fiber, PEEK became the optimal choice as a polymeric material for use in spinal fusion cages. PEEK possesses numerous characteristics which make it an ideal choice for use as a load-bearing biomedical implant material; an elastic modulus (3.6 GPa) close to that of human bone, high melting temperature (340°C), excellent chemical stability, resistance to radiation used in sterilization procedures, transparency to radiowaves, ability to increase mechanical strength by fiber reinforcement (4~20 GPa, depending on fiber volume fraction), etc. (Further details of PEEK are provided in Section 2.1).

Beginning in the mid-1990s, spinal fusion cages constructed from PEEK and carbon-fiber-reinforced PEEK (CFR-PEEK) were accepted by the FDA for human use and studied in clinical trials. PEEK biomaterials now have almost twenty years of successful clinical history in load-bearing spinal fusion cages and are now being evaluated for further demanding spinal applications such as posterior dynamic stabilization and total disc replacement [105]. While spinal fusion cages are still manufactured from both titanium and PEEK, an increasing number of implant developers have switched their focus from titanium to PEEK. For example, the developers of the Wallis posterior dynamic stabilization system have converted their titanium interspinous component to PEEK [23]. It is expected that with the development of advanced PEEK-based composites, PEEK will completely replace titanium as the bulk material for spinal fusion cages.

## 1.5. Hydroxyapatite coatings

While titanium and PEEK have been shown to possess excellent mechanical properties and chemical stability even in the harshest of conditions, the bioinertness of these materials dictates that they do not actively participate in forming functional chemical bonds with surrounding tissue, as a bioactive material would; therefore recent research has been focused on improving the bioactivity of PEEK implants with respect to osseointegration. Hydroxyapatite (HA)  $[\text{Ca}_{10}(\text{PO}_4)_6(\text{OH})_2]$  and other calcium phosphate coatings have been shown to promote rapid osseointegration on metallic dental and orthopedic implants, which results in faster and superior implant stabilization [24, 25, 26] Hydroxyapatite is preferred in bioactive coatings over other calcium phosphate phases because of its chemical similarity to bone (bone is comprised of approximately 70% of biological hydroxyapatite) and because of its low rate of dissolution. Details of hydroxyapatite are described fully in Section 2.2.1.

While possessing excellent biocompatibility, bulk hydroxyapatite is very brittle due to its ceramic nature, and cannot be used as the primary component of load-bearing implants; therefore, HA is used as a coating on traditional metallic materials such as titanium, cobalt-chromium, and stainless steel, and recently on polymeric materials such as polyetheretherketone (PEEK) to increase biocompatibility. Several studies have demonstrated the effect of hydroxyapatite coatings on improving bioactivity of orthopedic and dental implant surfaces *in vitro* and *in vivo* [27, 28, 29]. HA coatings promote osseointegration by causing bone formation to proceed faster, resulting in

increased bone apposition and increased differentiation of mesenchymal cells to osteoblast cells compared with control surfaces [30]. This is thought to be due to an increase in adsorption and production of proteins on HA surfaces, higher affinity of osteoblast cells to bone-like chemistry of HA, and increased crystal growth and matrix mineralization of osteoblast cells, once attached to the HA surface (due to the presence of Ca and P ions needed to form hard bone mineral) [30].

Hydroxyapatite coatings first received regulatory acceptance for human use in 1991 and have exhibited excellent results from clinical studies since then [31]. Early use of HA coatings in the 1990s was primarily in the application of hip implants; the femoral stem component of the implant, constructed from titanium, was coated with HA using the plasma spray method [31]. The strong fixation between implant and bone that resulted from a greater affinity of bone forming cells, called osteoblasts, to attach to the hydroxyapatite surface compared with bare titanium allowed for implants to be inserted without the use of bone cement to fix the implant in place. Cementless implantation is a preferred option due to the fact that some patients are allergic PMMA bone cement, as well as the recent discovery of *bone cement implant syndrome* (BCIS), in which serious complications can be caused by degradation of bone cement [32].

Plasma spraying is the current commercial method used to produce hydroxyapatite coatings on biomedical implants. Plasma spraying is a process in which melted or partially melted HA powders are sprayed onto the substrate surface by high temperature plasma and become solidified as a coating as the molten HA rapidly cools

onto the substrate surface. This method is used because of its high deposition rate, low cost, and ease of application. Despite concerns about coating delamination, plasma spraying was chosen as the preferred method of coating in the early 1990s because it was an established technology at the time, it was cost-effective, and it was seen as the most easily reproduced approach [31]. Plasma-sprayed HA coatings can promote greater direct bone attachment and improve bonding strength at the bone–implant interface when compared with uncoated titanium implants [33]. However, numerous problems with plasma-sprayed HA coatings have been cited, including weak bonding strength at the coating–metal interface, variation in structural and chemical properties, and nonuniformity in coating density [34, 35]. Because of these limitations, many alternative methods for deposition of HA have been investigated, including radio frequency magnetron sputtering, electron beam deposition, pulsed laser deposition, sol-gel spinning, precipitation from solution, hot isostatic pressing and others. Further description of the methods used to deposit hydroxyapatite coatings is described in Section 2.2.3.

#### **1.5.1. Functionally Graded Hydroxyapatite (FGHA) Coatings**

The Advanced Materials Research Laboratory (AMRL), under the direction of Dr. Rabiei in the Mechanical and Aerospace Department at North Carolina State University (NCSU), has been involved in the research and development of improved hydroxyapatite coatings for biomedical implants since 2004 [36]. As previously

described, crystalline hydroxyapatite is the least soluble of the calcium phosphate phases in physiological fluid and is therefore able to provide the most long-term stability when used as a coating for biomedical implants. However, dissolution of calcium phosphates is beneficial in early stages after implantation in order to provide  $\text{Ca}^{2+}$  and  $\text{PO}_4^{3-}$  ions which accelerates new bone growth. In this aspect, amorphous calcium phosphates are more bioactive than crystalline hydroxyapatite but have poor long-term stability as they become completely dissolved within weeks after implantation, causing the bare implant surface to be exposed to the surrounding body fluid [37]. Due to this competition between long-term stability and initial bioactivity, a CaP coating with uniform crystallinity cannot satisfy both demands. The optimal dissolution behavior of a calcium phosphate coating is one which dissolves rapidly upon initial introduction into the physiological environment and then gradually dissolves more slowly over longer time periods in order to retain a layer of coating on the implant surface. In order to solve this problem, Dr. Rabiei has developed a functionally graded hydroxyapatite (FGHA) coating, which exhibits a mostly amorphous top coating layer, a semi-crystalline middle layer, and a mostly crystalline layer at the substrate surface [33, 38, 39]. This coating is achieved using ion beam assisted deposition (IBAD) with in situ substrate heating in order to form various degrees of crystallinity by adjusting substrate temperature over the course of the deposition. The FGHA coating has been previously studied and optimized in terms of mechanical properties, microstructure and chemical composition, and has demonstrated superior biological

and mechanical properties when compared with commercial plasma-sprayed coatings and HA coatings produced by other methods [63].

The improvement in bioactivity of the FGHA coating compared with commercially pure titanium was measured using cell spreading and immunofluorescence integrin assays, performed using ATCC CRL 1486 human embryonic palatal mesenchyme (HEPM) cells, an osteoblast precursor cell line [40]. It was determined that the FGHA coating promoted increased cell attachment and spreading compared to the pure titanium surface. Shown in Figure 1-4, more HEPM cells are found on the FGHA surface compared with titanium and exhibit a higher degree of spreading of the extracellular matrix, indicating a healthier state.

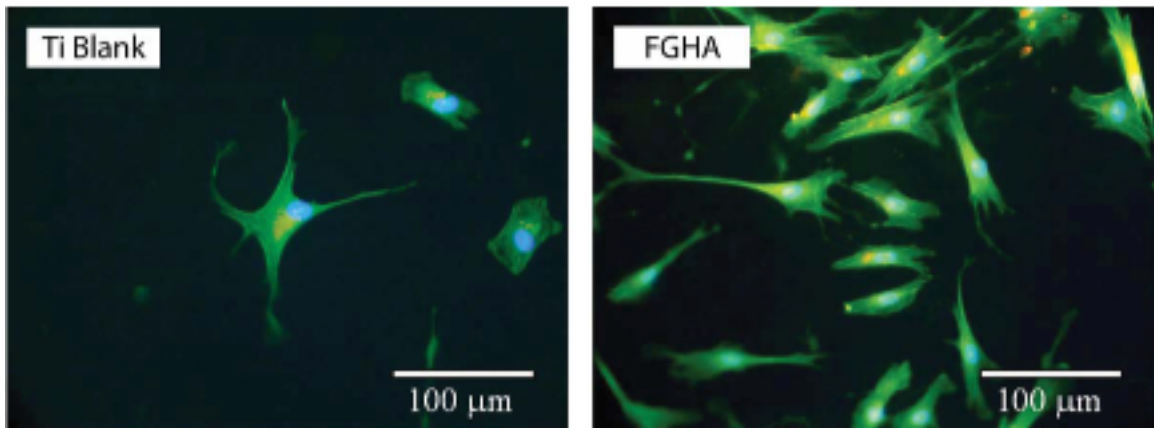


Figure 1-4. Fluorescent images of HEPM cells cultured for 24 h on FGHA coating (right) compared with Ti control (left). Stains: DAPI-Nucleus (Blue), FITC-Actin (Green), TRITC-6,4 Integrin (Orange-Red). [40]

### **1.5.2. Hydroxyapatite coatings doped with antibacterial agents**

Heavy metals such as lead, mercury and silver are known to exhibit a toxic effect on some bacteria, viruses and fungi [41]; among these, only silver is non-toxic (in low doses) to humans. The mechanism by which Ag reduces bacteria is not yet fully understood, but it is thought to involve protein inactivation of the bacterial cells and DNA association, in which Ag ions bond to bacterial DNA and eliminate its ability to replicate [41,42,43]. Silver has been used as an antibacterial agent for many years in applications such as topical gels, wound dressings, surgical masks and textiles.

In the field of biomedical implants, infection represents one of the primary causes for implant failure and subsequent revision surgery [44]. Risk of infection is highest immediately after implantation and gradually decreases within the following weeks. *Staphylococcus aureus* and *Staphylococcus epidermidis* are the two most common strains of bacteria that cause infection after implant surgery, representing approximately 80% of infections following orthopedic implant procedures [44]. Because Ag is known to be toxic to these strains of bacteria, Ag is has been incorporated into bioactive coatings and bone cements for biomedical implants within the last few years [44,45]. For HA coatings specifically, Ag is doped into the coatings by methods of ion exchange, thermal evaporation and co-sputtering, typically in concentrations of less than 10 wt % [44,46].

Recently, the Advanced Materials Research Laboratory (AMRL) at North Carolina State University has expanded upon its successful development of functionally

graded hydroxyapatite (FGHA) coatings by incorporating small percentages of Ag into the FGHA coatings during the deposition process [175,182,40]. The method for producing Ag-doped FGHA coatings has already been established; however, the dissolution behavior and biological response to these coatings still needs further studies. The first part of this research seeks to investigate the dissolution and biological response to the Ag-doped FGHA coatings, as well as to correlate these findings to the compositional and microstructural properties of the coatings.

#### **1.6. Yttria-stabilized zirconia intermediate layer**

Yttria-stabilized zirconia ( $Y_2O_3$  minor component,  $ZrO_2$  major component), or YSZ, while not bioactive, is a biocompatible material that has been used in some studies to improve the mechanical qualities of hydroxyapatite coatings [47,48,49,50]. YSZ, traditionally used as a thermal barrier coating to coat high-temperature components, has been shown to toughen hydroxyapatite coatings when used as second phase material within the coating [47,50], and to increase bond strength of hydroxyapatite coatings when used as a precursor layer, applied directly to the substrate material before the deposition of the hydroxyapatite coating layer [48]. The overall strengthening effect of YSZ when used as a precursor layer and a second phase constituent is reportedly due mainly to three mechanisms: (1) improved mechanical interlocking between YSZ coatings and substrates as compared with HA/substrate; (2) the YSZ intermediate layer provides a rougher, nanoscale surface morphology than a

polished substrate, resulting in stronger mechanical bonding of the subsequent HA layer; (3) when used as a minor phase constituent in the HA coating layer, the YSZ particles serve as a reinforcing agent, increasing toughness of the coating and resulting in increased cohesive strength of the composite coating.

In this research, yttria-stabilized zirconia (7%  $Y_2O_3$  / 93%  $ZrO_2$ ) is proposed as an intermediate layer, between the PEEK substrate and the hydroxyapatite top coating layer. The YSZ layer is expected to provide the following benefits:

1. To provide some degree of heat shielding to the PEEK substrates during post-deposition heat treatments for the purpose of forming a crystalline HA phase in the top coating layer. (Post-deposition heat treatment of the coating will be discussed in Section 1.8).
2. To increase the overall coating adhesion strength to the PEEK substrates as compared with HA coating alone.

### **1.7. Deposition of HA/YSZ bilayer coating by RF magnetron sputtering**

Deposition of the HA/YSZ coating onto PEEK substrates in this research will be accomplished using radio frequency magnetron sputtering, a physical vapor deposition method. Sputtering is a process in which atoms, or molecules, are ejected from a solid material (called a target), due to bombardment of the target by energetic particles (ions, neutral atoms, neutrons, electrons or photons) [51]. Because ions produce the highest number of ejected atoms per collision (called sputter yield), ions are most often used as

the energetic particles to bombard the sputter target in the sputter deposition process. Sputter deposition takes place in a reduced pressure environment (high vacuum chamber) so that ejected atoms condense onto the substrate without being hindered by collisions with other gas molecules. (Further description of sputter deposition in Section 2.2.3)

Among the many techniques available to produce HA coatings, sputtering possesses unique advantages that allow for the highest quality of coatings to be produced with the most control over coating properties. One aspect of sputter deposition that is particularly important in this research is that materials with very high melting points, which would be problematic or impossible to deposit using thermal or electron-beam evaporation, are easily sputtered because they are physically removed by collision, rather than evaporated by heat; hydroxyapatite and YSZ are both ceramic materials with very high melting points ( $\sim 1700^{\circ}\text{C}$  and  $2700^{\circ}\text{C}$ , respectively). Another advantage of sputter deposition specific this research is that it requires no hot parts, which is a necessity due to the relatively low melting point of the PEEK substrates ( $340^{\circ}\text{C}$ ). Sputter-deposited films result in compositions close to that of the sputter target; while this does not ensure that the sputtered film will be crystalline HA, it does provide a calcium phosphate film with a Ca/P ratio close to that of stoichiometric HA. Sputtering has been shown to produce HA films with the higher coating adhesion compared with other methods including dip-coating, electrophoretic deposition, and hot isostatic pressing (HIP) [52]. Sputtered films possess high adherence to substrate

materials for a number of reasons; for one, ion bombardment of the substrates is often used as a “pre-cleaning” step that serves to remove contaminants and adsorbed gases and produces a reactive surface that is more susceptible to atomic bonding; secondly, the heat and impact energy caused by energetic ions striking the surface of the substrate enhances bonding due to increased diffusion of sputtered atoms into the interfacial region; finally, the very thin (usually less than 2  $\mu\text{m}$ ) and dense coatings produced by sputtering are less affected by mismatches in thermal expansion and are also less susceptible to cracking compared with thicker ceramic coatings, due to the presence of fewer large cracks [52].

Magnetron sputtering, used in this research, is a type of sputtering that uses strong electric and magnetic fields to trap electrons close to the surface of the target, resulting in an increased number of ionizing collisions with the sputtering gas (typically an inert gas, such as Argon). The increased ionization of the Ar gas leads to a higher plasma density that can be sustained at lower pressures and ultimately to a higher deposition rate. In order to avoid charge build-up of non-conducting materials, such as HA and YSZ, radio frequency (RF) magnetron sputtering is employed, in which the sign of the anode-cathode bias is switched at a high rate. The RF magnetron sputter process is show schematically in Figure 1-5.

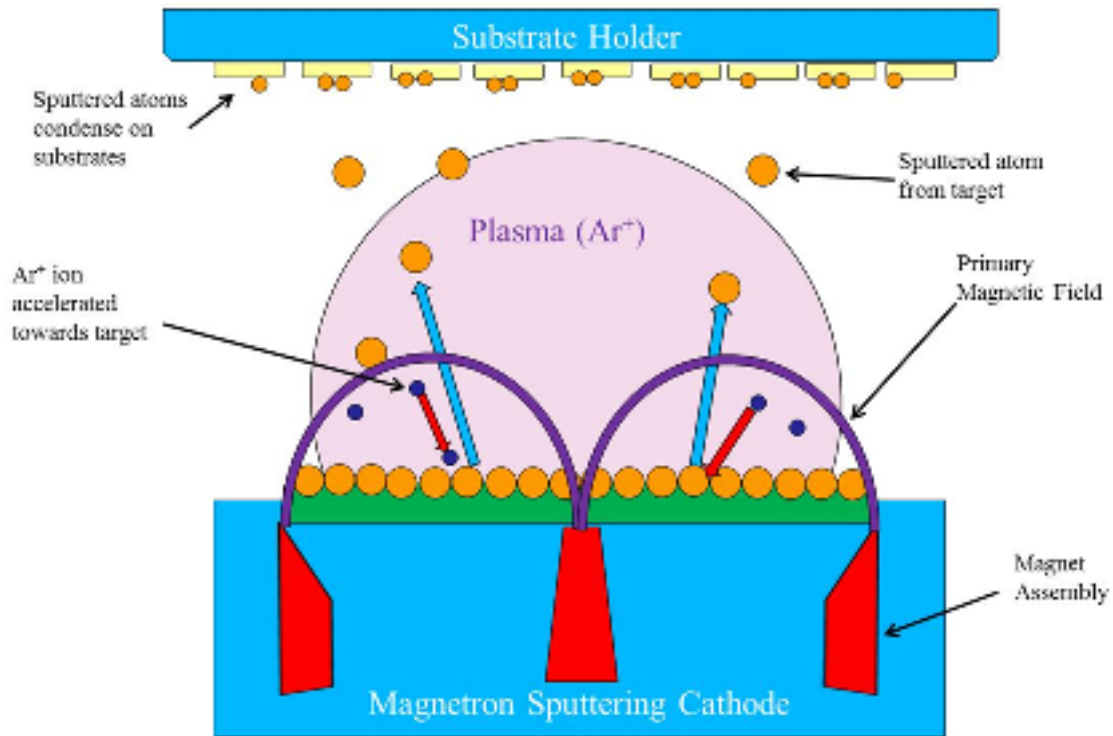


Figure 1-5. Schematic diagram of RF Magnetron sputtering process

### 1.8. Crystallization of hydroxyapatite coating on PEEK

As previously described, crystalline hydroxyapatite is the least soluble of the CaP phases in the body, and is therefore the desired phase for coating of orthopedic and dental implants in order to ensure the long-term stability of the implant. However, hydroxyapatite thin films produced by low-temperature, high vacuum sputtering processes are inherently amorphous (with the exception of some special cases of right-angle magnetron sputtering method, deposited onto single crystal or single phase substrates with preferred orientations) [53]. Therefore, to achieve a crystalline HA

coating layer, a post-deposition heat treatment step is necessary to transform the as-sputtered amorphous HA into crystalline HA (or other crystalline CaP phases).

Traditional crystallization of HA films involves annealing at temperatures above 600°C for at least one hour. Due to the comparatively low melting point of the substrates used in this research (PEEK has a melting temperature of approximately 340°C), conventional oven annealing is not a viable option. To overcome this limitation, three alternative methods for forming crystalline HA are proposed in this study, which have the potential to cause an amorphous → crystalline phase change by either lowering the activation energy necessary for the phase transformation to occur or by selectively heating only the HA coating, leaving the PEEK substrate relatively unheated. The methods which will be attempted are:

**1. Microwave heating** is the result of the absorption of microwave energy by a material exposed to the electromagnetic field distributed within a reflective cavity [54]. Microwave energy refers to non-ionizing electromagnetic radiation with frequencies in the range of 300 MHz to 300 GHz. Microwave heating has several advantages over conventional annealing including uniform heating within homogeneous materials, higher heating rate, and selective heating of materials (the main advantage with respect to this research). The ability to selectively heat materials by microwave radiation is due to the microwave absorption ability of different materials. Based on a “dissipation factor” (ratio of dielectric loss to dielectric constant), a material is classified as transparent, opaque, or absorbing with respect to their interaction with microwaves

[55,56]. Transparent materials allow microwaves to pass through with little or no attenuation; opaque materials reflect microwaves without absorbing; and absorbing materials (dielectrics) absorb and are easily heated by microwaves [55,56]. Based on the electromagnetic absorption characteristics of the coating and substrate materials used in this research (HA is dielectric, YSZ is opaque, and PEEK is transparent), microwave heating appears to be an excellent choice for selective heating of the HA coating in order to cause crystallization [57]. It is expected that that microwave heating can achieve selective heating of the HA coating layer without causing significant heating of the PEEK substrate.

**2. Laser-induced crystallization** is another method that has the ability to cause selective heating, when a short wavelength pulsed laser is used. In a similar manner to materials being heated by absorption of microwaves, materials can be heated through the absorption of certain wavelengths of light radiated by lasers. If pulse duration is sufficiently short (in the range of less than 100 ns), the laser pulses are absorbed in a thin surface region, and the heat is quickly dissipated. [160 ]For the crystallization of thin film coatings on temperature-sensitive materials such as polymers, it is required that the radiation is fully absorbed by the coating in order to avoid significant heating of the substrate; for this application, very short wavelength lasers, such as ultraviolet (UV) excimer lasers are best suited. Laser heating has been shown to cause crystallization of amorphous coatings on polymer substrates without damaging the polymer, as in the case of silicon crystallized on polyethyleneterephthalate (PET) [58]. Similarly,

amorphous calcium phosphate coatings of approximately 250 nanometers produced by sputter deposition were crystallized in HA by pulsed fluorine (F<sub>2</sub>) laser. In this research, crystallization of the amorphous sputtered HA coatings on PEEK substrates will be attempted using a pulsed krypton fluoride (KrF) laser.

**3. Hydrothermal annealing** is a process by which materials are exposed to elevated temperature and water vapor pressure by means of a saturated steam in a pressure vessel, such as an autoclave. As opposed to microwave heating and laser-induced crystallization, hydrothermal annealing is an alternative heating method which can cause crystallization of hydroxyapatite at lower temperatures by lowering the activation energy required for the amorphous to crystalline phase change to occur. Activation energy is lowered by the combination of elevated temperature and high pressure water vapor. This is proposed to result from replenishment of missing OH groups with surrounding H<sub>2</sub>O molecules; HA thin films produced by high temperature processes or high vacuum processes tend to be hydroxyl-deficient detracting from their ability to form crystalline HA [61]. Previous studies have demonstrated that hydrothermal treatment, at temperatures of 200°C or below, was effective in forming crystalline HA coatings from amorphous CaP coatings produced by plasma-spraying and sputtering methods [59,60,61,62]. (Hydrothermal annealing mechanism is described in further detail in Section 2.2.6.1). In this research, hydrothermal annealing will be attempted using an industrial autoclave.

## 1.9. Objectives

The objectives of this project are two-fold:

1. Initially, functionally graded hydroxyapatite coatings doped with silver as an antibacterial agent deposited on titanium substrates which have been previously developed and optimized [63] are to be evaluated in terms of microstructure, release of silver ions and biological response, including antibacterial effect and culture tests. Specific tests will include osteoblast cell count, cell attachment shear force measurement, silver release profile, antibacterial test and cell viability tests.
2. The second objective, and primary focus of this project, is to process bioactive hydroxyapatite coatings on polyetheretherketone (PEEK) substrates in order to improve biocompatibility of PEEK implants used in spinal surgery. The coatings will be processed using a physical vapor deposition (PVD) method; more specifically, radio-frequency magnetron sputtering. Due to the fact that hydroxyapatite coatings produced by physical vapor deposition are inherently amorphous, the coatings will be heat treated after deposition, using an alternative heat treatment method to ensure that the crystalline hydroxyapatite structure is achieved without causing damage or degradation to the underlying PEEK substrates.

These expected benefits will be evaluated using various tests. The mechanical properties of the coating will be measured using a coating adhesion stud pull-off test. The microstructure and crystalline features of the coating will be evaluated using scanning electron microscopy (SEM) of the coating cross sections. The microstructure and phase constituents will be evaluated by X-ray diffraction (XRD). The composition of coating will be quantitatively evaluated by X-ray photoelectron spectroscopy (XPS) and scanning electron microscopy equipped with energy dispersive spectroscopy (SEM-EDS). Finally, culture tests will be performed to evaluate the bioactivity, antibacterial effect, and cytotoxicity of the functionally graded coatings samples

## CHAPTER 2: LITERATURE REVIEW

### 2.1. PEEK

Many types of polymeric materials are used in medicine, each having its own set of properties, making them suited to specific applications. Poly-ether-ether-ketone (PEEK) is a polymer with the molecular formula  $-(\text{C}_6\text{H}_4\text{-O-C}_6\text{H}_4\text{-O-C}_6\text{H}_4\text{-CO})\text{-}_n$  belonging to the subcategory of homopolymers. Homopolymers are composed of repeating units of only one molecular segment (or monomer), taking the form (A-A-A-A), as opposed to copolymers, made from more than one type of monomer and taking the form of (A-B-A-B), where A and B represent different monomers. Because PEEK is made up of many of these monomer units, the average molecular weight is high and varies between 80,000 and 120,000 grams per mole [64]. PEEK is a relatively new high performance polymer, belonging to the chemical family of PAEK resins.

Polyaryletherketones (PAEK) resins are a class of high performance polymers used in joint replacements and other long term implants due to their high chemical and mechanical resistance. PEEK, first synthesized in 1978, was initially used as specialty polymer in very few applications, such as in aerospace moldings and in aircraft and turbine blades (as a fiber-reinforced composite), due to its high cost; however, a stable supply and increasing number of providers has led to its use in other high-tech applications in electronic and automotive industries. Finally, following its recognition as a biomaterial in the early 1990s, PEEK began being used in the medical industry and

is now the leading candidate for replacing metallic components in load-bearing biomedical implants, especially in orthopedic applications [64]. Currently, medical grade PEEK-OPTIMA® is manufactured by Invibio® and is used in the development of “implantable medical devices and pharmaceutical applications having blood or tissue contact for more than 30 days” [65]. Previously, “PEEK-Optima LT” (LT stands for long-term implantation) was produced by Victrex [65,68]. This material has been approved by the Food and Drug Administration (FDA) and is USP Class VI approved [68].

### **2.1.1. Physical and chemical properties of PEEK**

Implantable-grade PEEK, also known as PEEK-OPTIMA®, is a semi-crystalline thermoplastic that possesses superior strength, stiffness and toughness, compared with other biocompatible polymers, while being able to retain these properties through repeated sterilization procedures by steam, radiation and chemical methods [65]. Thermoplastics are polymers that soften or melt when heated and harden when cooled. Thermoplastic polymers consist of long polymer molecules that are not connected by cross-links; thermosets, on the other hand, are polymers which are permanently cured when heated, forming crosslinks that prevent them from being softened or remelted upon heating. Thermoplastics are often supplied as granules and heated to permit fabrication by methods such as molding or extrusion. Besides PEEK, other thermoplastics include polyethylene, polypropylene, polystyrene, polyester, polyvinyl chloride, acrylics, nylons, spandex-type polyurethanes, and cellulose.

The repeat unit in the molecular chain of PEEK consists of two ether groups followed by a ketone group, written as  $-(\text{C}_6\text{H}_4\text{-O-C}_6\text{H}_4\text{-O-C}_6\text{H}_4\text{-CO-})_n$  and shown in chemical notation below:

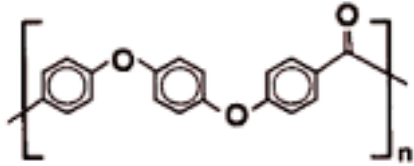


Figure 2-1. PEEK molecular repeat structure [66]

The PEEK polymer is formed by a method known as “step-growth polymerization,” and is the product of the dialkylation of bisphenolate salts [66]. A typical reaction of this type is that of 4,4-difluorobenzophenone with the disodium salt of hydroquinone, which is generated in situ by deprotonation with sodium carbonate. This reaction is shown below:

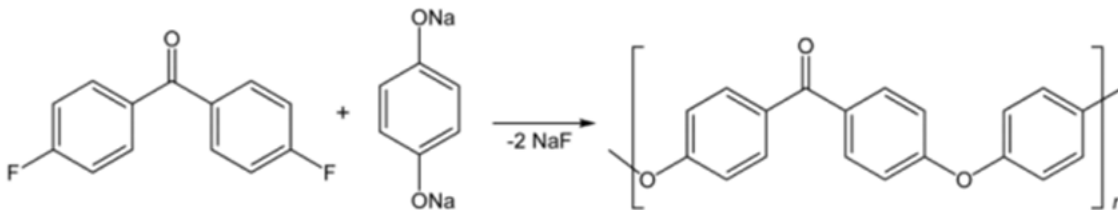


Figure 2-2. Polymerization Reaction of PEEK [67]

The reaction takes place in polar aprotic solvents (such as diphenylsulfone) at a temperature of around 300 °C [67].

The ASTM standard (ASTM F 1579 “Standard Specification for Polyaryletherketone (PAEK) Resins for Surgical Implant Applications”) classifies the chemical and mechanical properties of PAEK, to which PEEK belongs. Typical properties of PEEK are given in the table below:

Table 2-1. Typical physical and mechanical properties of PEEK [68]

<b>Property</b>	<b>Value</b>
Density (g/cm <sup>3</sup> )	1.32
Elastic Modulus (GPa)	3.7
Tensile Strength (MPa)	100
Elongation (%)	Up to 60
Melting Temperature (°C)	334

PEEK is classified as a semicrystalline polymer because it has an amorphous phase and a crystalline phase; typically it consists of about 30-35% crystallinity, but this varies depending on thermal processing. For example, compression molded PEEK materials typically have a higher degree of crystallinity, resulting in a higher elastic modulus, tensile strength and hardness, while being less ductile and tough than lower-crystalline forms.

Crytallization of polymers is a process in which the molecular chains partially align, forming parallel rows. The molecular chains fold together to align and form regions of like-oriented chains called lamellae, which compose larger spheroidal structures named spherulites [69]. Polymers can crystallize due to cooling from the melt, mechanical stretching or solvent evaporation. The degree of crystallinity, or percentage of crystalline regions of the polymer, affects its optical, mechanical, thermal and chemical properties. This degree of crystallinity can be estimated by analytical methods such as differential scanning calorimetry (DSC), X-ray diffraction (XRD), infrared spectroscopy and nuclear magnetic resonance (NMR). In most cases, polymers at room temperature have a degree of crystallinity within the range of 10 to 80%, having both crystalline and amorphous regions, and so are called “semicrystalline.” PEEK crystals consist of very thin lamellae (50-60 Å) that can organize and form large spherulites (25-40 μm) under certain conditions [70]. Shown in Figure 2-3, PEEK molecular chains align to form crystalline regions, characterized by an orthorhombic unit cell:

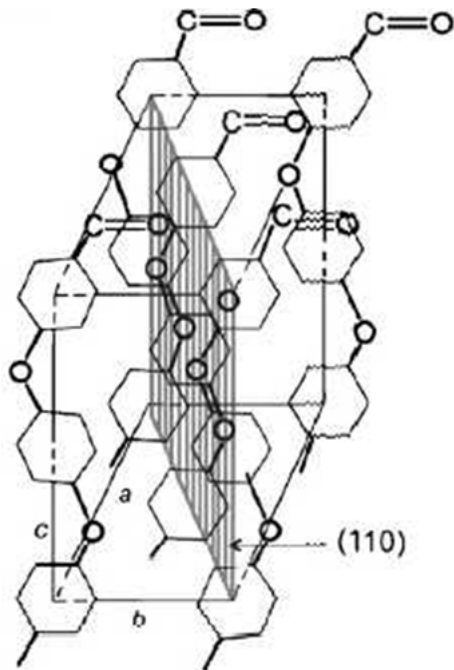


Figure 2-3. PEEK orthorhombic unit cell [105]

As previously mentioned, PEEK usually consists of 30 to 35% crystallinity, however crystalline content can vary between 0 and 40%, depending on its thermal processing [105]. For example, purely amorphous PEEK films can be formed by supercooling thin samples ( $t < 1\text{mm}$ ) by quenching from the melt into cold water [71]. Similarly, amorphous PEEK regions (called “amorphous skins”) are also seen on the outer surfaces of injection-molded components, when the mold is cooled too quickly from the melt [105].

PEEK and other polyaryletherketones are processed using common commercial techniques of extrusion or molding at temperatures between 390°C and 420°C, allowing for complex geometries to be formed [105]. The use of compression or injection

molding facilitates construction of PEEK spinal implants without the need for an extra machining step. PEEK has a glass transition temperature of approximately 143°C; the glass transition temperature in polymers refers to the temperature above which molecular chains are able to slide past one another, resulting in a softer, rubbery polymer, whereas below the glass transition temperature, the material is hard and rigid. Thermal properties of polymers are typically measured using differential scanning calorimetry (DSC), which measures the amount of heat need to cause a temperature change within a material.

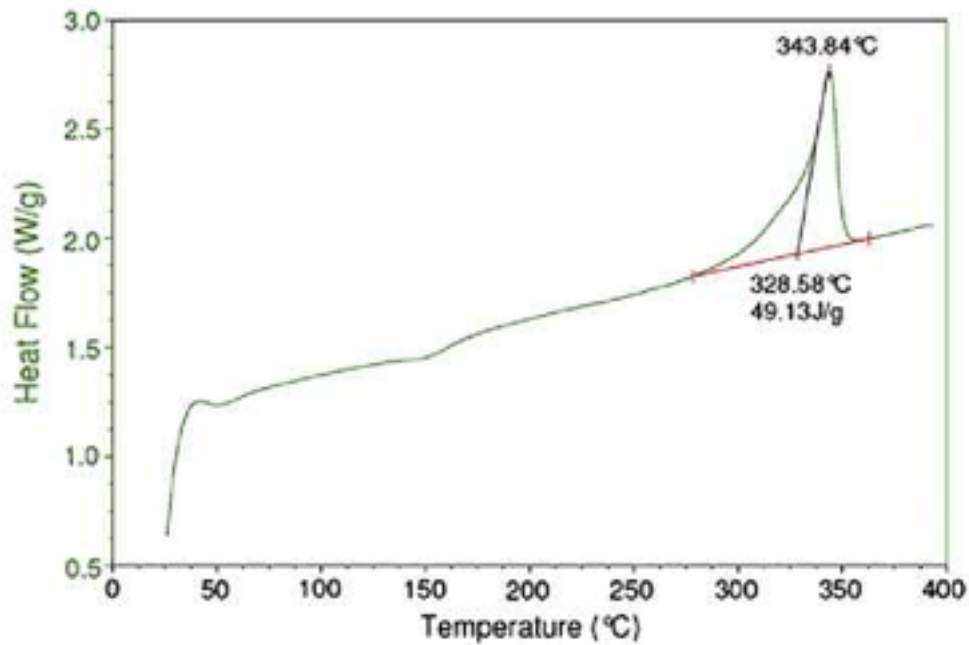


Figure 2-4 DSC Trace of PEEK-OPTIMA LT-1 rod [64]

A DSC trace of PEEK (shown in Figure 2-4) displays its thermal properties of glass transition temperature,  $T_g$ , which separates the “glassy” and “rubbery” regimes, and the melt temperature,  $T_m$ . The glass transition temperature at approximately 143°C, can be seen by the change in slope of the heat input/temperature curve; the melting point, at approximately 340°C, can be observed as a large spike, corresponding to the isothermal phase change from solid to liquid. Mechanical properties of PEEK refer to its behavior at temperatures below the glass transition temperature.

PEEK in its “natural”, non-reinforced form has a light tan or beige color in appearance, which make it aesthetically more compatible than metallic materials for biomedical applications such as exposed dental implants and components of prosthetic limbs. Carbon-fiber reinforced PEEK has a darker, grey appearance, which becomes darker with increasing volume fractions of carbon fiber.

### **2.1.2. Processing of PEEK**

The polymerization of PEEK, shown in Figure 2-3, produces the PEEK resin, referring to pure PEEK powder. Resins for medical-grade PEEK, or PEEK-OPTIMA®, is manufactured under strict quality-control procedures to meet ISO standards 9001:2000 and 13485:2003 in a cleanroom environment in order to reduce the risk of contamination of the raw materials and to ensure consistency among resin suppliers [64]. Once produced, the resin can then be compacted into small pellets, granulated, or left in powder form. The resin is supplied to manufacturers of PEEK in one of these

forms, depending on the processing that will be used, and is categorized based on its molecular weight and flow characteristics; it is necessary to know these factors in order for the manufacturer to select a suitable raw material for a specific forming process. Grades of resin, and their respective applications, are shown in Table 2-2.

Table 2-2. Properties of medical-grade PEEK resins [64]

<b>Property</b>	<b>450 PEEK Resin</b>	<b>381 PEEK Resin</b>	<b>150 PEEK resin</b>
<b>Invibio® PEEK designation</b>	Optima LT1	Optima LT2	Optima LT3
<b>Melt flow index</b>	3.4	4.5	36.4
<b>Molecular weight</b>	115,000 g/mol	108,000 g/mol	83,000 g/mol
<b>Grade characteristics/ Applications</b>	General purpose grade; majority of machining and injection molding processes	Reduced viscosity and good melt strength; used in extrusion of thin-walled parts	Lowest viscosity; used in injection molding of thin-walled parts

The resin (powder, granules or pellets) is then processed into a solid component using either extrusion, injection molding, or compression molding, depending on the desired shape and properties of the final product.

### **2.1.2.1. Extrusion**

Extrusion describes the process of pushing or drawing a material through a die of fixed cross-section [72]. Extrusion is used in the production of PEEK rods, plates and fibers. During the extrusion process, PEEK granules or pellets are fed into a heated screw assembly that melts the raw material and pressurizes the melt; the molten PEEK is then forced through a heated die and then slowly cooled along the extrusion line [64]. This process can be carried out using conventional extrusion equipment and dies and is advantageous in terms of producing PEEK components with a very low variation of crystallinity percentage within different areas of the final product due to uniform heating. Extrusion is more commonly used to produce PEEK rods or plates that are subsequently machined into a final shape and used in medical devices, rather than for the production biomedical implants themselves [64].

### **2.1.2.2. Compression Molding**

Compression molding is a production method in which a preheated material is placed into an open mold cavity and then enclosed by the top mold piece, or plug, which supplies enough pressure to ensure material contact with the mold on all surfaces.<sup>73</sup> The mold pressure is maintained during the cooling stage until the piece has cured, which requires a relatively long time compared with previously described forming methods. Advantages of compression molding are low cost and ability to mold large, intricate parts; however, drawbacks of inconsistency within products and the long cycle

time required limit its use to low-volume products, prototyping, and production of large, industrial components with thick cross-sections [64].

### **2.1.2.3. Injection Molding**

Injection molding is a process used in the production of both thermoplastic and thermosetting plastic materials in which the resin is fed into a heated barrel, mixed, and forced into a mold cavity, where upon cooling, it hardens in the shape of the cavity [73]. Once hardened, additional steps are usually required to obtain the exact shape desired, including trimming of cylindrical sprue, radial runners and extra flashing. Injection molding is capable of producing highly detailed parts, limited only by the design of the mold itself. The initial design and production of a detailed mold is a costly aspect of this technique, therefore injection molding is not used in the production of prototype parts or low-volume pieces; it is used in mass production of PEEK implant component, once a final design has been chosen [64].



Figure 2-5. Injection-molded PEEK component [64]

Due to the variation in thickness across different areas of an injection-molded component, rates of cooling cannot be uniform for all regions of the part, which can result in variation of crystallinity within the solidified product; as seen in Figure 2-5, amorphous regions (lighter colored areas) can result within an injection-molded part due to rapid cooling. In order to prevent the rapid cooling that leads to this problem, mold temperatures must be precisely controlled and monitored.

### **2.1.3. Mechanical properties of PEEK**

As mentioned previously, the mechanical properties of PEEK are dependent on its molecular weight, degree of crystallinity, and volume fraction of fiber reinforcement

(if any). As such, it is necessary to know the resin grade, thermal processing history and fiber content in order to predict the mechanical behavior of a PEEK component.

Talbott et al. measured the mechanical properties of both unfilled and carbon-fiber reinforced (CFR) PEEK as a function of percentage of crystallinity using PEEK 150 powder resin as the raw material [74]. Samples of unfilled and CFR-PEEK were formed with crystallinities ranging from 0 to 40% by cooling from a melt at different rates. As expected, tensile strength, shear strength and compressive strength were increased by increasing the crystallinity of both the unfilled and CFR PEEK. In the unfilled samples, the elastic modulus was increased from 510 ksi (3.52 GPa) to 630 ksi (4.62 GPa) when crystallinity percentage was increased from 16 to 39%; shear modulus was increased from 175 ksi (1.21 GPa) to 205 ksi (1.41 GPa) over the same range [74]. Fiber-reinforced PEEK specimens were also formed with PEEK 150 powder resin as the matrix material and had a fixed fiber volume fraction of 58%. Shear modulus of the CFR-PEEK specimens increased from 710 ksi (4.90 GPa) to 780 ksi (5.38 GPa) over a similar range of crystallinity; the crystallinity increase of the CFR-PEEK samples had less of an effect on strengthening due to the fact that the PEEK matrix only comprised 42% of the total composite volume. In contrast, the fracture toughness decreased significantly in both types of samples with an increase in crystallinity. For unfilled PEEK samples, fracture toughness decreased from 10.4 ksi\*in<sup>1/2</sup> (11.54 MPa\*m<sup>1/2</sup>) to 2.6 ksi\*in<sup>1/2</sup> (2.86 MPa\*m<sup>1/2</sup>) as crystallinity was increased from 16 to 39%; similarly, fracture toughness of CFR-PEEK samples decreased from 4.3 ksi\*in<sup>1/2</sup> (4.72 MPa\*m<sup>1/2</sup>)

to 3.2 ksi\*in<sup>1/2</sup> (3.52 MPa\*m<sup>1/2</sup>) [74]. From these data, the authors were able to formulate relationships for several mechanical properties with respect to crystallinity content of PEEK, useful over the range of 0 to 40% crystallinity.

Recent studies on 450 G (granule) PEEK material have investigated the plastic deformation behavior of PEEK samples at large strain values [75]. It was observed that unfilled PEEK has good ductility and is able to undergo large plastic deformation in both uniaxial tension and compression. At strain values below 0.03 PEEK exhibits a linear stress-strain slope; as strain is increased, there is a clear transition at the yield point, beyond which PEEK undergoes strain hardening and elongation over 50% at room temperature [75].

Experimental and finite element analysis experiments have established that PEEK-OPTIMA is a suitable material for load-bearing implants in the human body. While many of these studies describe the ability of carbon fiber reinforced-PEEK implants to perform in load bearing implants, few have investigated the use of non-reinforced (unfilled) PEEK in these applications. One recent study evaluated the performance of non-reinforced PEEK using quasi-static compressive testing, creep testing in simulated physiological environment and finite element analysis (FEA) in which spinal fusion cage geometries and materials (PEEK and Titanium) were compared [76]. An axial compressive stress of 10 MPa was chosen for the nominal load in the creep test based on finite element analysis findings of the stress state present in PEEK intervertebral cages during daily activities. PEEK samples experienced an average

creep strain of less than 0.1% after 2000 hours of loading. Finite-element analysis demonstrated that while maximum strain on adjacent vertebrae due to insertion of a spinal fusion cage is more dependent on cage design than on material, PEEK spinal fusion cages resulted in slightly lower strain values than similar titanium cages.

#### **2.1.4. PEEK composites**

The elastic moduli of human cortical bone in the longitudinal and transverse directions are typically reported in the range of 16–23 and 6–13 GPa, respectively [77]. The ability of a load-bearing implant to share applied stresses equally with surrounding bone and to transfer load continuously depends on how closely its mechanical properties are to those of the surrounding bone. PEEK, which exhibits an elastic modulus of 3.6 GPa, is much more closely matched to human bone than titanium, whose elastic modulus is approximately 100 GPa. However, with the use of reinforcing agents, PEEK biocomposites have been produced with elastic moduli that can be tailored to match exactly the stiffness of human bone. Several studies have shown that the stiffness and strength of PEEK can be increased with fiber reinforcement.

The most common form of PEEK composite is that of PEEK reinforced with carbon fiber. Since the introduction of PEEK as a biocompatible material, numerous studies have investigated the effect of various lengths, volume fractions and orientations of carbon fiber reinforcements on the mechanical properties, wear behavior and biological response on medical grade PEEK [64,65,107,108]. As described,

the purpose of strengthening PEEK is to raise its stiffness value to that of human bone, in order to provide a continuous, even load transfer between PEEK implants and adjacent bone; for example, PEEK may be modified with the addition of short carbon fibers to increase the elastic modulus from approximately 4GPa to approximately 18GPa and tensile strength from 100MPa to 230MPa of the base polymer [65]. Higher strength and stiffness values can be achieved by using longer fibers and higher volume fractions [74,105]. As is the case with most strengthening mechanisms, the increase in elastic modulus, tensile and shear strengths of PEEK by fiber reinforcement has a negative impact on its ductility and fracture toughness [74]; however, ductility and toughness are not decreased to an unacceptable level with normal volume fractions of fiber reinforcement.

While significantly weaker than titanium fusion cages of the same design, carbon-fiber reinforced cages exhibit sufficient mechanical strength to maintain disc space between vertebrae during the fusion process, and have shown to perform equally well in clinical trials [78].

A summary of the mechanical properties of medical-grade PEEK material without fiber reinforcement, with 30% carbon fiber (chopped) and with 68% carbon fiber (continuous), compared with ultra-high molecular weight polyethylene and polymethylmethacrylate is shown in Table 2-3.

Table 2-3. Physical and Mechanical Properties of unfilled and CFR-PEEK compared with UHMWPE and PMMA [105]

Property	Unfilled PEEK	30 % CFR-PEEK	68 % CFR-PEEK	UHMWPE	PMMA
Molecular weight (g/mol)	80,000-120,000	80,000-120,000	80,000-120,000	$2 \times 10^6$ - $6 \times 10^6$	100,000-800,000
Specific Gravity	1.3	1.4	1.6	0.93-0.95	1.2
Elastic Modulus (GPa)	4	20	135	0.8-1.6	1.5-4.1
Tensile Strength (MPa)	93	170	> 2,000	39-48	24-49
Elongation (%)	30-40	1-2	1	350-525	1-2

As can be seen from Table 2-3, the strength and strength-to-weight values for unfilled PEEK are already considerably higher than similar biocompatible polymers, and with the addition of carbon fiber reinforcement, PEEK composites can achieve strengths similar to titanium. Initially there were concerns about negative effects of carbon fiber released from composites containing short or chopped fibers on the response surrounding cells [79], but several studies have since shown that wear particles from CFR-PEEK have no toxic effect on cells and caused no adverse tissue reaction in concentrations commonly encountered in clinical applications [80].

A relatively new area of research in PEEK composites is the incorporation of HA particles with the goal of simultaneously adding strength and improving the biocompatibility of PEEK and providing a degree of porosity for new bone in-growth [81,82,83,84]. Shown in Figure 2-6, PEEK can be filled with up to 40% HA particles using injection molding without interfering with the crystallization behavior upon cooling [81-84]. However, HA and other calcium phosphate have low affinity for PEEK surfaces which contributes to a poor interface between the PEEK matrix and the HA (or other CaP) particles or fibers; this phenomenon leads to a deterioration in strength of the composite with increased volume fractions of HA [84,86]. Also, the increase in bioactivity of these PEEK composites is debatable, with some studies showing an increase in bioactivity *in vitro* [81,85], while others have shown no increase in human osteoblast attachment compared with a pure PEEK surface [84,86].

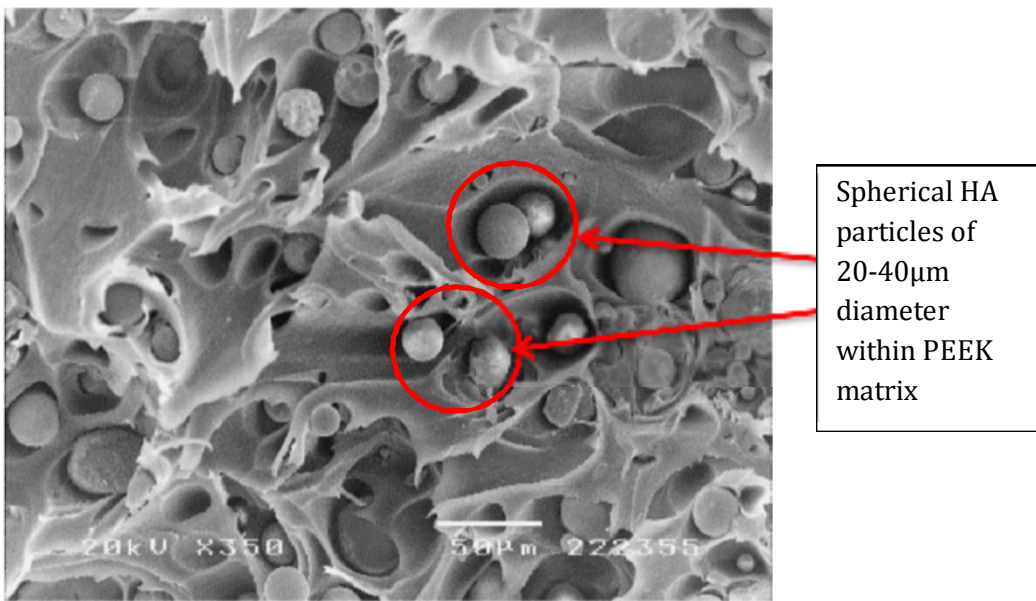


Figure 2-6. SEM Image of PEEK/HA composite fracture surface [86]

### **2.1.5. Resistance to radiation, elevated temperature, and chemical sterilization**

Long term stability of biomedical implants depends not only on their mechanical durability, but also on their ability to withstand exposure to sterilization procedures and physiological environments with degrading as well. This requires that implant materials be resistant to radiation, harsh chemicals and elevated temperatures. PEEK exhibits excellent stability in relation to these scenarios due its naturally unreactive chemical structure [105].

The physiological environment, in which biomedical implants spend their entire service life, is extremely harsh in terms of causing degradation of many materials. Body fluid is a highly oxygenated saline electrolyte solution with a pH of approximately 7.4 and a temperature of 98.6°F (37°C) [87]. The many types of salts contained in body fluid are highly corrosive to metals, and the addition of high ionic and protein concentrations can also be deleterious to many materials in terms of mechanical, chemical and electrical properties. PEEK, however, due to its “resonance stabilized chemical structure”, contains delocalized high orbital electrons along the entire macromolecule, causing it to be extremely chemically stable; for example, PEEK is not damaged by any solvents, with the only exception being highly concentrated (98%) sulfuric acid.

One of the most common sterilization procedures for the both medical equipment and biomedical implants is exposure to steam for time periods of 15 minutes up to an hour using an autoclave. PEEK is described as having a maximum

temperature for long-term use of 240°C [89]. PEEK has been shown to be unaffected by the normal steam sterilization procedure [88]. Several studies have proven that PEEK retained its original properties after steam sterilization for 2500 hours or after 3000 autoclaving cycles at temperatures between 100 and 150°C [89]. Even long term hot air sterilization at 204°C, which is well above its glass transition temperature, had no negative effect on the mechanical properties of PEEK [89].

PEEK is also highly resistant to ionizing radiation, which is another method of sterilization used in the medical industry. Radiation stability is a common concern with biocompatible polymers, such as UHMWPE, which are susceptible to bond cleavage during irradiation, which produces macroradicals (also called “free radicals”) [90]. Usual radiation sterilization doses are between 2 and 4 kGy. A recent study on PEEK has shown that it degrades only slightly at a radiation dose of 5000 kGy, much higher than its expected exposure [91]. Similarly, repeated sterilization with gamma radiation at doses between 25 and 40 kGy was confirmed to produce no measurable changes to the mechanical properties of both PEEK and CFR-PEEK, suggesting that PEEK and PEEK composites may be sterilized by gamma irradiation in air. Another study measured the release of volatile products and radicals by PEEK and other polymers when exposed to gamma radiation using the electron spin resonance (ESR) spectroscopy method and gas analysis [92]. It was found that PEEK (and other polyaryletherketones) are considerably more resistant to gamma radiation at temperatures from ambient

temperature up to the glass transition temperature compared with other types of polymers [92].

#### **2.1.6. Imaging Properties**

Besides the high elastic modulus of titanium which can lead to stress shielding when used as a spinal implant, the primary drawback of using spinal fusion cages constructed from titanium is the difficulty of evaluating the degree of fusion using radiographic methods due to the non-transparency, or “radiopaqueness”, of titanium. The ability to determine whether or not arthrodesis (spinal fusion) has been achieved when radiopaque devices, such as titanium fusion cages, are used has been debated over recent years. [93,94] In contrast to titanium, one of the most important properties of PEEK with respect to its use in orthopedic implants is its radiolucency. In diagnostics, as well as in post-operative inspection, it is important to be able to observe the recovery process using non-invasive imaging techniques such as X-ray, computed tomography (CT) and magnetic resonance imaging (MRI). Metal implants interfere with imaging using X-rays as the metal casts a shadow over the area of importance, and similarly in CT-imaging, metal implants create artifacts, making it difficult or impossible for the surgeon to inspect the implanted area. MRI is not suitable with metal implants either due to the presence of the strong magnetic field [65,95] The use of PEEK implants eliminates these imaging obstacles as PEEK is transparent to X-rays, produces no artifacts in CT images and is non-magnetic, allowing the use of MRI. Because of its

radiolucency, as well as the ability to strengthen PEEK to the levels of bone's mechanical properties, PEEK implants are being considered as replacements in many areas where titanium or cobalt-chromium alloys have been traditionally used.

A study using experimental data from radiographs and computer tomography (CT) scans from cadaver specimens demonstrated that while some level of radiographic determination is possible when titanium fusion cages are used, the metallic artifacts present in the scans considerably obscured observations [93]. Another recent study surveyed a panel of spinal experts (researchers and surgeons) and found that the panel was unable to agree on whether or not arthrodesis was successful after insertion of a titanium spinal fusion cage [94].



Figure 2-7. Radiograph of titanium spinal fusion cage inserted between two lumbar vertebrae [96]

Shown in Figure 2-7, a threaded titanium spinal fusion cage used in a lumbar fusion procedure blocks observation of the intervertebral space by x-ray imaging [96].

In contrast, when PEEK spinal fusion cages are used, arthrodesis is easily determined using radiographic observation [97]. In a clinical study of patients with cervical disc disease, anterior cervical discectomy with interbody fusion (ACDF) was performed, using PEEK cages packed with allograft material in order to fuse together the instable vertebrae. Figure 2-8 displays X-ray images (a,b) and CT scans (c,d) of successful arthrodesis in a patient 12 months after ACDF. The bone growth between the two cervical vertebrae is clearly visible. The PEEK fusion cage cannot be seen in either the radiographs or the CT scans, with the exception of the radiographic markers (seen in images a and b) that are purposely incorporated into the PEEK cages in order to view implant alignment after the procedure.

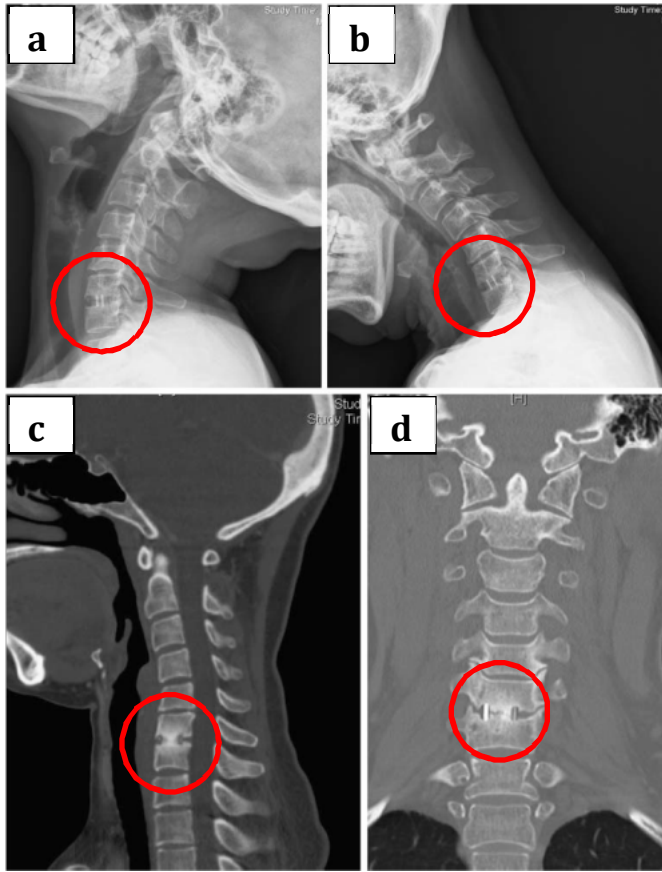


Figure 2-8. Radiographs (a,b) and CT scans (c,d) of anterior cervical fusion using PEEK fusion cage [97]

### 2.1.7. Biocompatibility of PEEK

PEEK-OPTIMA devices have been cleared by the FDA since the 1990s and are being researched in several applications for long-term implants [68]. It is currently being used in the development of finger implant stems, femoral stem prosthesis, acetabular cups, prosthetic hips, spinal cages, suture anchors, ligament fixation

washers, and bone screws and pins [68]. Prior to FDA approval, several clinical studies demonstrated the biocompatibility of PEEK both *in vivo* [98,99] and *in vitro* [100,101].

The response of fibroblasts (a type of cell found in connective tissue throughout the body that produces collagen and other proteins) and osteoblasts (bone-forming cells) to PEEK and CFR-PEEK has been studied, using many cell lines, both human and animal [98,99,100,101]. Fibroblasts and osteoblasts are types of cells that orthopedic and dental implants are expected to be in contact with during their service life. Results from an *in vitro* study using cultured fibroblast and osteoblast cell lines derived from the 3T3 mouse showed that PEEK surfaces, both with and without carbon fiber reinforcement, were non-toxic to these cell lines [100]. Several well-established cell culture tests were utilized in this study, and the findings demonstrated that PEEK and CFR-PEEK supported the growth of fibroblasts and osteoblasts without any signs of inhibition of cell growth around the material. It was also noted that PEEK containing carbon fibers stimulated osteoblast protein content, possibly due to the somewhat porous nature of the composite surface [100].

Another recent study compared implantable grade PEEK to commercially pure titanium (cpTi) using a human primary osteoblast model [102]. The PEEK surfaces used in this experiment were processed using extrusion or injection molding, both commonly used in the commercial production of PEEK implant materials. Osteoblast cell response was measured at several stages, corresponding to the biological response after implantation of an implant, including adhesion (initial cell attachment),

proliferation (multiplication of cells), alkaline phosphatase study (differentiation into specific cell types), and mineralization (in which cells calcify and begin hardening into bone) [102]. It was found that while surface roughness of both PEEK and titanium had an effect on the initial cell attachment and proliferation, PEEK surfaces performed equally as well as commercially pure titanium, producing increases in levels of cell differentiation and calcium content for human osteoblasts.

Wear debris has been shown to be a complication of metallic implants, causing adverse tissue reactions in some cases. The effect of PEEK wear debris has also been studied using biological testing, using wear debris from both pure PEEK and CFR-PEEK components. The effect of wear debris on the spinal cord has been investigated in a rabbit model [103]. The spinal cord was chosen as the area of implantation in this study, to simulate the effects of wear debris resulting from a spinal fusion implant constructed from PEEK. In this study, high concentrations of PEEK particles were injected into the spinal cord and nerve roots of healthy rabbits, and the results were compared with rabbits receiving no injections as a control population. At several time periods, it was observed that there was not any adverse reaction, such as necrosis or chronic inflammation, in either the spinal cord, dura matter (outermost layer of fiber surrounding the brain and spinal cord), or nerve roots, demonstrating that even in uncommonly high concentrations, PEEK wear debris was harmless to the spinal cord [103].

The effect of wear debris originating from carbon fiber-reinforced PEEK has also been studied [65]. Wear simulation tests have shown that that acetabular inserts (used in hip replacements) made from implantable-grade PEEK polymer with carbon fibers yield lower wear rates and a smaller amount of wear particles compared with other materials [65]. Wear particles from medical-grade PEEK were biologically tested in concentrations of 0.5 and 1.0 mg/ml with human fibroblasts and results showed that the material was well tolerated biologically. Implantable-grade PEEK polymer particles extracted from the simulator test for acetabular inserts were found to be smaller than 15  $\mu\text{m}$  [65].

Concerning the biocompatibility of PEEK with various degrees of crystallinity, a recent study investigated the performance in vitro and in vivo of PEEK fracture fixation plates having different degrees of crystallinity: one type of plate was constructed from optically amorphous PEEK (approximately 15% crystalline) and the second type constructed of the typically semicrystalline PEEK (32-34% crystallinity) [104]. Biological response was evaluated initially in vitro and subsequently in vivo after implantation in sheep with a 3-year follow-up. Both materials were well tolerated initially, without adverse reaction in cell culture studies. After the 3-year follow-up period, both PEEK plates were found to have retained mechanical stability and to have successfully provided structural support as fracture fixation devices, with neither plate producing any allergic reaction or inflammation. It was concluded that both optically

amorphous and crystalline PEEK polymers are suitable materials for the fixation of fractures and osteotomies [104].

#### **2.1.8. PEEK in spinal implants**

Because of its favorable set of properties with respect to biocompatibility, chemical stability, radiolucency, and appropriate mechanical strength, PEEK has become increasingly prevalent in spinal implant applications. The first biomaterials manufactured from PEEK were spinal cages that were introduced by AcroMed (now DePuy Spine) in the early 1990s [105]. The spinal fusion cages, as discussed previously, were developed to stabilize the anterior column of the lumbar or cervical spine and allow fusion of the vertebrae in patients suffering from intractable back pain caused by degenerative disc disease and/or spinal instability [105]. Following the development of the posterior lumbar interbody fusion (PLIF) cage, surgeons Arthur Steffee and John Brantigan developed a titanium implant with a columnar opening to allow bone ingrowth and fusion of the associated vertebrae. However, the initial design of this device, constructed of titanium to meet the mechanical loading requirements, was eventually found to have two problems; the high elastic modulus which could cause stress shielding and inhibit bone growth, and the imaging difficulties associated with titanium's lack of radiolucense, making diagnostic evaluation of bone growth difficult by X-rays and MRI [107]. In order to overcome these limitations, many high-performance thermoplastic resins were considered, including PEK, PEEK, PEKEKK, and PS [107].

Reinforcing agents of chopped and continuous carbon fibers to form a carbon fiber/polymer matrix composite were also evaluated for the cage [106]. Acromed ultimately decided upon PEEK as the optimal matrix material and continuous carbon fibers as reinforcing agents [107]. This device (named the “Brantigan cage” after John Brantigan) was successful in clinical trials and later in commercial use and greatly encouraged the use of PEEK in spinal implants by spinal surgeons and implant manufacturers.

Before PEEK was chosen as the primary polymer for spinal applications, both PEEK and Poly-ether-ketone-ether-ketone-ketone (PEKEKK) were evaluated in a 2-year pilot clinical study of the spine cage for lumbar fusion in 26 human patients [108]. Both implant materials were consolidated into plates with continuous 68% by weight carbon fibers for reinforcement, and the cages were then machined from the plates into their final form. After the 2-year period, clinical results were described as good or excellent in 21 out of 26 patients, and fair or poor results were apparently a result of problems unrelated to the cage [108]. Interbody fusion was able to be identified using radiographic observation in 100% of the cages, due to the radiolucency of the polymers. This clinical study was the first implantation of carbon-reinforced PEEK and PEKEKK in the human spine. Based on the successful fusion that was seen in this study, several other researchers and surgeons directed their attention towards spinal fusion cages constructed of PAEKs. Although most initial studies involve the use of CFR-PEEK for spine implants, there are now many cases of pure (unfilled) PEEK used in both cervical

and lumbar spinal cages [109,110]. As mentioned earlier, some current research has also investigated the use of PEEK cages containing osteo-inductive materials, such as hydroxyapatite and other calcium phosphates. One such clinical study evaluated PEEK incorporated with  $\beta$ -tricalcium particles for use in anterior cervical fusion; results showed good incorporation rate of bone without significant complications [84].

While spinal fusion cages constructed from PEEK now represent a significant percentage of currently manufactured devices, research continues on other polymeric-based fusion cages with similar proposed benefits to PEEK cages. For example, within the last few years, studies have explored the use of a poly-L-lactic acid (PLLA) spinal fusion cages [111,112,113]. Similar to PEEK, PLLA cages are of interest due to their reduced stiffness compared with titanium, providing a more natural load-sharing between the spinal fusion cage and adjacent vertebrae. However, PLLA is perceived to have the added benefit of being bioresorbable, allowing the implant to be absorbed completely by the body once spinal fusion has occurred, eliminating any possible long-term complications of a permanent implant [111]. However, clinical trials of current PLLA fusion cages exhibited poor results in terms of successful spinal fusion using these devices. In a comparison of patients undergoing posterior lumbar fusion using either a PEEK cage or a PLLA cage, computer tomography assessment after one year follow-up showed solid fusion in 12 of 13 patients in the PEEK group, while only 6 of 12 patients showed solid fusion in PLLA group [113]. The low fusion rate observed with PLLA was suspected to be a result of early mechanical failure leading to loss of

structural support before a sufficient degree of fusion had occurred to resume the natural load-bearing capacity of the spinal segment. Another study has demonstrated this degradation in mechanical strength of PLLA cages as early as 3 months after implantation [114]. At this point in clinical trials, PEEK remains the material of choice for replacing titanium in the application of spinal fusion devices.

#### **2.1.9. Plasma activation of PEEK surfaces**

While PEEK has been shown to be well-tolerated by both osteoblast and fibroblast cells, as well as highly stable in the physiological environment, maintaining its chemical and mechanical structure without any measurable degradation, it is desirable to improve its surface in terms of bioactivity, in order to speed osseointegration and reduce recovery time for implant procedures. As previously described, the optimal method for enhancing bioactivity of orthopedic and dental implants is the coating of the bulk material with a thin, highly osseoinductive calcium phosphate coating, such as HA. (Bioactive coatings are discussed in length in Section 2.2.) In order to prepare a substrate surface for coating, several methods are practiced, including surface roughening, etching, polishing, ion implantation, etc. In the field of polymers, exposure to high-power, reactive plasmas has been shown to be highly effective in altering the polymer surface, resulting in an enhanced adhesion to subsequently deposited thin films [115,116,117,118,119,120]. This is typically achieved

using an RF-powered plasma of either oxygen, argon or nitrogen gas in a reduced pressure environment.

A study on the surface activation of polyethylene, polystyrene and PEEK using oxygen plasma described the increased functionality of the polymers surfaces as a result of increased oxidation [118]. The chemical state of each of the polymers was shown to have increased oxygen content compared with its bulk chemistry as a result of a higher number of oxygen-carbon bonds; these C-O bonds were reportedly formed by the breaking of carbon-carbon double bonds during the oxygen treatment, followed by the formation of C-O bonds in the atmosphere of increased oxygen content. It was also noted that O<sub>2</sub>-treated PEEK exhibited the most highly oxidized surface of the polymers tested.

Another study compared the effect of three types of surface activation of PEEK surfaces on the adhesion strength of a subsequently bonded adhesive film; the surface activation methods tested were degreasing by ultrasonic cleaning with methyl ethyl ketone (MEK), corona discharge treatment and exposure to oxygen and argon plasmas at 500W for several minutes [119].

It was found that the O<sub>2</sub> and Ar plasma exposure resulted in significantly higher coating adhesion strengths compared with the other methods tested. Another important finding was that the plasma-enhanced surfaces remained stable for several days after treatment; for example, the decrease in coating adhesion strength was only 15% when the plasma-treated surface was exposed to air for four weeks prior to

adhesive bonding compared with adhesive bonding immediately after the plasma treatment [119].

Other studies suggest the increase in coating adhesion strength of plasma-treated PEEK surfaces is more strongly correlated to an increased surface energy, due to increased polarity and wettability, than to increased oxygen content on the surface [120]. Awaja et al. studied the effect of RF-powered  $\text{CH}_4$  and  $\text{CH}_4/\text{O}_2$  plasmas on coating adhesion to PEEK surfaces. The  $\text{CH}_4/\text{O}_2$  plasma-reacted sample resulted in a much higher surface energy and a decreased water contact angle (increased wettability), as compared with the  $\text{CH}_4$  plasma-treated sample and untreated samples. Subsequent bonding strength was increased by a factor of 4 compared with the untreated surface.

## **2.2. Bioactive coatings**

Surface modification is often necessary to improve the biocompatibility of biomedical implants. Surface modification describes any process by which an aspect of the material surface is altered in order to better serve a specific application. Surface modifications include changes in surface roughness, surface charge, surface chemistry, wettability and other properties. Many techniques are utilized as surface modifications, including sanding, polishing, etching, microtexturing, ion implantation and coating. While all of these have their own set of advantages, the coating of biomedical implants has been the most popular choice for the last few decades and is the method used in most clinical and commercial applications due to the following benefits:

1. Applying a coating to the bulk material serves to completely change the surface chemistry of the implant; whereas ion implantation can alter the chemistry, coating provides a surface chemistry of an entirely new material, which can be tailored to the exact needs of that application.

2. Successful coating of the bulk material ensures that the substrate is never exposed to the physiological environment to which the implant is surrounded. This is of particular importance in biomedical implants because the physiological fluid which is encountered by orthopedic and dental implants is harsh in terms of its chemistry, causing corrosion and dissolution of many materials [87]. Traditional metallic implants experienced problems of corrosion and release of metallic ions; as a result, inflammation of the surrounding body tissue, as well as allergenic reactions, have been commonly cited [121,122,123].

Several bioactive ceramic materials have been employed for surface coatings in implants because of their toughness and resistance to corrosion, including bioactive glass, hydroxyapatite ( $\text{Ca}_{10}(\text{PO}_4)_6(\text{OH})_2$ ), alumina ( $\text{Al}_2\text{O}_3$ ), and tricalciumphosphate ( $\text{Ca}_3(\text{PO}_4)_2$ ) [124].

### **2.2.1. Hydroxyapatite coatings**

As mentioned above, when coating biomedical implants that are designed for orthopedic and dental applications, the goal is to more closely match the surface chemistry of the implant with that of human bone; these implants are designed to come

into direct contact with the bone (or tooth) and the ultimate goal is to achieve osseointegration. This occurs as a result of new bone growth between the bone and the implant, which densifies and unites the two as one mechanical component. Calcium phosphate coatings, most notably hydroxyapatite (HA), are well known for good osteoconductivity (favorable attachment of osteoblasts), providing rapid biological response and acting as a scaffold for bone growth [125]. Cell culture assays have demonstrated a higher alkaline phosphatase expression and increased parathyroid hormone response on hydroxyapatite surfaces compared with titanium [126], as well as an increased formation of extracellular matrices [127]. The mechanism by which calcium phosphate coatings increases osteoconductivity has been studied and characterized in terms of the phases of bone development; initially, calcium and phosphorous ions dissolve from the coating surface, resulting in a high local concentration of Ca and P ions within the physiological environment; as a result, biological hydroxyapatite crystals precipitate on the CaP coating surface; this newly developed biological HA layer undergoes ion exchange with the surrounding tissues, stimulating bone cells to continue development, synthesizing an extracellular matrix and eventually calcifying into hard bone tissue [128]. As described previously, the hard bone tissue is then continuously remodeled in response to applied loads by osteoblasts and osteoclasts.

Due to its chemical similarity to bone and low rate of dissolution compared with other calcium phosphates, hydroxyapatite has been the standard material for coating of

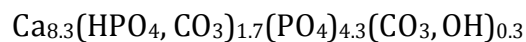
load-bearing implants for many decades [136]. Comparison of CaP compounds in terms of their relative rates of solubility yields the following relationships:



where ACP is amorphous calcium phosphate, DCP is dicalcium phosphate ( $\text{CaHPO}_4$ ), TTCP is tetracalcium phosphate ( $\text{Ca}_4\text{P}_2\text{O}_9$ ), TCP is tricalcium phosphate ( $\text{Ca}_3(\text{PO}_4)_2$ ), and HA is crystalline hydroxyapatite ( $\text{Ca}_{10}(\text{PO}_4)_6(\text{OH})_2$ ). The dissolution of HA in physiological solution increases with increasing porosity and surface area, and decreases with increasing particle size, and degree of crystallinity [131,132].

Chemically, the differences between hydroxyapatite and bone mineral are their impurity concentrations and degrees of crystallinity [133]. Bone mineral consists of partially crystalline apatite and contains several impurities, including water (9.7 wt%), carbonate (5.7 wt%), sodium (0.5-0.7 wt%), magnesium (0.3-0.6 wt%) as major impurities, and zinc, strontium, aluminum, lead and barium as minor impurities [133].

In bone, the metallic ions substitute for calcium sites in the HA structure, while the carbonate groups replace either the phosphate or hydroxyl groups [133]. These substitutions lead to an average composition of biological hydroxyapatite with the following chemical formula:



Because body fluid is supersaturated with biological hydroxyapatite, calcification of

biological HA on implanted materials is greatly enhanced by the presence of an HA surface on these implants.

Hydroxyapatite coatings first received regulatory acceptance for human use in 1991 and have exhibited excellent results from clinical studies since then [134]. Early use of HA coatings in the 1990s was primarily in the application of hip implants; the femoral stem component of the implant, constructed from titanium, was coated with HA using the plasma spray method [31]. The strong fixation between implant and bone that resulted from a greater affinity of bone forming cells, called osteoblasts, to attach to the hydroxyapatite surface compared with bare titanium allowed for implants to be inserted without the use of bone cement to fix the implant in place. Cementless implantation is a preferred option due to the fact that some patients are allergic to PMMA bone cement, as well as the recent discovery of *bone cement implant syndrome* (BCIS), in which serious complications can be caused by degradation of bone cement [135]. Since the introduction of hydroxyapatite coatings as the standard for enhancing bioactivity of orthopedic and dental implants, several methods for applying HA coatings have been developed and studied.

### **2.2.2. Commercially-produced hydroxyapatite coatings**

The current commercial method for applying calcium phosphate coatings, including HA coatings, onto biomedical implants is plasma spraying. In this method, a gas stream is used to carry the HA powder, which passes through electrical plasma

produced by a low- voltage, high current electrical discharge [136]. Aspects of this process are shown in Figure 2-9. The composition of the carrier is typically either argon or a mixture of argon and other gases. Plasma spraying of HA and CaP usually takes place under normal atmospheric conditions, as opposed to plasma-spraying of metallic components which usually takes place under a vacuum or in an inert atmosphere to minimize oxidation [136]. This method is used because of its high deposition rate, low cost, and ease of application. Plasma spraying, however, has many disadvantages as a coating method, including degradation of the polymer substrate, poor coating adhesion and non-uniformity of the HA coating itself in terms of chemical composition, porosity, density and crystallinity.

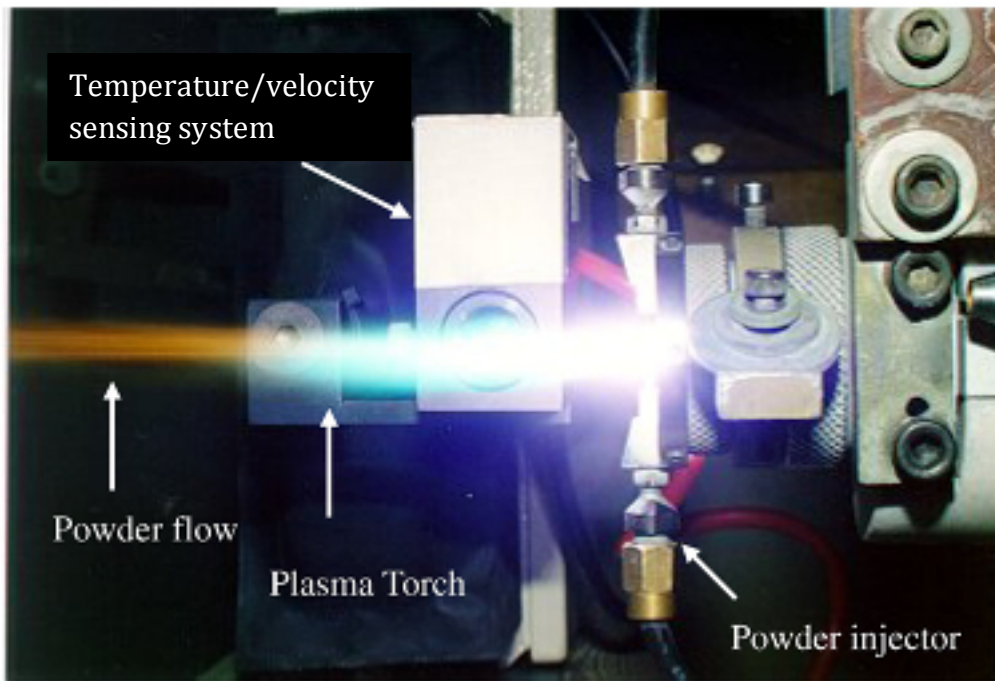


Figure 2-9. Plasma-spray apparatus used in depositing HA coating onto carbon-fiber reinforced PEEK substrates [124]

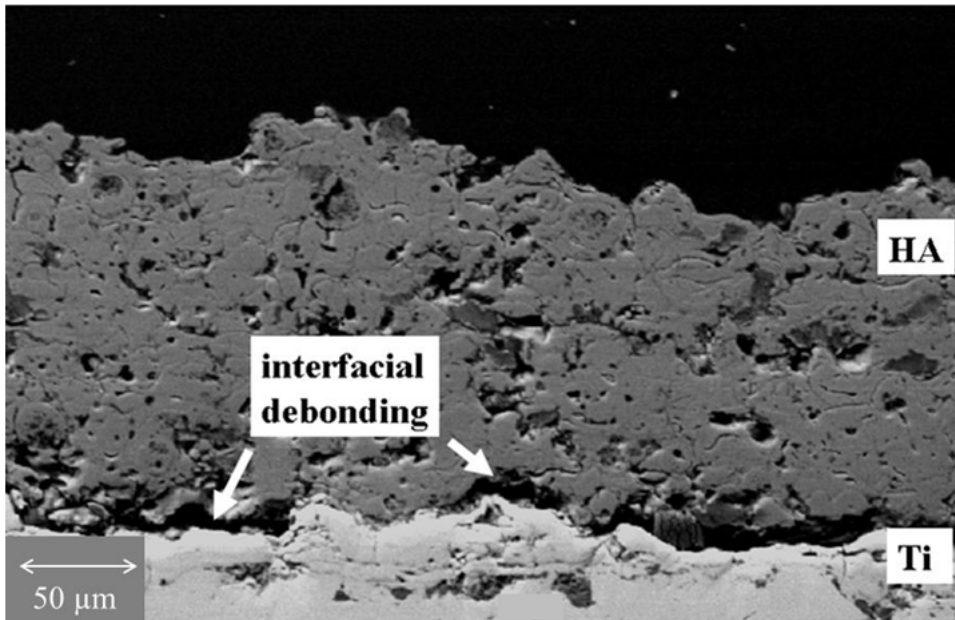


Figure 2-10. SEM micrograph of plasma-sprayed HA coating/Ti interface [137]

Figure 2-10 shows a cross-section of a plasma-sprayed HA coating on a titanium substrate. Several features which are common to plasma-sprayed HA coatings are displayed in this image: 1) the coating is very thick (greater than 100  $\mu\text{m}$ ), resulting in residual stresses when cooled caused by mismatch in thermal expansion coefficients between HA and titanium; 2) there is a large degree of interfacial de-bonding at the coating/substrate interface due to the combination of above mentioned residual stresses along the interface together with weak mechanical bonding formed during rapid cooling of the molten HA at the Ti surface, resulting in poor adhesion strength (less than 15MPa); 3) the microstructure is non-homogeneous, containing porosity and various defects [137]. The result of the various phases of calcium phosphates and

porosities contained in plasma-sprayed CaP coatings is degradation of the coatings by rapid dissolution of the highly soluble amorphous phase followed by loosening of the crystalline HA particles. Some studies have demonstrated that the resulting loose crystalline HA particles around the implant can cause a foreign body response [138]. While the specific properties of plasma-sprayed HA coatings vary depending on the manufacturer, the problems associated with this deposition method are consistently observed. Due to the many disadvantages to HA coatings produced by plasma-spraying, several other approaches to depositing HA coatings onto implant surfaces have been researched extensively in recent years.

### **2.2.3. Experimental methods of applying HA coatings**

Much research has been focused on developing techniques for applying HA coatings to biomedical implants without the problems associated with the commercially-accepted plasma-spray method. Problems with plasma-spray HA coatings arise mainly from their thickness and nonhomogeneity in terms of interfacial voids, porosity and crystallinity; therefore new techniques are designed to produce dense HA coatings of reduced thickness, better adhesion and higher crystalline content. Physical vapor deposition (PVD) and chemical vapor deposition (CVD) processes have been used extensively in semiconductor, aerospace and tooling industries to produce coatings of inorganic elements (metals and semiconductors) and compounds (oxides and other ceramics), as well as carbon and some other organic materials [125]. PVD and CVD

methods are of particular interest because of their ability to produce thin films of homogeneous microstructure, with thickness from the nanometer range to several microns, and with good control over coating properties. As such, several of these methods have been applied in the deposition of HA thin films onto biomedical implants. Each of these techniques has its own set of advantages and disadvantages and produce HA coating with various characteristics. A few of these methods are described briefly in this section.

### **2.2.3.1. Physical Vapor Deposition (PVD) processes**

Physical vapor deposition methods involve creating a vapor of atoms evaporated from a solid or liquid source which is then condensed onto a substrate surface in a low pressure environment [125]. PVD processes do not require elevated temperatures and can be used to deposit films with thicknesses in the range of a few nanometers up to several microns. Due to the ability to deposit at room temperature and because neither the coating material nor the substrate need to be reactive, PVD techniques can be used to deposit a wide variety of coating materials onto many different types of substrates. Coatings produced by PVD methods are typically dense, uniform and exhibit good adhesion to the substrate surface [139]. Physical vapor deposition is comprised of several techniques including evaporation processes and sputtering processes. Evaporation processes such as thermal arc evaporation, electron beam evaporation and pulsed laser deposition use thermal energy to break bonds and free atoms from solid or

liquid targets. On the other hand, sputtering processes such as magnetron sputtering and ion beam deposition, use high energy particles (ions, atoms, electrons) to free atoms by collision with the sputter source. A few of these PVD methods, as they have been applied to the deposition of HA coatings, are described in this section.

Pulse laser deposition (PLD) is a process in which a high-power pulsed laser beam is used to evaporate a solid HA target by laser ablation in a low pressure environment, causing HA particles to deposit on the substrates. PLD produces HA coatings with thickness between 50nm and 5 $\mu$ m, consisting of various densities and various degrees of crystallinity depending on process parameters [136]. Figure 2-11 shows a) cross-sectional and b) top coating surface SEM images of crystalline HA deposited by PLD. As seen in Figure 2-11a, the HA coating exhibits a columnar structure, with grains oriented normal to the growth direction. While dense, crystalline HA coatings can be produced, PLD has the disadvantage of forming calcium phosphate phases other than HA due to decomposition that occurs as a result of the high energy and heat used in ablation of the HA target. PLD is also a “line of sight” technique, meaning that only substrate areas that are directly facing the HA target are coated, making complex geometries difficult to coat [140].

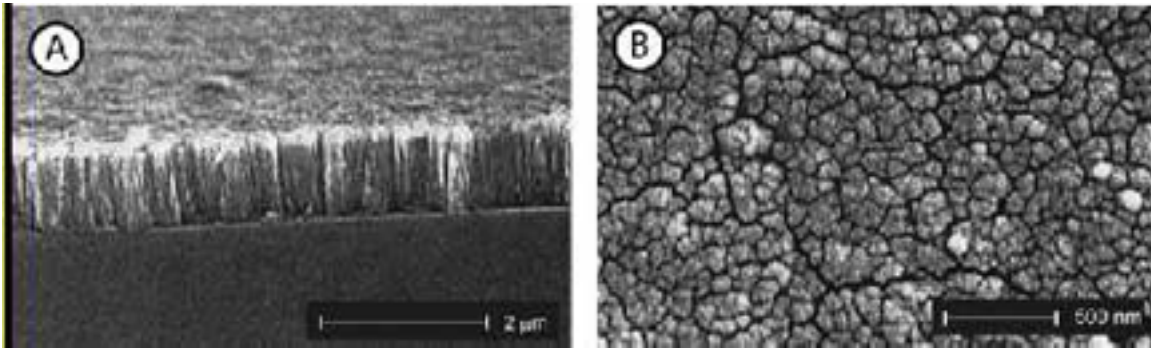


Figure 2-11. SEM images of HA coating deposited onto Ti alloy substrates by pulsed laser deposition: a) cross-sectional view; b) top view of coating surface [140]

Sputter deposition, which has been described previously as it is used in this research, is a physical vapor deposition method in which atoms from a solid target material are evaporated by bombardment with high energy particles, such as ions; these ejected atoms then condense on the substrate surface in a reduced pressure environment (high vacuum chamber). The high energy particles are generated by a positively charged plasma, generated applying a DC or RF field to a pressurized gas such as argon or oxygen. Sputter deposition has advantages of producing uniform, dense coatings of 0.5 to 3.0 μm with good adhesion at low processing temperatures; however, it is also a line of sight technique, and HA coatings produced by sputtering are usually amorphous [136].

### 2.2.3.2. Chemical Vapor Deposition (CVD) processes

Chemical vapor deposition (CVD) is a type of process in which volatile chemical compounds are reacted in the gas phase, producing a nonvolatile which deposits on the substrate surface as it condenses [141]. CVD processes generally follow an order of steps to arrive at the deposition of atoms or molecules, forming a thin film, on the substrate surface:

1. Reactants are transported from gas inlets into the reaction chamber by means of convection, diffusion and forced flow.
2. Chemical reactions take place in the gas phase which produce new reactive species
3. The initial reactants and their products arrive at the substrate surface, where they are adsorbed (chemically and physically).
4. The substrate surface catalyzes reactions of the newly adsorbed reactants, producing the coating as a product.
5. The by-products are removed from the substrate surface by convective and diffusive transport.

Many variations of CVD processes have been developed including atmospheric pressure CVD (APCVD), low-pressure CVD (LPCVD) and plasma-enhanced CVD (PECVD). CVD can be used to produce a wide variety of films with good control over stoichiometry at low cost. However CVD requires elevated temperatures and a reactive substrate surface, which make this technique unsuitable for non-reactive materials (such as PEEK).

### **2.2.3.3. Other HA coating methods**

Physical and chemical methods of applying HA coatings that are not categorized by PVD or CVD include precipitation from solution, dip coating, electrophoretic deposition, sol-gel spinning and hot isostatic pressing (HIP). These methods are typically easier and less expensive than low pressure processes, but produce HA coatings with low adhesion to substrates.

Sol-gel coating is a process in which an HA colloidal solution is dip-coated or spin-coated onto substrates and is then sintered to remove moisture and solidify the coating onto the substrate. This method produces HA coatings of 1 $\mu$ m or less and has advantages of low cost, relatively low processing temperatures ( $\sim$ 500°C), ability to coat complex shapes, and homogenous coatings [136]. However, sol-gel coatings produce HA coatings with low adhesive strength and the post-deposition sintering can produce residual stresses within the coating as a result of thermal expansion mismatch between coating and substrate [142].

Hot isostatic pressing is a method that incorporates a combination of pressure and heat in order to sinter a powder onto the substrate with high density. The substrate is first coated with an HA powder (plus a binder to aid in solidification) and is then encapsulated in a mold and pressed at elevated temperature [143]. This method can produce HA coatings between 0.2 and 2.0mm of high density. Disadvantages include the inability to coat substrates of complex geometry, high temperature required and

thermal expansion mismatch between coating and substrate, producing residual stresses within the coating and resulting in poor coating cohesive strength [136].

#### **2.2.4. Bioactive coatings on PEEK substrates**

PEEK has been previously shown to exhibit good biocompatibility in terms of lack of toxicity to cells, inflammatory response to wear debris, infection or rejection by the body; however, because PEEK is not an osseoconductive material, it does not actively participate in the attachment of osteoblast cells or aid in the formation of new bone. One of the major problems with such bioinert polymers is the attachment of fibrous tissue, rather than bone tissue, to the implant surface [144]. This fibrous tissue can encapsulate the implanted material, isolating it and preventing the implant from forming a functional bond with the surrounding bone. Several studies have investigated methods of improving the bioactivity of PEEK surfaces in order to enhance bonding with bone-forming cells without formation of fibrous tissue [144]. Because PEEK is a relatively new biomaterial, studies on surface modification of PEEK for the purpose of increased bioactivity are limited; however, following the industrial method used in production of metallic implants, commercially produced PEEK implants are also coated with hydroxyapatite by the plasma-spraying process.

The coating/substrate interface of plasma-sprayed hydroxyapatite coatings on carbon-fiber reinforced PEEK substrates has been investigated [31]. It was shown that the resulting HA coating has very low adhesion strength, measured at 2.8 MPa. The

cause for the low coating adhesion strength in this case was found to be related to the degradation of the PEEK substrates due to the high temperature of arriving HA particles, which is a common characteristic of the plasma-spray process. The high temperature molten HA causes evaporation of the underlying PEEK substrate, producing a vapor film, which is assumed to partially prevent close contact of the HA coating with the substrate, resulting in low coating-substrate adhesion.

In a similar study of gas plasma-sprayed HA coatings on PEEK composite substrates, the coating process was improved compared with traditional plasma-spray coatings by evaluating and optimizing the processing parameters such as carrier gas flow rate, plasma power, spray distance and powder feeding rate using a high temperature sensing system incorporated into the plasma-spray system [124]. Surface temperature of the arriving molten HA powder was decreased and the resulting HA coating had less porosity. Additionally, it was observed that pre-coating the PEEK substrates with a thin layer ( $\sim 10\text{nm}$ ) of titanium resulted in a more uniform HA coating layer [124]. While this represents an improvement over traditional plasma-sprayed HA coatings, the coating thickness was still in the range of  $30\text{-}40\ \mu\text{m}$ , which has been shown to have poor cohesive strength, and the temperature of the molten HA during deposition, while decreased, was still above  $2700^\circ\text{C}$ , which is well above the melt temperature of PEEK.

Other attempts have been made at improving the bioactivity of PEEK implants by coating with titanium with the thought that the  $\text{TiO}_2$  that forms on its surface may

promote faster osteoblast attachment and growth. In a study of CFR-PEEK dental implants, a 200nm thick titanium coating was applied using plasma vapor deposition and implanted, along with uncoated control samples, into the femurs of dogs in order to study the bone contact, bone ingrowth, inflammatory response and adhesion strength of attached bone [145]. Bone contact area after 8 weeks of implantation was slightly higher (60% compared with 51%) on the Ti-coated samples compared with the CFR-PEEK surfaces, however no significant difference was seen between the two sets of samples in terms of bone attachment shear strength. Neither type of samples produced an inflammatory response, leading to the conclusion that both types of surfaces are biocompatible, and that the thin titanium coating may provide a small increase in bone cell attachment per area compared with the PEEK composite surface.

Titanium has also been used as an intermediate coating on PEEK substrates to increase adhesion of a subsequently deposited HA layer [146]. A vacuum plasma-spray process was used to produce a bilayer coating of titanium and hydroxyapatite on CFR-PEEK substrates with the intention of increasing the adhesion of the HA coating; it is suggested that the molten HA used in plasma-spraying exhibits better spreading on titanium than on PEEK and CFR-PEEK surfaces and leads to a higher quality interface with few voids [146]. As seen in Figure 2-11a, both the PEEK/Ti and Ti/HA interfaces appear to exhibit good bonding, without the presence of many voids between layers. However, Figure 2-12a shows that the HA coating thickness is rather thick ( $\sim 100\mu\text{m}$ ), a characteristic of plasma-sprayed coatings which has previously been shown to cause

poor cohesive strength in ceramic coatings; also, as can be seen in Figure 2-12b, the top view of the HA coating shows a non-homogeneous microstructure, containing porosities and HA crystals of various sizes, which ultimately leads to an HA coating which is highly susceptible to rapid dissolution after implantation.

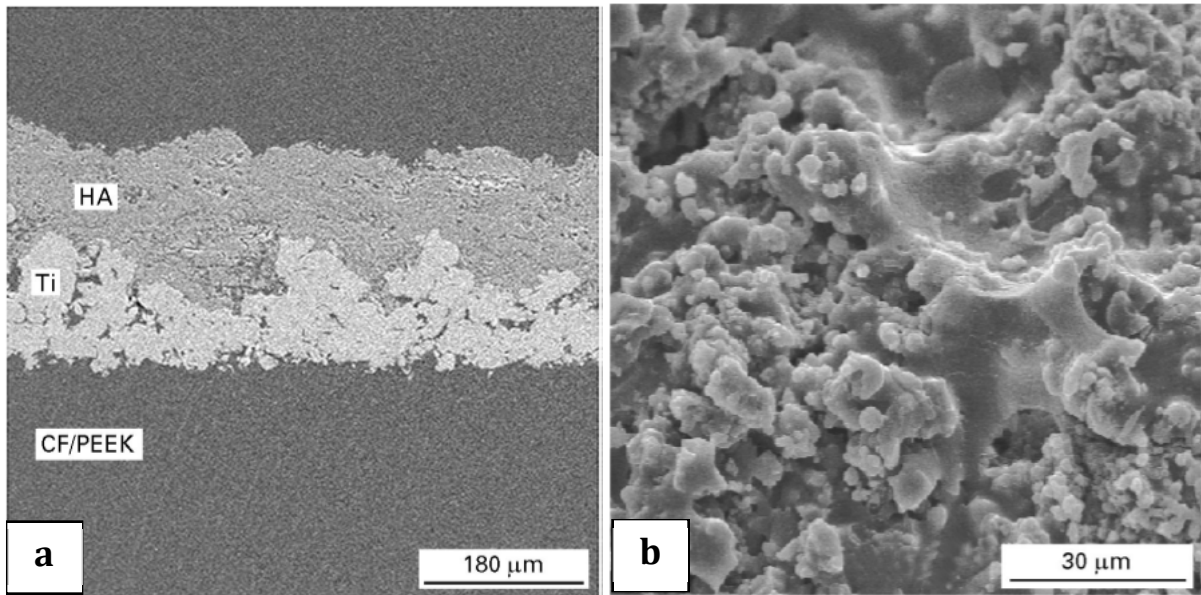


Figure 2-12. SEM images of Ti/HA coating on CFR-PEEK (a) cross section, (b) top view [146]

### 2.2.5. Yttria-stabilized zirconia in bioactive coatings

Yttria-stabilized zirconia ( $Y_2O_3 - ZrO_2$ ), or YSZ, is a ceramic oxide material containing a majority molecular composition of zirconia,  $ZrO_2$ , and varying percentages of yttria,  $Y_2O_3$ , as a phase-stabilizing compound. YSZ films possess many desirable properties, most notably its very low thermal conductivity, which has led to its widespread use as a thermal barrier coating. In addition, YSZ exhibits chemical stability, a high dielectric constant, high melting point, high hardness, and the ability to be

tailored by varying the amount of yttria or by adding other phases [147]. YSZ is currently used in several applications including thermal and chemical barrier coatings, buffer layers between superconductors and sensors in microelectronics, and optical coatings [147]. Some thermal, physical and electrical properties of YSZ films are listed in Table 2-4. These properties are in reference to a YSZ film of 7 weight % yttria and produced by a sputtering process and will vary in YSZ films of various yttria percentages and in films produced by different methods.

Table 2-4. Selected properties of YSZ thermal barrier coating [148]

Property	Thermal conductivity (W/(m K))	Coefficient of thermal expansion (K <sup>-1</sup> )	Melting Point (°C)	Fracture toughness (J/m <sup>2</sup> )	Dielectric constant, k
YSZ (7%Y <sub>2</sub> O <sub>3</sub> )	1.5–1.9	11x10 <sup>-6</sup>	2700	3.7–3.9	27

As mentioned above, yttria (Y<sub>2</sub>O<sub>3</sub>) is added in small percentages for the purpose of preventing the phase changes which pure zirconia undergoes when cooling from solid solution temperatures. This is accomplished by the formation of more stable tetragonal or cubic crystals, which are less susceptible to phase change than the original monoclinic structure, leading to an improvement in thermal, mechanical and electrical properties. Properties of yttria-stabilized zirconia coatings vary with molar percentage of yttria [149]. For example, YSZ containing small percentages of yttria (2–3 mol% Y<sub>2</sub>O<sub>3</sub>) forms a tetragonal structure, which exhibits a high fracture toughness and

resistance to thermal shock. “Partially stabilized” YSZ (~5 mol%  $Y_2O_3$ ) is composed of a mixture of several phases and is used in thermal barrier coatings. Finally, “fully stabilized” YSZ (8-12 mol%  $Y_2O_3$ ) forms a cubic crystal structure and possesses the highest ionic conductivity, making it particularly useful in electrical and optical applications [149].

The biocompatibility of YSZ has been confirmed in vivo [49]. YSZ has been added to bioactive glass (wt %: CaO-47.7, PO-6.5, SiO-43.8, MgO-0.5 and CaF-0.5) in percentages up to 30% by volume, in order to toughen the bioceramic, which is used in dental implants and as artificial bone. Bone bonding strength of the bioactive glass/YSZ composite was evaluated after implantation for up to 84 days in femora and tibiae of dogs; bonding strength of the living bone to the bioactive glass/YSZ composite was shown to be as high as that of the bioactive glass without YSZ, while improving the coating cohesive strength as compared with the bioactive glass without YSZ [49].

As with HA, many methods can be utilized to deposit YSZ coatings, including sol-gel spinning, plasma-spray, electron beam evaporation, pulsed laser deposition, and sputtering. Sputtering has been shown to be an effective method of producing uniform YSZ coatings with good density, high adhesion strength to substrates, and with the benefit of low deposition temperature, making this a favorable method for temperature-sensitive substrate materials [147,150,151].

### **2.2.5.1. Thermal barrier properties**

YSZ coatings have traditionally been used as thermal barrier coatings for large-scale components in extreme temperature environments. Typical applications include protective coatings for high temperature gas turbine engine components such as turbine blades and nozzle guide vanes using YSZ coatings in the range of 100 to 150 $\mu$ m. However, due to advances in thin film coating technology enabling the fabrication of uniform, homogeneous thin films of low porosity and high adherence to substrates, much thinner YSZ coatings (< 2  $\mu$ m) are now being employed in a number of other applications such as in optical, electronic and aerospace industries. For example, YSZ films of 225nm thickness have been developed as a buffer layer of the superconducting film and a gate dielectric of the integrated circuit [152]. These nano- to micro-scale YSZ coatings can provide heat shielding on a much smaller scale to the microscopic components used in such devices.

Protective-coating of solid oxide fuel cells (SOFCs) represents another application of micron-scale YSZ thermal barrier coatings. SOFCs must retain high ionic conductivity, low thermal expansion and thermodynamic stability in the presence of volatile environments at temperatures above 500°C [153]. Recently, thin (1~2 $\mu$ m) YSZ coatings have been deposited on silicate ceramics using RF magnetron sputtering for the purpose of prohibiting silicon oxide volatilization at temperatures of 525–725°C. The coatings produced were found to be dense, crystalline and without the presence cracks.

In another study, phase composition, microstructure and mechanical properties of YSZ coatings of less than 10  $\mu\text{m}$  produced by RF magnetron sputtering have been studied as a function of deposition parameters [147]. Deposition rate, crystallite size and percentage of monoclinic YSZ phase were shown to be dependent on RF sputtering power and vacuum level. However, all films produced exhibited good uniformity and adhesion to the substrates, and exhibited a columnar structure with the grains preferentially oriented along the growth direction [147]. This columnar grain structure can be explained by the structure zone model (SZM) for sputtered films deposited at low pressure and at various substrate temperatures. As shown in Figure 2-13, decreasing substrate temperature and decreasing pressure results in increasingly finer columnar-grained films, oriented perpendicular to the growth direction (or normal to the substrate surface).

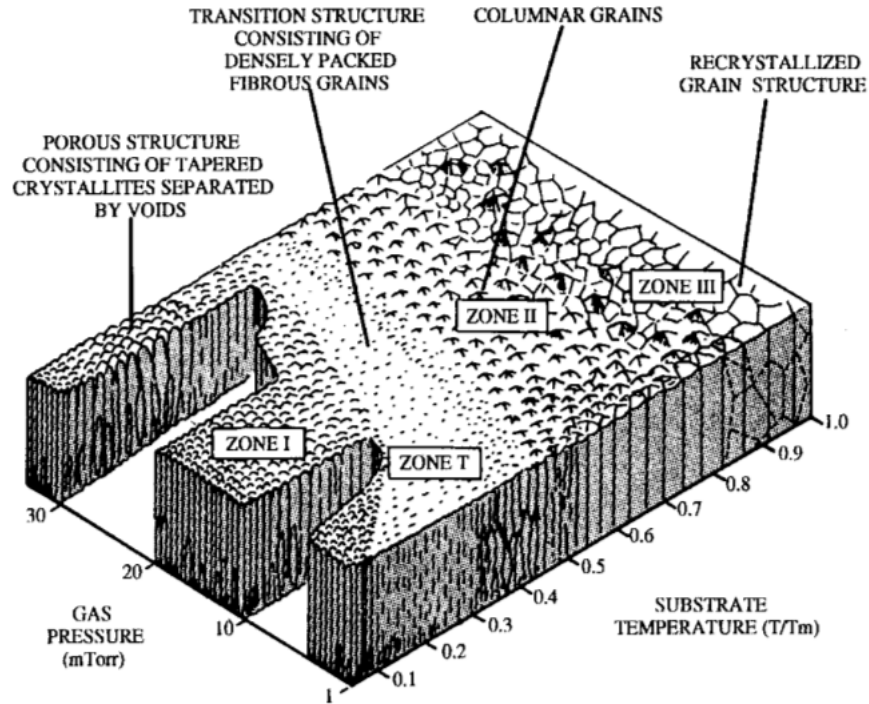


Figure 2-13. Structure zone model (SZM) for sputtered thin films [154]

### 2.2.5.2. Improvement of HA coatings

In addition to its excellent thermal shielding capabilities when used as a thermal barrier coating, YSZ can also be used as an intermediate layer or second phase material in other coatings to strengthen the overall coating and provide added adhesion to substrates of many types. Particularly useful for coating of biomedical implants, YSZ has been shown to increase the cohesive strength of HA coatings and to improve the quality of the substrate/coating interface, resulting in higher adhesive strength [47,48,49,50].

In a study of plasma-sprayed HA/YSZ composite coatings, the addition of YSZ was shown to increase the bond strength to the Ti-6Al-4V substrates; additionally it

was observed that YSZ containing 8 wt.% yttria had more of an effect in strengthening the HA coating compared with YSZ of 3 wt.% yttria [47]. The composite coatings reportedly had slightly increased porosity compared with pure HA coatings; however this was perceived to be outweighed by the increased fracture toughness of the composite coating.

Other studies have utilized YSZ as an intermediate layer, between the HA coating and the substrate, as a method of increasing coating adhesion. YSZ is thought to possess an ability to form stronger bonds with substrates compared with HA due to its higher toughness value [48]. Using a YSZ intermediate layer, bond strength of HA to a Ti-6Al-4V substrate was improved from 28 MPa to 36 MPa; this effect was suggested to be a result of the increase in toughness and a higher average surface roughness due to the YSZ bond coat. Surface roughness was nearly doubled on the YSZ coating surface, which may provide additional mechanical interlocking of the subsequent HA coating. This increase in surface roughness is likely due to the columnar crystal structure of the as-deposited YSZ, shown in Figure 2-14.

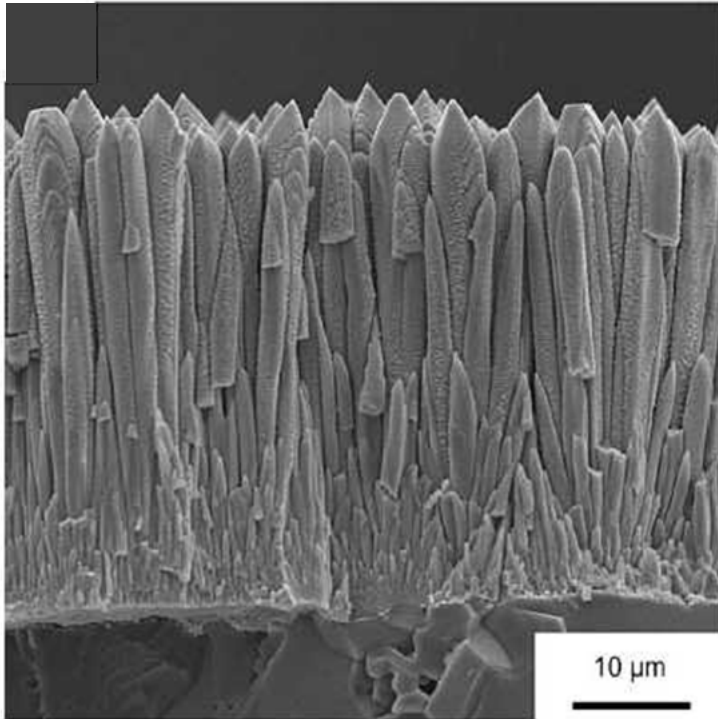


Figure 2-14. SEM Image of YSZ coating cross-section [155]

The improvement in coating adhesion that arises from using a YSZ interlayer can be explained in part by observation of the YSZ coating cross-section, shown in Figure 2-14. At the interface region, the YSZ coating is observed to be very dense and well-bonded to the substrate, without voids or porosity; the crystalline structure is comprised of very fine, sub-micron equiaxed columnar grains. Further away from the interface, the columnar structure is maintained, as described by the structure zone model (SZM), but grains are seen to grow larger as coating deposition progresses, forming crystals of a few microns in diameter, and up to 60 μm in length. The resultant morphology of the YSZ top coating surface exhibits a high surface roughness along with some porosity; it is

believed that this morphology is responsible for the greater adhesion of the HA layer which is subsequently deposited; the HA coating is able to form better mechanical bonding to this surface as compared with the dense non-porous substrate surface, attributing to a stronger mechanical bond.

#### **2.2.6. Low temperature crystallization of Hydroxyapatite Coatings**

Coating of polymers with hydroxyapatite and other calcium phosphates for the purpose of increased bioactivity is a very recent development in the field of biomaterials, and as such, there are very few studies published on this topic. Compared with metallic implants, coating of polymeric implants presents additional challenges. First of all, achieving a well-adhered coating on polymer substrates is difficult due to the vast chemical and physical differences between the ceramic coatings and polymer substrates. As discussed previously, this challenge can be addressed through the pre-treatment of the polymer to form a more reactive surface, the use of an intermediate layer to promote better attachment of the HA coating, and the use of a low-temperature, high energy coating deposition process, such as ion beam deposition or sputtering to form dense, well-adhered coatings without interfacial voids without damaging the polymer surface in the process.

Secondly, HA coatings produced using sputtering processes are inherently amorphous. Amorphous HA, as describe previously, is highly soluble in the physiological environment [25,26]. Some degree of dissolution can be beneficial in the

early stages after implantation to provide calcium and phosphorous to the newly growing bone, however, in order to provide long-term stability of a biomedical implant, the HA coating should be retained on the surface of the implant [63,175]. Therefore, a post-deposition treatment is needed to crystallize the amorphous as-sputtered HA coating. Conventional methods of HA crystallization involve annealing at temperatures above 600°C for periods of at least one hour, however, the low melting point of polymeric materials prohibits this type of process. Therefore, alternative methods of HA crystallization, requiring lower substrate temperatures, must be explored. Crystallization of HA coatings at substrate temperatures lower than those used in conventional annealing can be achieved by either 1) lowering the activation energy for HA amorphous → crystalline phase change or 2) selective heating of the coating, without causing a significant increase in temperature of the substrate material. A few of these methods are described in the following sections.

#### **2.2.6.1. Hydrothermal annealing**

Hydrothermal annealing can cause amorphous calcium phosphates to undergo the phase transition to crystalline hydroxyapatite at temperatures of 300°C or less by lowering the activation energy for the phase change to occur; this is accomplished using the combination of moderately elevated temperature along with high pressure water vapor (steam) in an autoclave or pressure vessel. This method was first introduced as a way to improve the crystallinity and homogeneity of plasma-sprayed HA coatings [156].

Hydrothermal annealing has since been shown to be effective on sputtered HA coatings at even lower temperatures [60,61,157]. RF magnetron sputtered HA films of 1 $\mu$ m thickness underwent hydrothermal treatment at 110°C and 0.145 MPa using an autoclave for times of 6 to 72 hours, resulting in crystalline HA, as evident from XRD, as well as a significant reduction in the rate of dissolution for samples receiving at least 48 hours of treatment, as compared with as-sputtered films [157]. Another study analyzed the hydrothermal crystallization kinetics of hydroxyapatite films, quantifying the activation energy for the amorphous to crystalline phase transformation [158]. Activation energy in the presence of saturated steam was reported as 17.4 kJ/mol, as compared with 24.6 kJ/mol in vacuum and 19.1 kJ/mol in an ambient atmosphere. The presence of H<sub>2</sub>O is thought to be the driving factor in the reduction of activation energy; as-sputtered and plasma-sprayed HA coatings are known to be hydroxyl-deficient (missing -OH group), due to either the high temperature or the low pressure environment during the coating deposition. The abundance of water vapor, along with high pressure and temperature is suggested to replenish the missing -OH groups of the amorphous HA, without the need for diffusion of these molecules within the coating itself, allowing the phase transformation to take place at much lower temperatures [158]. From several studies, a range of parameters is suggested in Table 2-5, based on successful applications of hydrothermal annealing to form crystalline HA.

Table 2-5. Hydrothermal parameter for annealing of HA thin films [60,61,156,157,159]

Parameter	Value	
Duration	24 – 120 hrs	
Steam properties	Temperature (°C)	Pressure (MPa)
	150	0.476
	175	0.892
	200	1.55
	225	2.55
	250	3.98

#### 2.2.6.2. Laser heating

Laser annealing has been proven to be effective in causing phase transformation of amorphous phases in thin films to crystalline thin films [159]. This effect has been proven specifically in transforming amorphous calcium phosphate films into crystalline hydroxyapatite in recent studies [160,161]. In this method, the energy from the laser is desired to be fully absorbed by the coating material only, without passing through to the substrate material. For heating to be contained in only the coated region of a material, the laser must be of a very low wavelength (below the optical absorption edge of the coating material) and it must be pulsed, so that the material is only heated during the laser pulses and the heat is quickly dissipated before it can be transferred to the

underlying substrate. In the case of calcium phosphate coatings, the wavelength of the laser should be below 200nm, corresponding with the optical absorption edge of calcium phosphate. Lasers of this wavelength fall into the category of ultraviolet excimer lasers and include Ar<sub>2</sub> (126nm), Kr<sub>2</sub> (146nm), F<sub>2</sub> (157nm), Xe<sub>2</sub> (175nm), and ArF (193nm). In 2005, Feddes et al. studied laser crystallization of calcium phosphate coatings on polyethylene deposited by RF magnetron sputtering. In this study, crystalline HA coatings of 250nm were successfully achieved from amorphous CaP using a pulsed F<sub>2</sub> laser [160]. Based on studies of laser-induced crystallization of thin films presented in literature [159,160,161]and based on optical absorption characteristics of HA (absorption edge ~ 200nm), suggested values of laser parameters that may be successful in achieving crystallization of the amorphous HA coating layer are listed in Table 2-6.

Table 2-6. Laser parameters for annealing of HA thin films

Laser type	Pulsed excimer gas laser
Appropriate Excimer Laser Gasses	Ar <sub>2</sub> - 126 nm
	Kr <sub>2</sub> - 146 nm
	F <sub>2</sub> - 157 nm
	Xe <sub>2</sub> - 175 nm
	ArF - 193 nm
Laser fluence (energy/area)	100 - 200 mJ/cm <sup>2</sup>
Pulse duration	20 - 40 ns
Pulse frequency	50 Hz

### 2.2.6.3. Microwave annealing

The use of high-frequency electric fields for heating dielectric materials was first proposed in 1934; in a patent owned by Bell Telephone Laboratories, dated 1937, an invention was described as heating "means of the dielectric loss produced in them when they are subjected to a high voltage, high frequency field" [162]. The primary heating mechanism using electromagnetic fields at both radio and microwave frequencies occurs via the dielectric heating effect, as polarized molecules are affected by a rapidly-alternating electric field. This implies that polar molecules and materials with a high dielectric loss can be rapidly heated using microwaves, while other

materials which are transparent due to lack of a dipole or to their dielectric properties will remain unheated. This is the basis for the idea of “selective heating” of the ceramic HA coating on the transparent, non-polar PEEK substrates.

Hydroxyapatite was first proven to be susceptible to heating by microwave through the application of sintering bulk hydroxyapatite. Traditional oven sintering of hydroxyapatite requires temperatures above 1000°C, but it was demonstrated that dense crystalline HA, with crystals of 200nm, could be synthesized at ambient atmosphere using microwave processing to heat only the HA ceramic, without causing significant heating of the surroundings [163]. Microwave annealing has since been shown to be effective in crystallizing amorphous HA thin films [54,57]. Using a conventional microwave (2.45GHz, 1300W), amorphous HA coatings of approximately 400nm thickness were crystallized in time periods as short as 20min [57]. Compared with coatings of the same thickness which were exposed to rapid thermal annealing (RTA), the microwave-treated HA coatings exhibited better crystalline properties, such as larger crystal size and more distinct crystalline peaks in XRD [57].

### **2.3. Summary**

This section has been aimed at summarizing literature that is pertinent to the research conducted in the upcoming chapters. The physical, chemical and mechanical properties of PEEK have been described, as well as its applications in the biomedical industry, with specific details in regards to its use in spinal fusion cages. Bioactive HA

coatings have been discussed in terms of their effect on biological response and methods of deposition. The use of YSZ as an intermediate coating layer has been introduced and its applications in bioactive coatings summarized. Finally, the current research on deposition and optimization of bioactive coatings on temperature-sensitive substrates has been discussed.

## CHAPTER 3: FUNCTIONALLY-GRADED HYDROXYAPATITE COATINGS WITH AG-DOPING ON TITANIUM SUBSTRATES

### 3.1. Introduction

As previously described, commercially-produced HA coatings suffer from variation in microstructure and composition as well as from mechanical weakness, resulting in undesirable long-term stability rates. In addition to these limitations, bacterial infection after implantation is an increasing problem [164]. For example, infection rates for total hip arthroplasties range between 0.5% and 3.0% in primary total hip arthroplasty, despite strict antiseptic operative measures [165]. It has been reported that the overall rate of prosthetic joint infection is highest in the first 6 months postoperatively and declines continuously thereafter [166]. While infections do not commonly cause implant failure, they do result in an enormous medical cost, an increase in morbidity, and a decrease in patient satisfaction [167]. Studies on Ag incorporation in biomaterials have shown success in reducing bacterial attachment to implant surfaces [165,168,169,170,171,172,173]. In the research presented in this chapter, FGHA coatings with three different amounts of Ag addition are deposited onto glass and Ti substrates using IBAD to take advantage of FGHA's proven success in promoting cell growth and implant stability, as well as adding Ag as an antibacterial agent. It is expected that FGHA coatings incorporated with Ag will have better long-term stability and antibacterial effectiveness than similar Ag-doped coatings because of the graded crystallinity, which allows rapid release of Ca, P, and Ag ions from the

amorphous top coating layer immediately after implantation, while retaining Ca, P, and Ag in the more crystalline layers of the coating closer to the substrate/coating interface. Initial cell adhesion to materials surfaces is of critical importance when considering tissue response to biomaterials, as the initial attachment affects cell morphology and spreading and provides signals for later stages of development such as cell proliferation, cell differentiation, and cell function [174]. Materials used in orthopedic and dental implants require a high degree of cell/material adhesion, particularly in the shear direction as they mostly experience shear force in service [174]. Using the unique method of measuring shear force necessary to detach a single cell from a material surface, osteoblast cell affinity is evaluated on the FGHA coatings with and without Ag [175]. Dissolution characteristics and surface roughness of the coatings in vitro are also evaluated and correlated to the attachment of MC 3T3-E1 murine osteoblastic cells.

## **3.2. Materials and Methods**

### **3.2.1. Preparation of Titanium substrates**

Titanium discs of 7.62 mm thickness were machined from a 12.7 mm diameter 99.5% commercially pure titanium rod (Alfa Aesar, USA). Prior to coating deposition, the substrates were prepared by wet grinding with 240-, 400-, and 600-grit silicon carbide paper (Buehler) and subsequent polishing with 9, 3, and 1  $\mu\text{m}$  polycrystalline diamond suspension (Buehler). In between each of the grinding and polishing steps the discs were washed and ultrasonically cleaned to prevent cross contamination of

abrasive particles. After polishing and grinding the discs were ultrasonically cleaned in acetone and isopropyl alcohol for 10 min each and then decontaminated and passivated by exposing the discs to a 40% (by volume) nitric acid solution at room temperature for 30 minutes (ASTM F86-04). The discs were then rinsed with water and dried by compressed air. The Ti discs were saved in sterilized culture plates and then stored in desiccators.

### **3.2.2. Processing of Coatings**

Functionally graded hydroxyapatite coatings with and without incorporated silver were deposited onto the Ti discs and onto sterilized glass microscope slides using the ion beam assisted deposition (IBAD) system (Ion Tech) in the Center for Nanophase Materials Sciences (CNMS) at Oak Ridge National Laboratory (ORNL), pictured in Figure 3-1. A schematic diagram of the IBAD chamber and positions of the various components is shown in Figure 3-2. A 152.4mm diameter sintered HA target with 6mm thickness 99% purity (Cerac Inc., USA) was used to deposit coating. The target was recessed into a stainless steel holder and 21 titanium disc substrates were secured into custom made stainless steel holders, shown in Figure 3-3, for deposition in each run.

Silver wires with diameters of 1.0 and 1.5mm and 99.999% purity (ESPI) were placed on the HA target surface in order to dope Ag into the coating during deposition. For the three coatings with different Ag concentrations (FGHA-Ag1, FGHA-Ag2, and FGHA-Ag3), silver wire diameters of 1.0, 1.5 and (2 wires of 1.5mm) were used,

producing three sets of FGHA-Ag coatings with average silver concentrations of 1, 3 and 6.6 wt%, respectively.

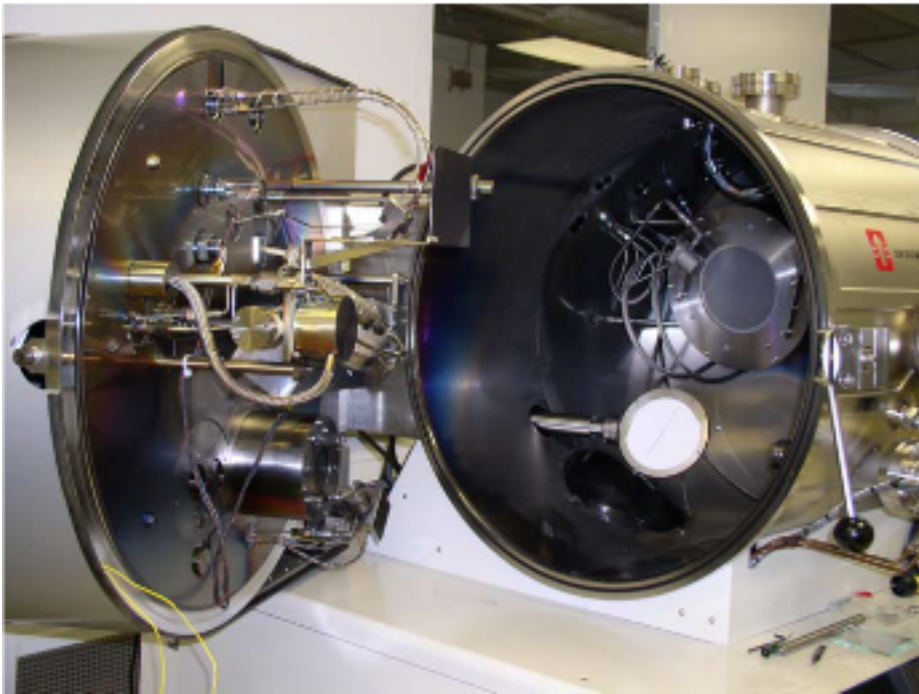


Figure 3-1. Image of IBAD system at ORNL [63]

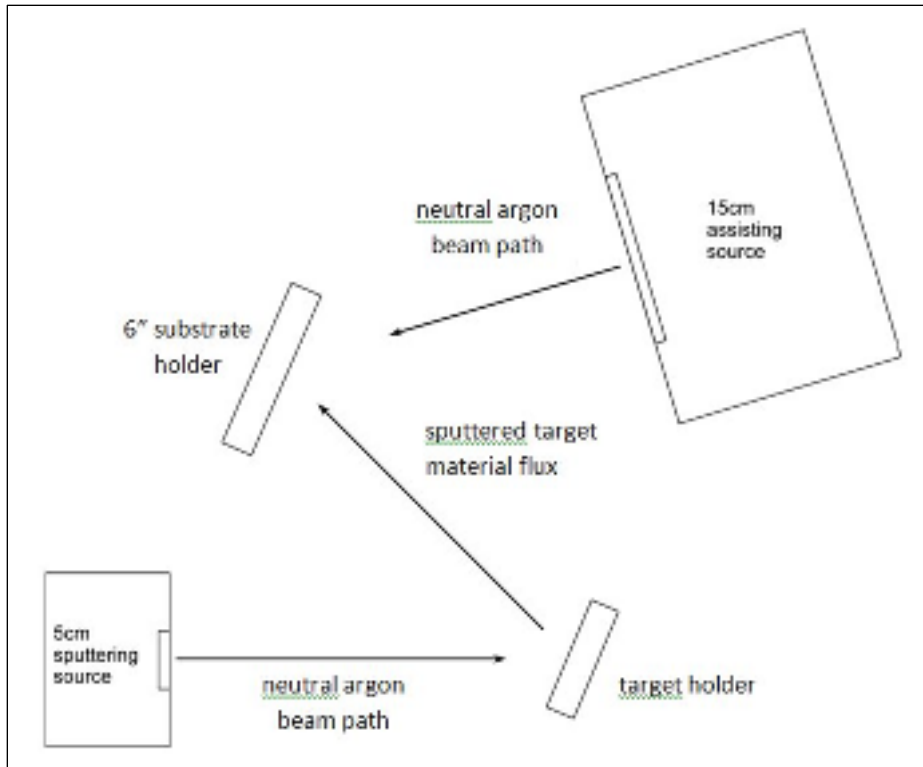


Figure 3-2. Diagram of IBAF chamber and components

As shown in Figure 3-2, the primary ion source, used for sputtering the HA target, is a 5cm Kaufman type ion source, and the assist beam, used for ion bombardment, is a 15cm Kaufman type ion source. The substrate and target holders were positioned using optical paths with respect to the ion sources; the target was positioned at approximately 45° to the primary ion beam (5cm source); the substrate holder was aligned parallel to the target; the secondary ion beam (15cm source) was positioned at approximately 45° to the substrate holder. The primary and secondary beams were focused on the center of the target and center of the substrate holder, respectively. This positioning was done in order to ensure that the substrate holder was sufficiently

exposed to the sputtered HA flux and to the ion bombardment; substrate rotation ensured that each Ti disc within the substrate holder received equal exposure.

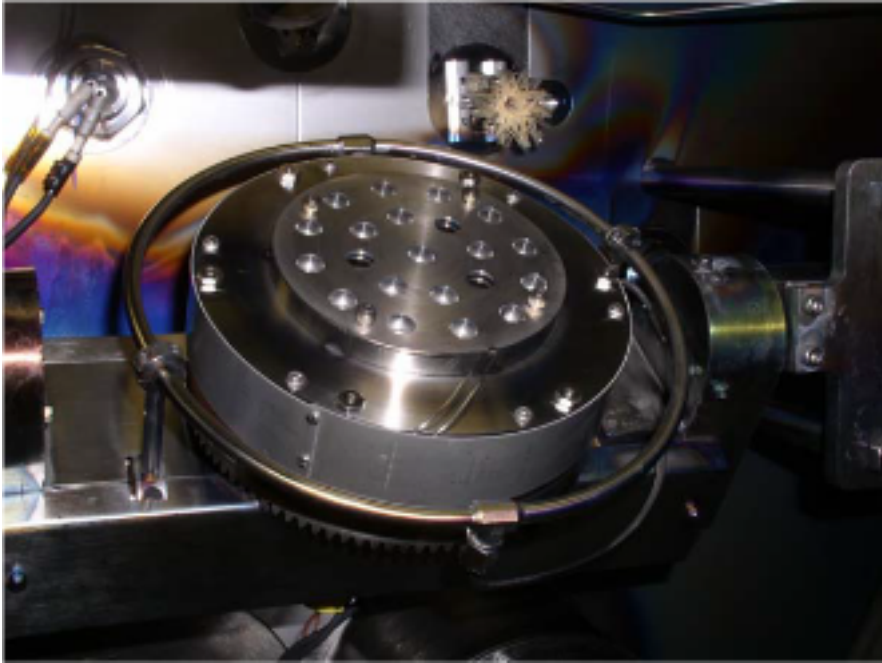


Figure 3-3. Custom-built stainless steel substrate holder for Ti substrates [63]

In situ substrate heating was accomplished using a radiative substrate heater (Momentative Performance Materials), positioned directly behind the substrate holder but without direct contact. A thermocouple fed into the center of the substrate holder was used to monitor substrate temperature during deposition. Vacuum was initiated by a rotary vane mechanical pump, and high vacuum was achieved using a turbomolecular pump; a base pressure of  $5 \times 10^{-5}$  torr was reached before starting each run.

Deposition parameters are listed in Table 3- 1. The secondary beam voltage was gradually reduced over the first four hours of deposition to form an atomically intermixed interface layer and dense HA bottom layer, while maintaining a Ca/P ratio close to that of stoichiometric HA towards the coating surface.

Table 3-1. Deposition parameters for Ag-doped FGHA coatings deposited by IBAD

Time (hrs)	Primary beam		Secondary beam		Substrate temperature (°C)	Substrate rotation
	Voltage (V)	Current (mA)	Voltage (V)	Current (mA)		
1	1200	175	200	50	550	90° at 5 min increments
2			100	50		90° at 15 min increments
2-4			60	30		
5-6			50	30	450	

For comparison of coating properties, an FGHA coating without silver was deposited using another fresh and pure HA target without any silver wires. All coatings were deposited over a total time of 6 hours; with substrate temperatures at 550 °C for the first 4 hours and 450°C for the last 2 hours in order to grow coatings with a graded crystallinity throughout the coating thickness. Coatings processed in this study and their compositions are summarized in Table 3-2.

Table 3-2. Composition of FGHA coatings as determined by XPS

Coating Name	Description	Composition (wt %)	
		HA	Ag
FGHA	Functionally graded hydroxyapatite coating (control)	100	0
FGHA-Ag1	Functionally graded hydroxyapatite coatings with Ag <sup>+</sup> incorporation	98.9	1.1
FGHA-Ag2		96.84	3.16
FGHA-Ag3		93.41	6.59

### 3.3. Analysis of FGHA-Ag coatings

#### 3.3.1. TEM Analysis of coatings

A combined transmission electron microscope/scanning transmission electron microscope, TEM/STEM (Hitachi HF3300) operated at 300kV was used to examine the cross-sectional microstructure of each of the coatings. The cross-section samples for TEM analysis were prepared in a dual-beam focused ion beam (FIB) instrument (Hitachi NB5000) using an in-situ lift-out technique.

#### 3.3.2. Cell detachment study

Murine osteoblastic cells (MC 3T3-E1 cell line) were used in the cell assays in this research; this cell line is a well-established bone-forming cell which exhibits similar behavior with human osteoblastic cells and has been used extensively in biomedical

research as a measure of biological response to orthopedic and dental biomaterials [176,177,178]. Cells were cultured in accordance with standard biological protocol. Prior to cell culture, all glass dishes and substrates were sterilized by autoclaving at 120°C for 30 minutes. MC 3T3-E1 cells were cultured in alpha-modification of minimum essential medium ( $\alpha$ -MEM) supplemented with 10 vol.% fetal bovine serum and 20 mmol/L N-2-hydroxyethylpiperazine-N8-2-ethane sulfonic acid (HEPES) at 37°C under a humidified atmosphere of 5% carbon dioxide in air. About  $2 \times 10^4$  cells were seeded on glass substrates coated with each of the different coating compositions (FGHA, FGHA-Ag1, FGHA-Ag2, and FGHA-Ag3) in a glass dishes (in 20 mL of the medium), and incubated for 20–26 h before the measurement. For this experiment, glass substrates are used rather than Ti for the purpose of viewing cells using the inverted microscope, which is necessary for measurement of cell adhesive area used in shear force calculations. Measurement of cell detachment shear force of each coating (FGHA, FGHA-Ag1, FGHA-Ag2 and FGHA-Ag3) were performed on the same day together with the measurements on a control surface (sterilized microscope slide glass) to increase the reproducibility and validity of the data [174]. By testing at least one coating surface and a control surface on the same day, experimental results of coatings tested on different days can be compared by calculating improvement of cell detachment shear force of a coating compared to its control surface (for that day), and comparing improvement over control for different surfaces.

### 3.3.3. Measurement of shear force necessary to detach a cell from a surface

The method for measuring the shear force necessary to detach a cell from a coating surface was developed at the National Institute for Materials Science (NIMS) in Tsukuba, Japan and described in full detail in the original article [174]. To summarize the method, a cell adhered to the surface of the sample of interest in a dish containing culture medium on the X-Y microscope stage is detached by an applied lateral force.

This force is caused by an AFM-like tip of a cantilever as the stage is moved toward the tip at the speed of 20  $\mu\text{m/s}$ . The shear force applied to the cell ( $f$ ) is given by Equation

$$(1): \quad f = k \delta \quad (1),$$

where  $k$  is the force constant of the cantilever and  $\delta$  is the deflection of the cantilever.

The shear force applied to the cell is recorded as a function of the displacement of the X-Y stage, and displayed as a force-displacement curve. Figure 3-4 shows an example of the force-displacement curve obtained during detachment of a cell:

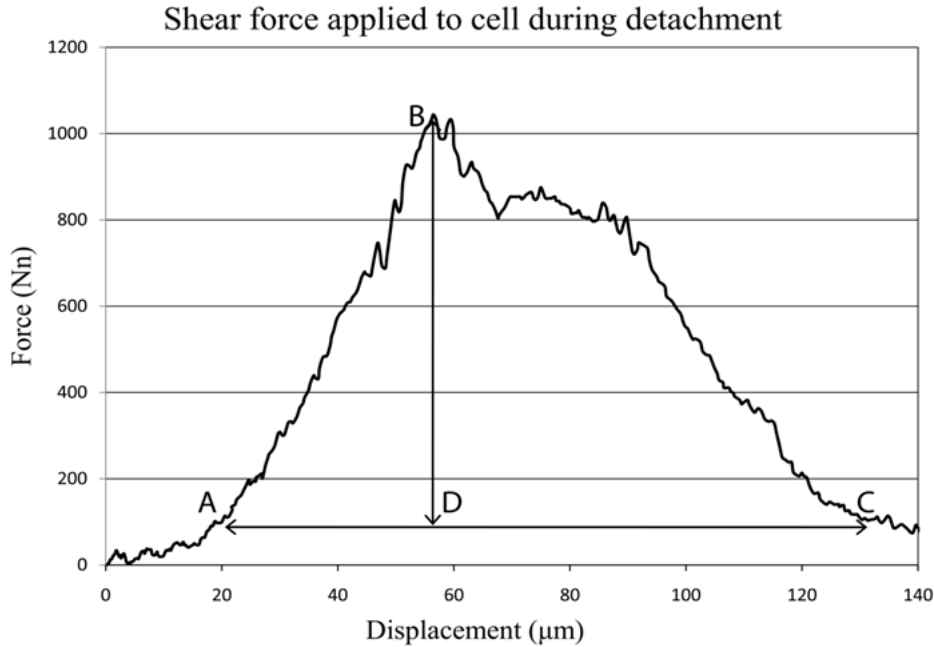


Figure 3-4. Example of force–displacement curve obtained from detachment of a single cell adhered to coating surface

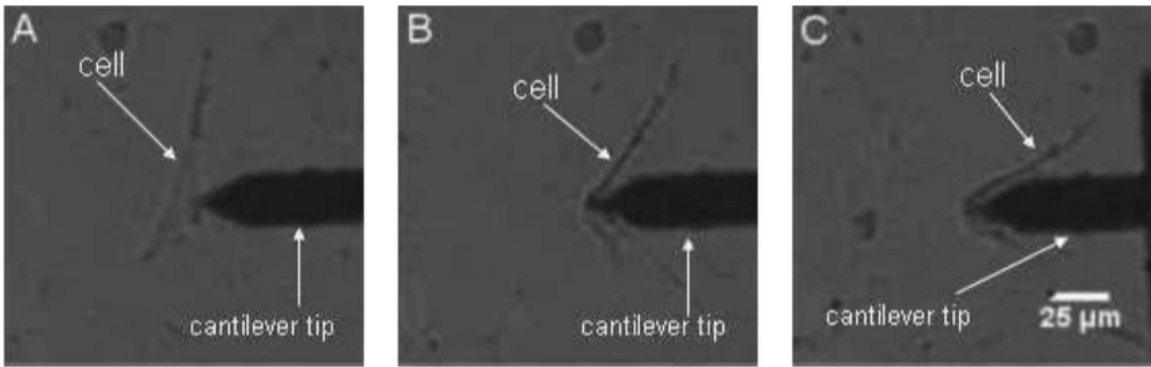


Figure 3-5. Series of images captured from video during cell detachment process. Tip comes into contact with cell (A) shear force is applied to cell as X-Y stage is moved right (B) cell is fully detached as tip has moved across cell adhesive area (C).

Optical images corresponding to this force-displacement curve are indicated in Figure 3-5. Point A corresponds to the first point where the tip of the cantilever touches

the cell. Point B is assumed to be the point where the cell starts to detach from the material. Finally, the cell is completely detached from the material and the shear force applied to the cell decreases to the value found at the beginning of the measurement (point C). The maximum force that appears in the force-displacement curve (B-D in Figure 3-4) is defined as cell adhesive shear force ( $F$ ). The measurement of the cell adhesive shear force of a single cell was performed at room temperature and repeated over at least 20 cells for each dish within 2 hrs after taking the dish out of the incubator. The values of the forces measured were confirmed to have no dependence on the time elapsed after setting the dish on the XY-stage within 2 hrs [174].

#### **3.3.4. Measurement of cell adhesive area**

During the measurement of cell adhesive shear force, the cell was observed using an inverted optical microscope, and the image of the cell was recorded on video tape by CCD camera. Still images of the cell were captured from video and then A/D-converted into  $640 \times 480$  pixels with 256 gray levels using the public domain NIH Image 1.62 program on a Power Macintosh 8500 computer. The converted image was transformed into a binary image by density slicing at an appropriate level to display the outline of the cell, and then the area within the outline was measured. The average shear strength of cell-material adhesion, which herein is called cell detachment shear strength ( $S$ ), is calculated using Equation (2):

$$S = F/A \quad (2)$$

where  $A$  is cell adhesive area.

### **3.3.5. Cell Count**

Approximately  $2 \times 10^4$  cells of MC3T3-E1 were cultured in alpha-modification of minimum essential medium ( $\alpha$ -MEM) supplemented with 10 vol.% fetal bovine by gentle pipetting and then seeded on the surface of each of the coatings in 12-well polystyrene culture plates (Iwaki, Japan). Cells were then incubated for 1, 4 and 7 days at 37°C and 5% CO<sub>2</sub> in humidified air. After incubation, non-adhered cells were removed by rinsing with phosphate-buffered saline (PBS) solution. Cells were then fixed with glutaldehyde and stained with a 10% by volume solution of Geimsa's blue dye.

Cell count was determined by observation of coating surfaces using an inverted optical microscope (Zeiss Axiovert 40 MAT). Areas of each surface were randomly selected, with at least one cell visible on each site. Images were captured using a ProgRes C10 Plus digital camera (Allied High Tech Products Inc., USA) connected to the microscope. The number of cells adhered on each surface after 1, 4, and 7 days incubation was determined by averaging cell counts for each surface and incubation period. The number of cells from at least 5 different areas of each surface and incubation period was counted using AxioVision LE software (Zeiss) and Image J (public domain software created by the US National Institute of Health [179]) and the average number of adhered cells was then determined.

### **3.3.6. Cell Viability Study**

In addition to the cell proliferation study, cell viability can be also be estimated by the WST-1 assay. WST's (water soluble tetrazolium salts) are water soluble dyes that cleave to the formazan dye produced by viable cells. The formazan dye can then be measured colorimetrically at an absorbance of 450nm using a multiwell spectrophotometer. The absorbance of solutions is quantified in order to evaluate and compare metabolic activity among cells in various environments. This method was incorporated as an additional cell study technique to compare cell growth on the FGHA and FGHA-Ag coatings. Samples of each of the FGHA and FGHA-Ag coated titanium were seeded with approximately 1000 MC 3T3-E1 cells in 1.5 ml of alpha-MEM for 1, 4, and 7 days. After 1, 4, and 7 days, culture medium was changed to alpha-MEM without phenol red (for the facilitation of colorimetric reading of WST-1 dye), with 10% WST-1, and inoculated for 4 hours. After 4 hours, the absorbance of each solution was measured with 450 nm wavelength in a multi-plate reader (spectrophotometer). Relative absorbance numbers are recorded and used to evaluate formazan production by viable cells growing on each samples surface at the 1, 4 and 7-day inoculation periods.

### **3.3.7. Silver Release Test**

Silver released from the Ag-doped coatings was measured using photometric determination with a silver reagent kit (HI 93737-01, Hannah Instruments). This well-established method is based on the principle of 1-(2-pyridylazo)-2-naphthol (PAN)

reacting with silver in alkaline media to form a water-insoluble, red-violet complex which can be extracted with organic solvents [180]. The absorbance of the solution at 555nm is directly proportional to the amount of Ag<sup>+</sup> in solution. A calibration line with linear regression ( $R^2 = 0.9506$ ) was first created by measuring the absorbance of solutions of known silver content, created using a standard AgNO<sub>3</sub> solution. AgHA-coated discs of each of the three percentages of Ag doping were immersed in ultra-pure water for 1, 2, 4, 24, 72 and 172 hours in 24-well polystyrene culture plates (Iwaki) and kept in a humidified atmosphere at 37°C to simulate body conditions. After the designated immersion time, the FGHA-Ag coated discs were removed and the remaining solution was reacted with the PAN reagent, followed by reaction with the organic solvents. Five 250µl portions of each of the reacted solutions were transferred into separate wells of a 96-well polystyrene culture plate (Iwaki) and absorption was measured at 555nm. After eliminating statistical outliers as described by Dean and Dixon [181], average absorbance of solutions for each of the three Ag-containing coatings at each immersion time was calculated, and this number was transformed to Ag<sup>+</sup> content (in µg/ml and ppm) by comparison with the calibration line. The calibration line used to transform absorbance number into silver content is shown in Figure 3-6. Although silver content was measured after immersion in ultra-pure water in this experiment, it is demonstrated that this relationship also holds true for silver content in Hank's medium, a synthetic solution with the same pH and concentration of electrolytes found in human physiological fluid.

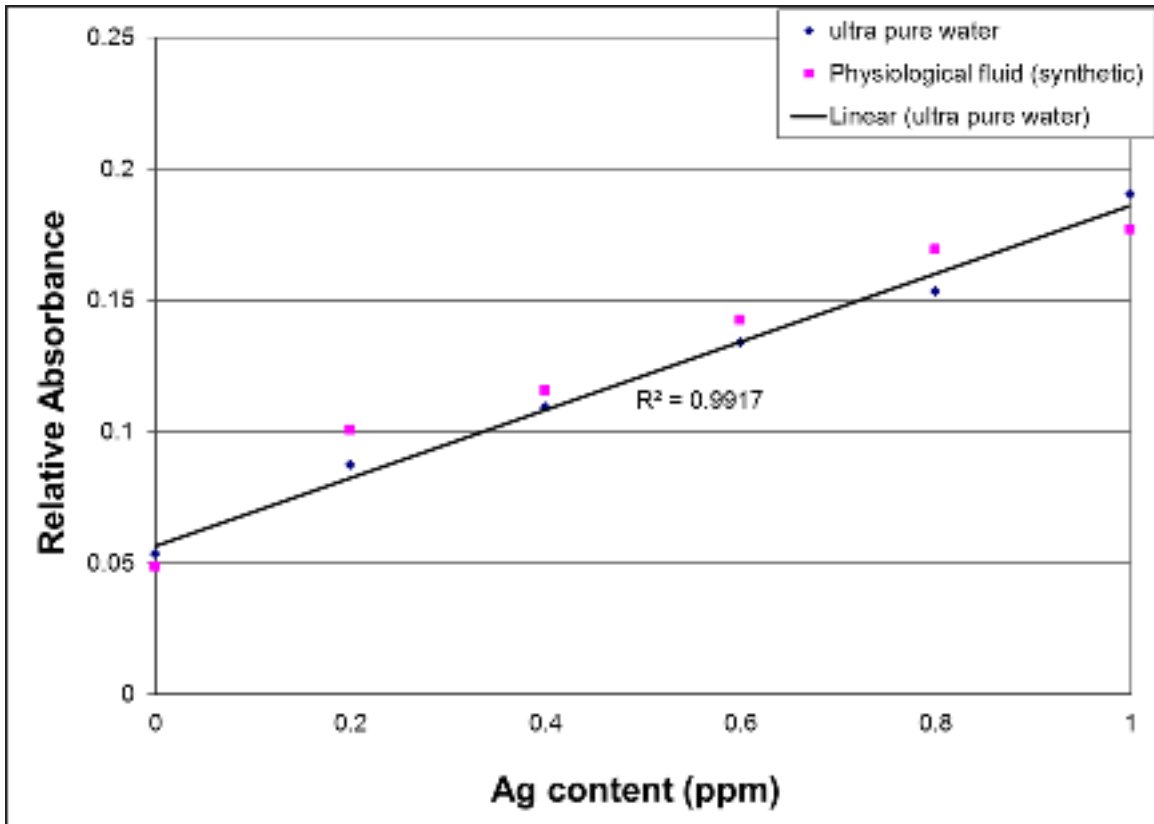


Figure 3-6. Linear regression for silver content vs. absorbance at 550nm

### 3.3.8. Surface Profilometry

Surface roughness of the HA/Ag-coated Titanium discs was measured for all samples before and after immersion in ultra-pure water for 24 hours, to simulate the immediate dissolution of the coatings after implantation. Surface roughness was determined using a Tencor Instruments ALPHA STEP 200 profilometer, with a minimum of 5 scans performed from each surface, with each scan spanning 2mm over

40 seconds, using a stylus force of 17mg. Average roughness values,  $R_a$  – arithmetic average of height deviations from the mean line (ASME B46.1), and Total Indicator Run-out values, TIR – maximum vertical height change over total scan length, were obtained with a maximum resolution of 5nm.

### **3.4. Results**

#### **3.4.1. TEM of coating and coating/substrate interface**

Figure 3-7 shows cross sections of the Ag-doped FGHA coatings from the Ti substrate to the top coating surface.

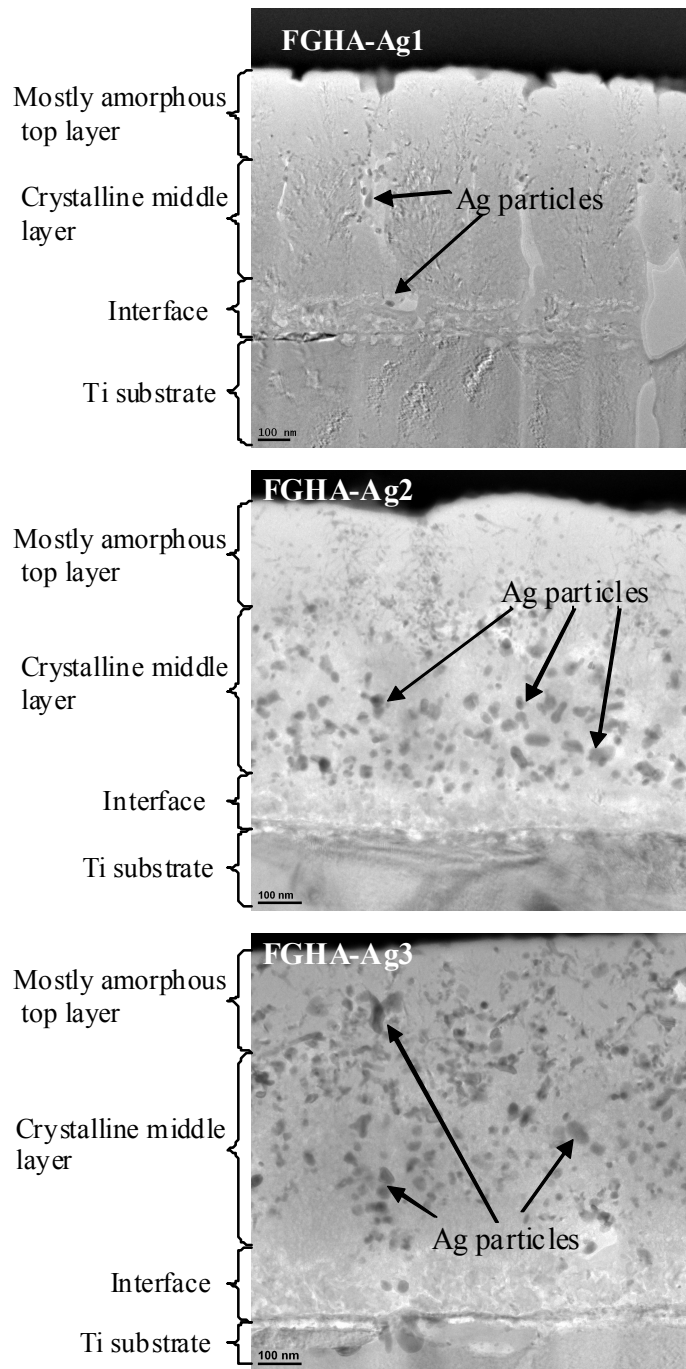


Figure 3-7. TEM cross-sectional micrographs of FGHA-Ag1, FGHA-Ag2 and FGHA-Ag3 coatings [175]

From Figure 3-7, it is observed that coating FGHA-Ag1 contains a columnar grained crystalline structure near the substrate interface, while coatings FGHA-Ag2 and FGHA-Ag3 exhibit an equiaxed nanocrystalline grain structure at the bottom layer due to Ag particles acting as nucleation sites for equiaxed grain formation. Decreased crystallinity in the top two layers is a result of decreased in situ substrate temperature during deposition [182]. Effects of this graded crystallinity can be seen in ion release and surface roughness measurements to follow.

### 3.4.2. Evaluation of cell affinity to coating surfaces by cell detachment shear force measurement

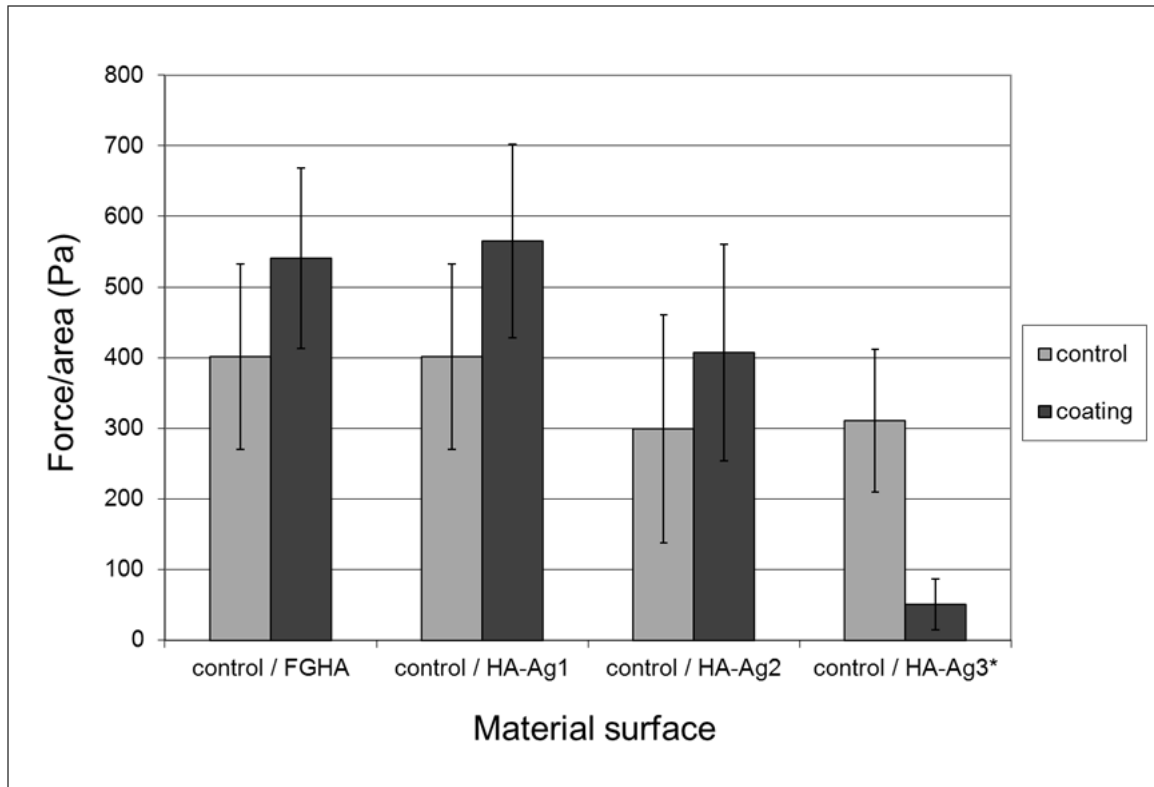


Figure 3-8. Summary of cell detachment shear force measurements, showing average shear force (normalized by cell adhesive area) applied to cells to detach from the surface [167]

Figure 3-8 illustrates the average cell detachment shear strength of each coating surface, compared to the control surface tested on the same day with the same conditions (cantilever tip, room temperature, cell passage, and time of cell seeding) to confirm the reproducibility of results. Cell adhesive shear strengths shown in Figure 3-8 represent the average shear force necessary for detachment of at least 20 cells per surface, normalized by the cell adhesion area.

FGHA-Ag1 coating surface shows the most improvement in cell adhesion shear strength (164.0 Pa increase with respect to control surface) compared to FGHA (139.6 Pa increase) and FGHA-Ag2 (108.2 Pa increase). It should be noted that FGHA-Ag1 and FGHA coating surfaces were measured on the same day, and therefore are compared to the same control surface. FGHA-Ag3 surface had a significantly lower cell adhesive shear strength compared to the glass control surface; on this surface, very few cells were adhered, causing difficulty in measurement. Cells that were adhered to FGHA-Ag3 were very weakly attached, as indicated in Fig. 3-8.

### **3.4.3. Cell culture assay**

Figures 3-9 through 3-11 show optical micrographs of the MC 3T3-E1 cells on FGHA and FGHA-Ag surfaces after fixing and staining at time periods of 1, 4, and 7 days. In addition to the number of cells attached, these images can be used to understand the condition of the cells on each surface; cells in a normal, healthy state exhibit spreading of the extracellular matrix (lighter blue appearance as opposed to dark blue cell nucleus), whereas cells in an unhealthy or dying state appear rounded and compact, without a well-spread extracellular matrix. The condition of cells during initial attachment is highly dependent upon the biocompatibility of the surface to which they are attached [174,175] and is therefore a good indicator in determining bioactive surfaces.

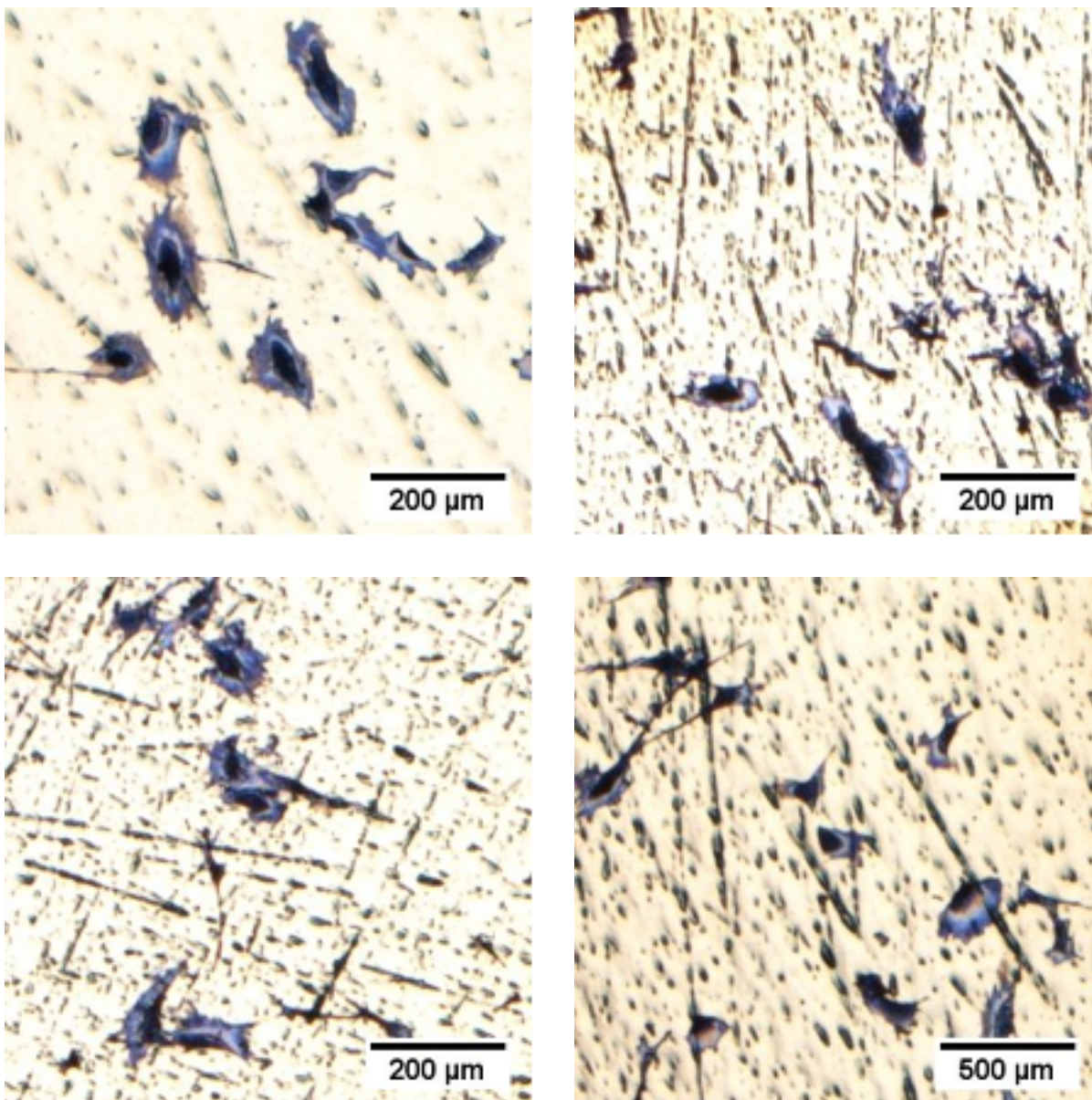


Figure 3-9. Optical micrographs of sample surfaces A) FGHA coating (top left), B) FGHA-Ag1 coating (top right), C) FGHA-Ag2 coating (bottom left), and D) FGHA-Ag3 coating (bottom right) after 24-hour cell culture

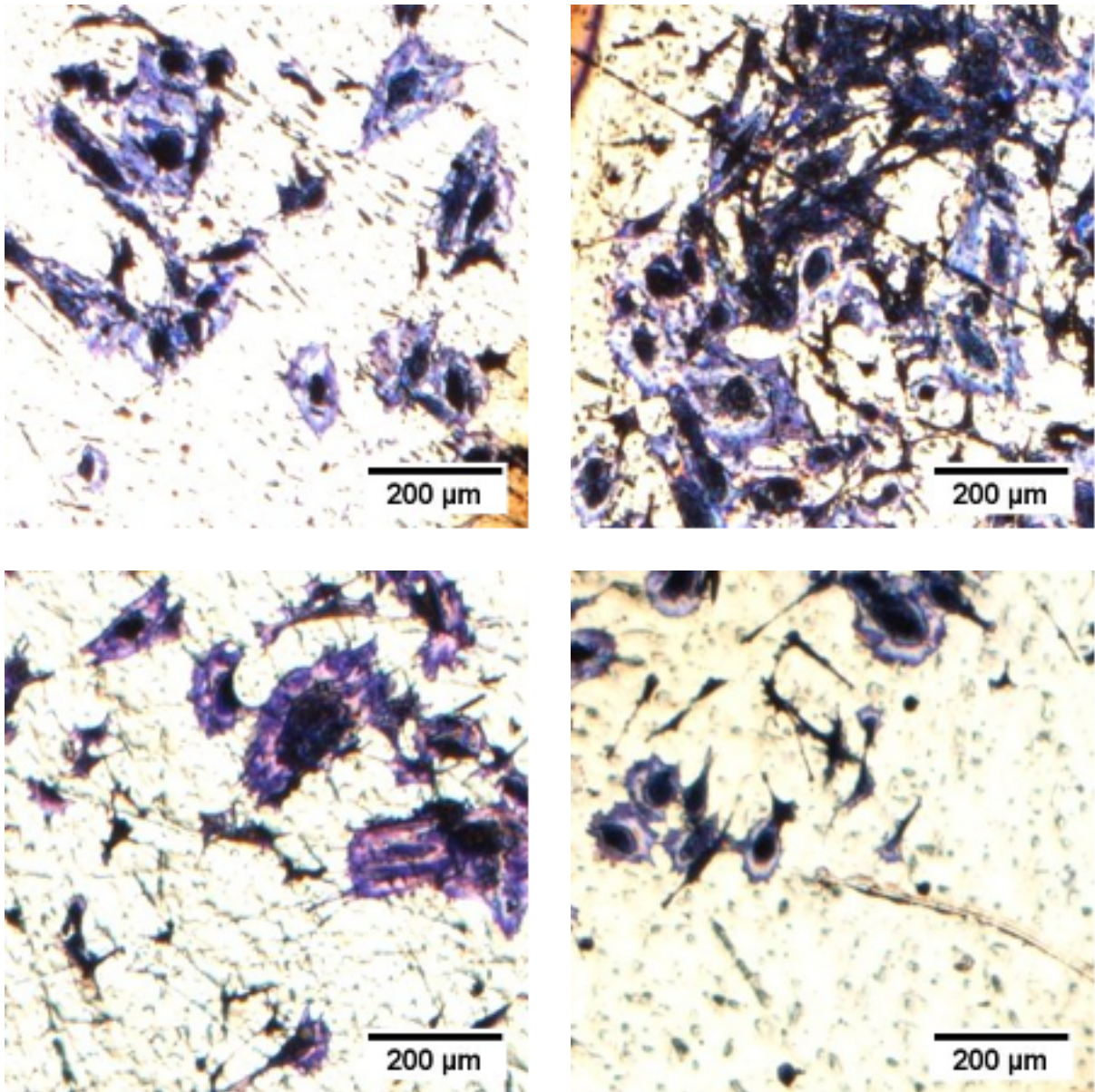


Figure 3-10. Optical micrographs of sample surfaces A) FGHA coating (top left), B) FGHA-Ag1 coating (top right), C) FGHA-Ag2 coating (bottom left), and D) FGHA-Ag3 coating (bottom right) after 4-day cell culture

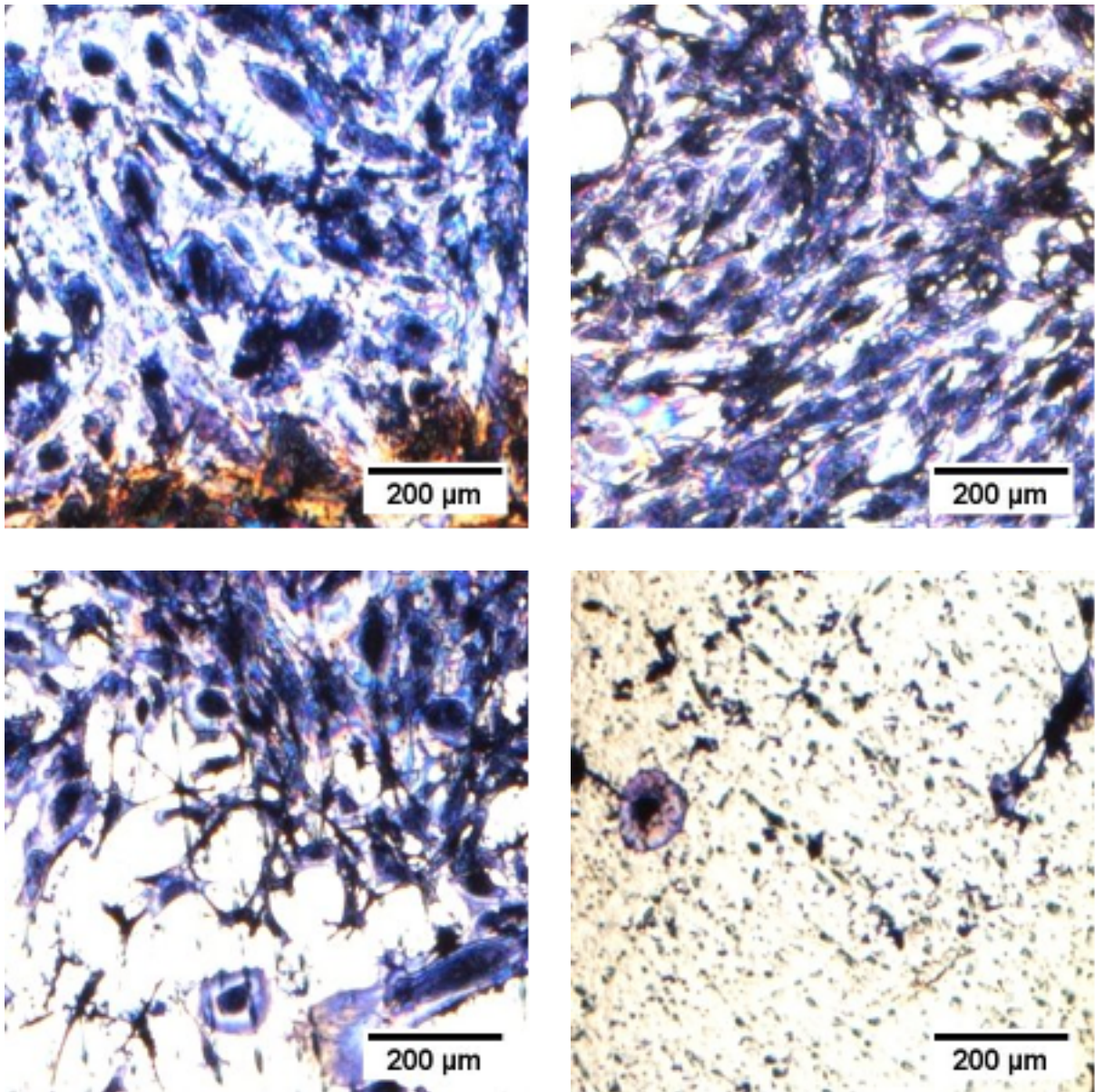


Figure 3-11. Optical micrographs of sample surfaces A) FGHA coating (top left), B) FGHA-Ag1 coating (top right), C) FGHA-Ag2 coating (bottom left), and D) FGHA-Ag3 coating (bottom right) after 7-day cell culture

Shown in Figures 3-9 through 3-11 and summarized in Figure 3-12, the osteoblast cells attach and proliferate (multiply) in a normal manner on all surfaces except that of the FGHA-Ag3 coating surface. Cells attached to FGHA, FGHA-Ag1 and FGHA-Ag2 coating surfaces appear well spread, with a large extracellular matrix surrounding the nucleus, indicating that the cells are in a healthy state; however, on FGHA-Ag3 coating surface, the attached cells are fewer in number at each time period, and appear rounded and unspread, indicating a low affinity for that surface.

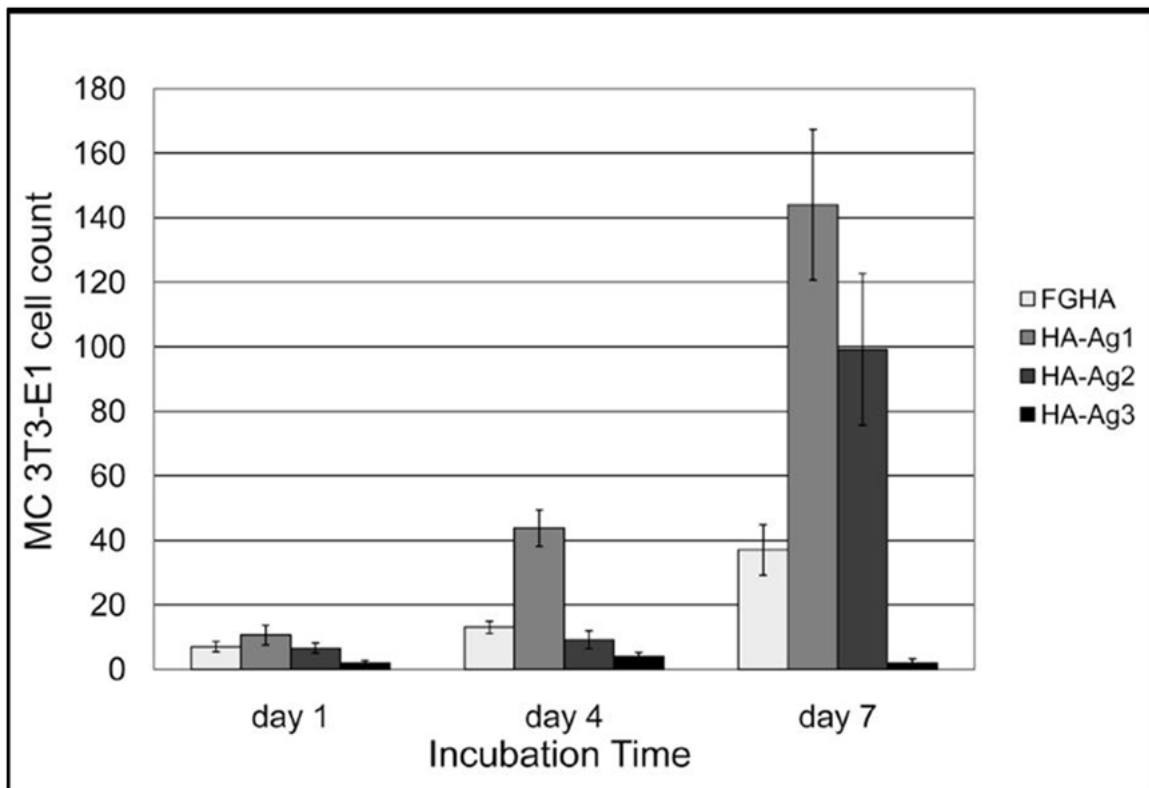


Figure 3-12. Average number of MC 3T3 osteoblast cells counted on each of coating surface at different incubation times.

Figure 3-12 shows the average number of MC 3T3-E1 cells counted on each of the coating surfaces after 1, 4 and 7 days of incubation. FGHA-Ag1 coating shows a higher number of adhered cells at each of the incubation periods, with FGHA-Ag2 having the next highest number after 7 days. Three of the coatings, FGHA, FGHA-Ag1 and FGHA-Ag2, show an exponential increase in the number of cells grown with respect to incubation time, while the average number of cells grown on FGHA-Ag3 does not increase over time, indicating an unhealthy environment on the coating surface of FGHA-Ag3 which does not promote cell growth.

#### 3.4.4. WST-1 Assay

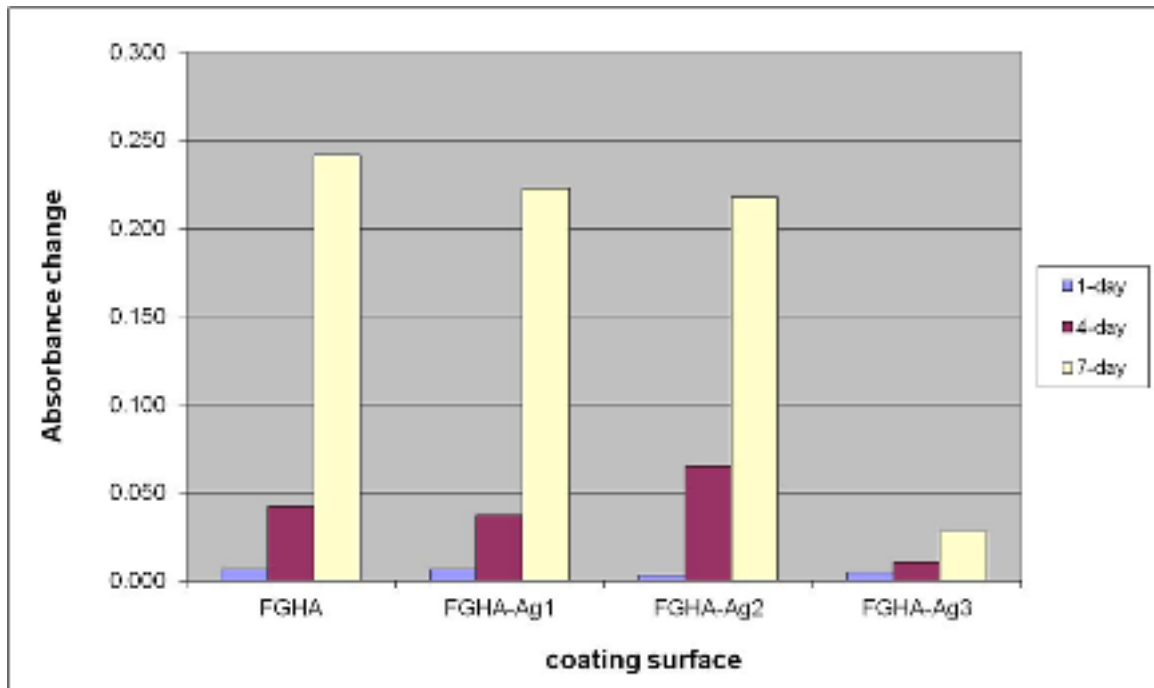


Figure 3-13. Relative viability of cells by WST-1 assay

Shown in Figure 3-13, coatings FGHA, FGHA-Ag1 and FGHA-Ag2 resulted in an exponential increase in WST-1 absorbance over the 7-day incubation period, indicating a rise in production of the formazan salt associated with cell viability; this is the typical behavior of cells undergoing healthy growth and proliferation. Coating FGHA-Ag3 resulted in only small increases in formazan production, indicating a low degree of cell proliferation and/or growth of cells.

### 3.4.5. Ag release test

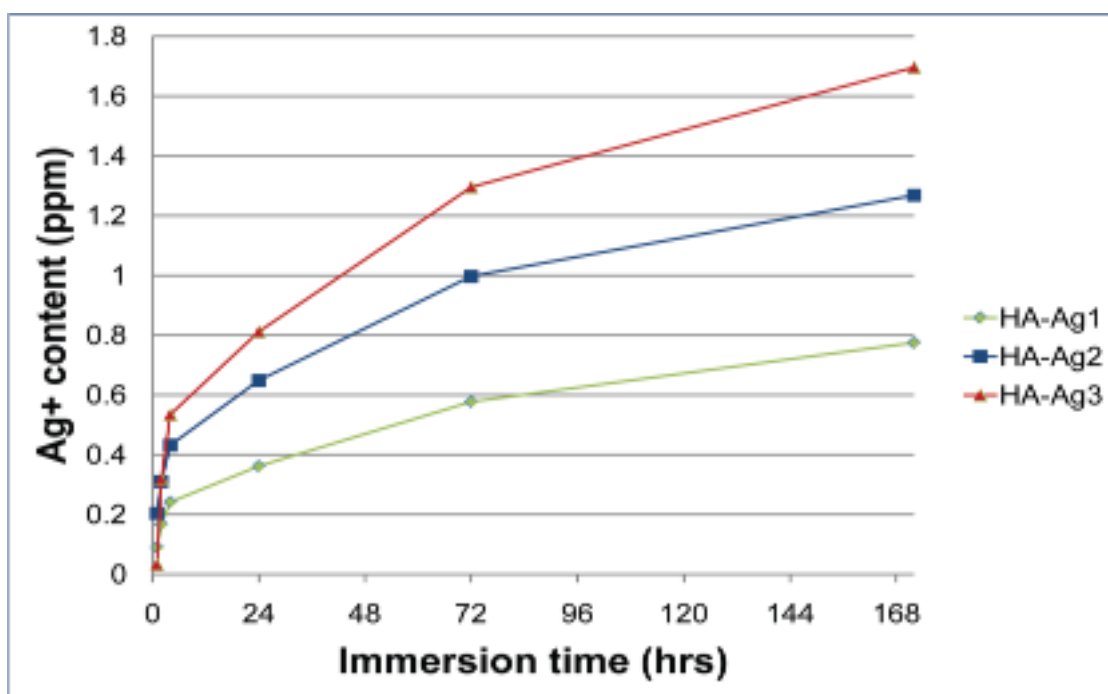


Figure 3-14. Release of Ag<sup>+</sup> ions from each of the Ag-doped FGHA coatings immersed in USP water over time.

The release of silver ions from each of the three Ag-doped coatings into ultra-pure H<sub>2</sub>O as a function of time is illustrated in Figure 3-14. As expected, FGHA-Ag3 coating released the highest amount of Ag, resulting in about 1.7 ppm (10.2 µg/ml) after 172 hours, compared to 1.27 ppm (7.6 µg/ml) and 0.78 ppm (4.6 µg/ml) for FGHA-Ag2 and FGHA-Ag1 coatings, respectively. For all of the three coatings, silver ions released quickly from the coatings in the first few hours, and then the release rate decreased after 4 hours.

### 3.4.6. Surface Roughness

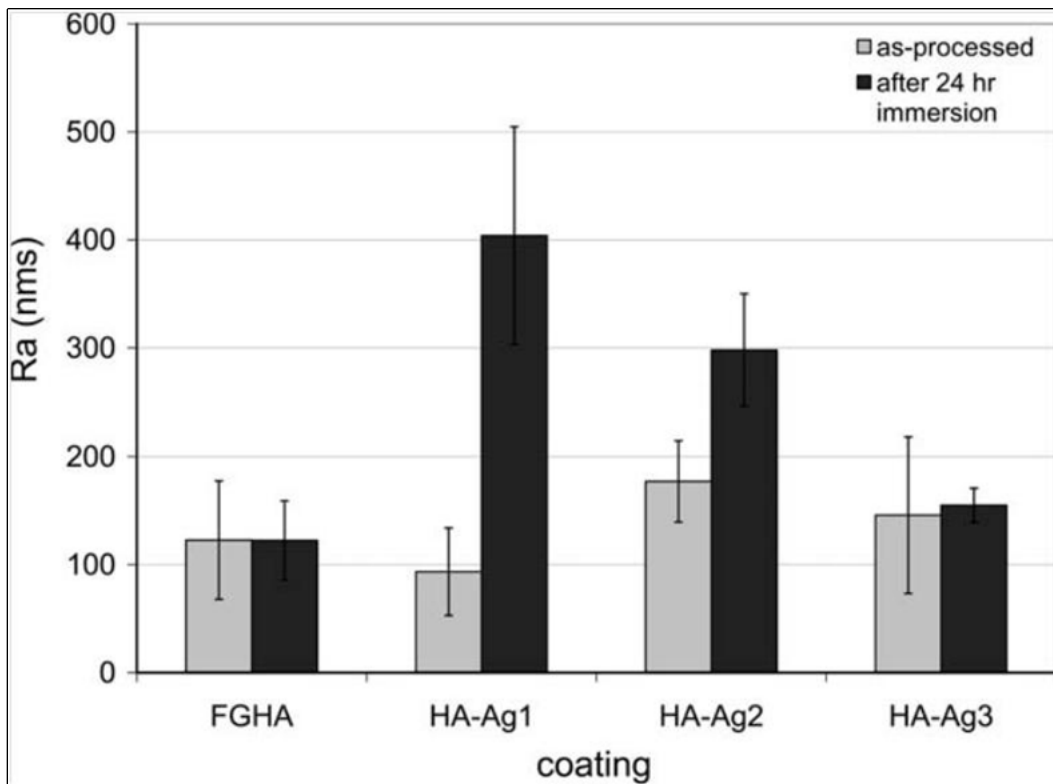


Figure 3-15. Surface roughness average ( $R_a$ ) of each coating surface measured before and after immersion in culture medium.

Figure 3-15 shows the roughness average, Ra, for coatings FGHA, FGHA-Ag1, FGHA-Ag2 and FGHA-Ag3 before and after 24 hr immersion in ultrapure H<sub>2</sub>O. It can be seen that, before immersion, surface roughness of the four coatings is similar (Ra ~ 100 nms), with FGHA-Ag2 having a slightly higher roughness. After immersion however, FGHA-Ag1 and FGHA-Ag2 coating surfaces having significantly higher surface roughnesses, Ra = 404 +/- 101 nms and 298 +/- 51.2 nms, respectively, while the other surfaces remained in the range 100 to 200 nms, similar to their surface roughness before immersion.

### **3.5. Discussion**

In our previous study, bioactivity of FGHA coating (without silver) was observed. [40] FGHA coating surfaces seeded with ATCC CRL 1486 human embryonic palatal mesenchyme (HEPM) cells, an osteoblast precursor cell line, have shown a denser cell layer with a higher expression of integrin anchoring proteins after 24 hrs when compared to the titanium control surface [40]. In the research presented in this chapter, osteoblast response and dissociation characteristics of FGHA coating and of three Ag-doped FGHA coatings are examined to determine optimal silver content.

According to the measurement of cell detachment shear strength and cell count on each of the coatings, FGHA-Ag1 coating surface exhibits the highest bioactivity indicated by a higher average cell detachment shear strength and a greater number of MC 3T3-E1 cells observed on the surface after 1, 4 and 7 days of incubation. Results of

the cell detachment assay indicated that FGHA-Ag2 surface has lower cell affinity than FGHA coating surface, determined by its lower improvement in average cell adhesive shear strength. However, FGHA-Ag2 coating surface performed better according to basic cell count at each incubation period, observed by fixing and dyeing MC 3T3-E1 cells on all coating surfaces. It is assumed that the amount of silver released from FGHA-Ag1 and FGHA-Ag2 coatings is not toxic to cells. FGHA-Ag3 coating may exhibit relatively high cytotoxicity, as indicated by the low number of adhered cells from cell culture assays and poor cell adhesive shear strength seen in cell detachment results.

Preliminary results show the Ag-FGHA coatings exhibit a desirable release of Ag<sup>+</sup>, with a rapid release rate directly after immersion, followed by decline to an almost steady Ag<sup>+</sup> concentration. FGHA-Ag3 had the fastest and highest release of Ag<sup>+</sup> which reached 0.81 ppm (4.9 µg/ml) after 24h, followed by FGHA-Ag2 with 0.65ppm (3.9 µg/ml) after 24h. FGHA-Ag1 has the lowest release of 0.36ppm (2.2 µg/ml) after 24h immersion. According to the result of a cytotoxicity evaluation by colony formation assay using MC3T3-E1 [183], the concentration of AgNO<sub>3</sub> reducing plating efficiency (ratio of colony formation) to 50% is  $2.77 \times 10^{-6}$  mol/L, which is equivalent to 0.298ppm. Only a few percent of cells could proliferate around AgNO<sub>3</sub> concentration of  $1 \times 10^{-5}$  mol / L, which is equivalent to 1.07ppm, and no cells could survive over  $2 \times 10^{-5}$  mol/L, which is equivalent to 2.14ppm. Based on these data, Ag<sup>+</sup> release of FGHA-Ag3 after 172 hours is very close to AgNO<sub>3</sub> concentration that completely inhibits the proliferation of MC3T3-E1, whereas Ag<sup>+</sup> release of FGHA-Ag1 after 172 hours is in the range of the

concentration in which cells could survive. This suggests that the cell count and average cell detachment shear strength is controlled by the release rate of Ag<sup>+</sup> from FGHA-Ag coatings. However, further evaluation is needed to determine the release profile of Ag<sup>+</sup> in cell culture medium accompanied by Ca<sup>2+</sup> and PO<sub>4</sub><sup>3-</sup> release from Ag-FGHA coatings. Silver buildup in the body after release from Ag-containing coatings has been a concern with respect to possible negative effects, however it has been shown that silver ions released within the body in low amounts are eventually processed and removed during normal kidney function and do not pose any long-term adverse health effects [184].

Surface profilometry of coatings as-processed revealed roughness average, Ra, was in the range of 100-200 nms for all coating surfaces. As-processed coating surface roughness is expected to be similar for all coatings due to identical substrate preparation before deposition as well as substrate rotation and heating during deposition, ensuring uniform coating thickness and growth direction. Roughness average before immersion is most likely directly related to surface roughness of the titanium substrates before coating deposition, which would explain the similarity in Ra among all coatings. However, after immersion in ultra-pure water for 24 hours, roughness averages of FGHA-Ag1 and FGHA-Ag2 increased significantly to approximately 400 nms and 300 nms, respectively, while FGHA and FGHA-Ag3 roughness averages remained close to 100 nms. Increasing surface roughness of HA surfaces has been shown to increase osteoblastic cell adhesion, proliferation and detachment strength [185]. While surface roughness of HA in the latter study is

deliberately caused by a preparation technique, variations in surface roughness in the present study occur after immersion due to the difference in dissolution rates among the four coatings. Increased dissolution of calcium phosphate materials has been shown to promote osteoblast attachment in recent studies [186]. This observation is seen in the success of FGHA-Ag1 in initial osteoblast cell attachment and higher average attachment shear strength.

### **3.6. Summary**

In summary, the dissolution properties and biological response to functionally graded hydroxyapatite coatings doped with various amounts of silver have been investigated in this research. Coating deposition process by IBAD has been previously studied and optimized in terms of physical, mechanical and composition properties [63]; however, the dissolution behavior and effects of silver incorporation on osteoblast cell response were unknown. It was found that Ag was released rapidly at first, and then gradually decreased to a near constant concentration, owing to the functionally graded microstructure of the coatings; the amorphous top HA layer dissolves at a high rate, releasing silver particles which are dispersed throughout the coating cross-section at a correspondingly high rate; once the top amorphous layer has dissolved, the mostly crystalline layer dissolves at a slower rate, releasing less silver as result. Osteoblast cell proliferation was seen on all surfaces, however a very low number of cells remained attached to the FGHA-Ag3 coating, suggesting that its high

silver content (6.6 wt%) may be toxic to cells. A similar trend was observed in the measurement of the cell attachment shear strength on each surface; FGHA, FGHA-Ag1 and FGHA-Ag2 coating surfaces promoted an increase in cell attachment shear strength, as compared with the control group, while FGHA-Ag3 coating surface resulted in much weaker cell attachment. It was concluded that FGHA-Ag3 coating contained an excessive amount of Ag which was toxic to osteoblast cells. Optimal Ag-doping for FGHA coatings is suggested to be in the range exhibited by FGHA-Ag1 and FGHA-Ag2 (between 1 and 3 wt%), in order to release Ag at a sufficient rate as to produce an antibacterial effect, while maintaining an Ag concentration that does not inhibit the growth of osteoblast cells.

## CHAPTER 4: HYDROXYAPATITE COATINGS ON PEEK SUBSTRATES

### 4.1. Introduction

In the previous works conducted by the Advanced Materials Research Laboratory, titanium was successfully coated with hydroxyapatite using a physical vapor deposition method (ion beam assisted deposition) to obtain a functionally graded crystalline coating with excellent physical and microstructural qualities. Titanium is a suitable bulk material for many orthopedic and dental implants, such as the femoral stem of a hip implant, dental posts, fracture fixation plates, bone screws, etc. However, for the application of spinal fusion cages, titanium has limitations of 1) interfering with X-rays and other radiation-based evaluation techniques that are used to assess a patient's recovery following spinal fusion surgery and 2) causing weakening of adjacent vertebrae due to the mechanical stiffness mismatch between titanium and bone via stress shielding. Recently, PEEK has emerged as an optimal substitute for titanium in the development of spinal fusion cages. PEEK has suitable mechanical properties, is radiolucent, and has been recognized by the FDA as an implantable biomaterial; however, while biocompatible, PEEK surfaces are not bioactive due to the chemical dissimilarity compared with bone. PEEK therefore does not actively participate in the formation of new bone. For this reason, several techniques have been studied with the aim of achieving a bioactive implant surface while retaining the benefits of PEEK as the bulk material. The current commercial method used in the production of PEEK spinal

fusion cages is HA coating by the plasma-spraying method. While plasma-sprayed HA coatings can promote greater bone attachment, several problems have been cited including weak coating adhesion and non-homogenous microstructure, which lead to rapid dissolution of coating and can ultimately cause implant loosening and failure. In order to improve the quality of HA coatings and of the substrate/coating interface, the research presented in this chapter will investigate the deposition of a bilayer coating of YSZ and HA onto PEEK substrates by radio frequency magnetron sputtering, a physical vapor deposition method. Coating adhesion will be studied and optimized using stud-pull coating adhesion strength testing and optical microscopy. Attempts will be made to crystallize the amorphous as-sputtered HA coating using heat treatment methods that are suitable for the thermal properties of the PEEK polymer substrates. The microstructure and composition of the coatings will be studied with scanning electron microscopy (SEM) with energy dispersive spectroscopy (EDS), X-ray diffraction (XRD), Fourier transform infrared spectroscopy (FTIR) and optical microscopy. Finally, biological response will be evaluated through cell culture tests.

## **4.2. Materials and Methods**

### **4.2.1. Preparation of PEEK substrates**

The PEEK substrates used in this research are implant grade PEEK Optima®(Invibio) discs of ¼" height with ½" diameter, machined from PEEK rods of 1' length and ½" diameter. PEEK Optima rods are shown in Figure 4-1; after machining, substrates of

described dimensions are shown in Figure 4-2. Prior to deposition, the PEEK discs were prepared by wet grinding with 240, 400, and 600 silicon carbide paper (Buehler) and subsequent polishing with 9, 3, and 1  $\mu\text{m}$  polycrystalline diamond suspension (Buehler) using an automated grinding and polishing machine (Buehler), shown in Figure 4-3. In between grinding and polishing steps, the discs were washed and ultrasonically cleaned to prevent cross contamination of abrasive particles, using sonic bath cleaner (Ultramet 2002), shown in Figure 4-4. After polishing, the discs were ultrasonically cleaned in acetone and isopropanol alcohol for 10 min each, dried by compressed air and then stored in sterile culture plates, and kept in a dessicator until deposition.



Figure 4-1. PEEK rods of 1 ft length and  $\frac{1}{2}$ " diameter before cutting

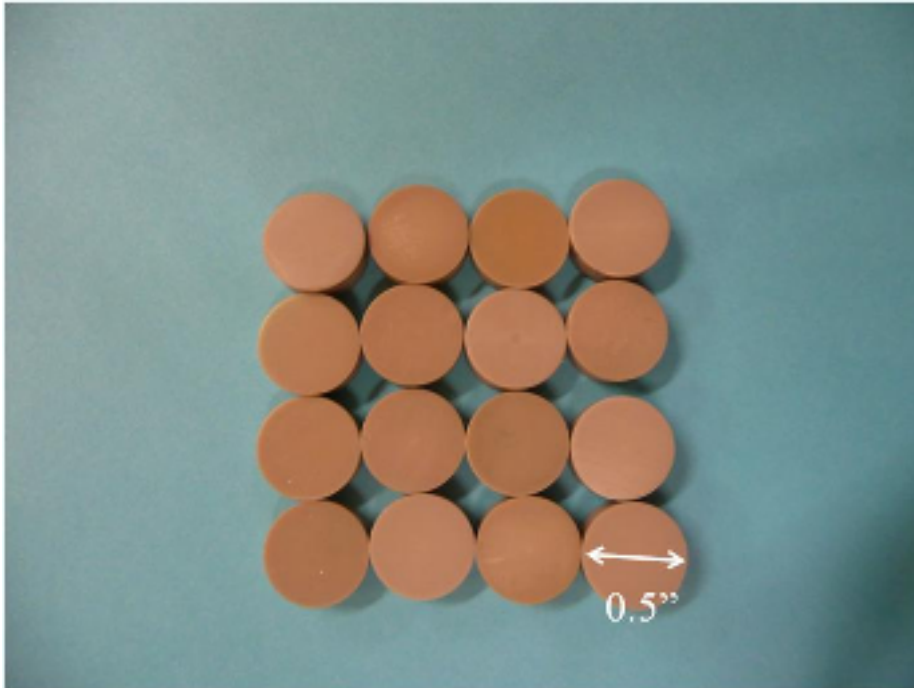


Figure 4-2. PEEK substrates of  $\frac{1}{2}$ " diameter,  $\frac{1}{4}$ " height



Figure 4-3. Grinding and polishing station (Buehler)



Figure 4-4. Sonic cleaner (Buehler)

#### **4.2.2. Plasma activation of PEEK substrates**

Prior to inserting the polished and cleaned PEEK samples into the vacuum chamber of the RF sputter deposition system for coating, the PEEK substrates were exposed to an oxygen plasma in order to alter the surface chemistry of the polymer to enhance bonding of the sputtered film to be deposited. This was accomplished using a radio frequency plasma barrel reactor (model PM-600 by March Instruments Inc.), shown in Figure 4-5, in the nanofabrication facility of NCSU.



Figure 4-5. RF plasma barrel reactor

This system is designed for stripping, cleaning and etching, (typically of semiconductor materials) using oxygen gas to create the plasma. Base pressure is approximately 50 millitorr, which is achieved using a rotary vane mechanical pump. Oxygen partial pressure of 600 mTorr was established prior to striking the plasma. Power was set to 300W, and sample (5 per set) were treated for 5, 10, 15, 20 and 25 minutes, creating 5 sets with different exposure times in order to measure the effect on subsequent coating adhesion. After plasma exposure, each sample set was transferred into vacuum chamber of the RF magnetron sputter system for coating deposition.

#### 4.2.3. Conditioning of sputtering targets before use

Sputtering targets were purchased from Kurt J. Lesker Company for use in a radio frequency (RF) magnetron sputtering system. Targets were 1) 99.9% pure HA of 3.00" diameter and 0.125" thickness, secured to a 0.125" copper backing plate by elastomer bonding and 2) YSZ ( $ZrO_2$  - 93 at%,  $Y_2O_3$  - 7 at%) of 2.00" diameter and 0.125" thickness, also elastomerically bonded to a 0.125" copper backing plate. Sputter targets are shown below in Figures 4-6 and 4-7.

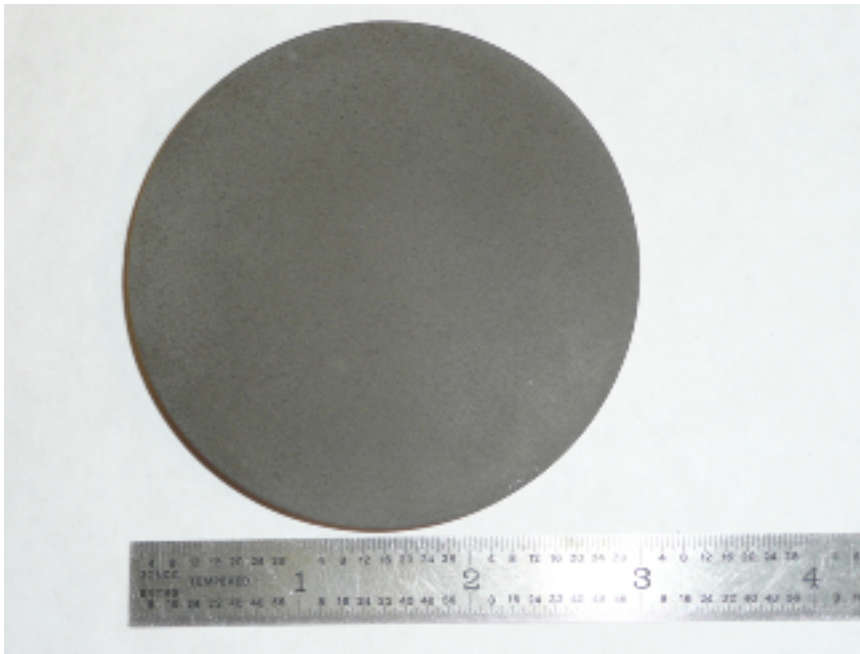


Figure 4-6. Hydroxyapatite sputter target [Kurt J. Lesker Co.]

As per manufacturer's recommendations, both targets were "preconditioned" prior to use in coating deposition for the purpose of preventing premature cracking of the ceramic sputter targets due to thermal shock. This was performed by installing the

sputter targets into the RF sputter system and slowly increasing RF power by a rate of 20-25 Watts every 5 minutes. This gradual ramp-up procedure was also performed during the first several coating trials.

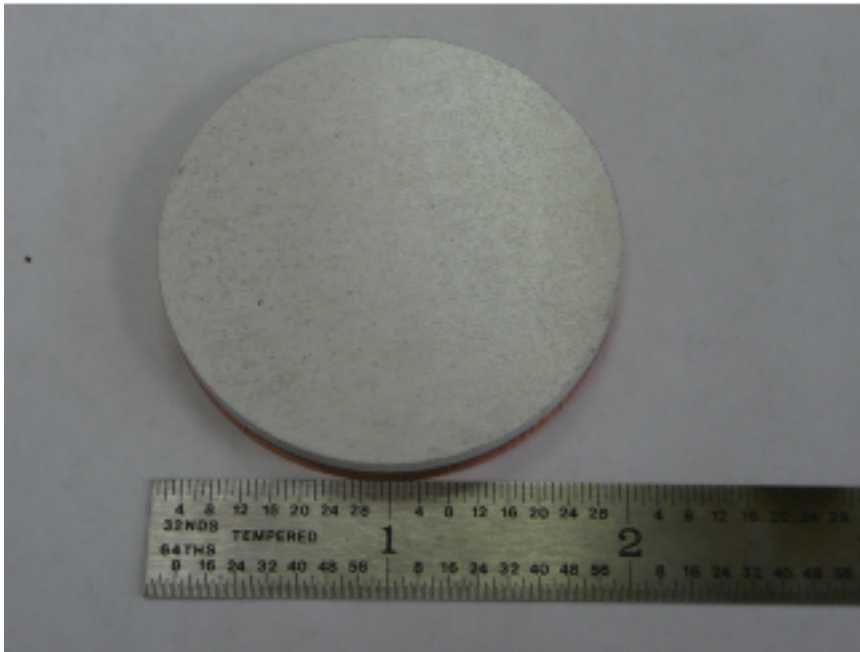


Figure 4-7. Ytria-stabilized zirconia sputter target [Kurt J. Lesker Co.]

#### 4.2.4. Radio Frequency Magnetron Sputtering System

HA/YSZ coating were deposited onto PEEK substrates using a radio-frequency (RF) magnetron sputtering system located in the Nanofabrication Facility (NNF) cleanroom at North Carolina State University. An image of this system is shown in Figure 4-8. The RF magnetron sputter tool is equipped with two sputter sources that accept either 2" or 3" targets and can be used to deposit a wide variety of materials. A

rotary vane pump, using fomblin oil, is used as a roughing pump to achieve the initial vacuum level of approximately 100 mTorr. At this pressure crossover, the vacuum system is manually switched over to high vacuum, which is achieved by a turbomolecular pump. The base pressure of the system is approximately  $2 \times 10^{-7}$  Torr. To insure that no oil vapors are introduced into the chamber, a dry pump is used to achieve the initial pump down from atmospheric pressure. An MKS 600 pressure controller (MKS Instruments) is used to set and maintain the Argon working pressure used in creating the plasma. The RF power is supplied by an RFX-600 RF power generator (Advanced Energy); an AFX-600 digital matching network (Advanced Energy), is used to match the impedance of the plasma and tune the desired power. Sputter targets (and sources) are cooled using a pump to supply a flow of ice water to the backing plates of the target holders. The substrate stage height is adjustable within a wide range, and substrate rotation speed can also be varied.

#### **4.2.5. Coating Deposition**

The target-to-substrate distance was studied and found to be optimized in terms of coating adhesion strength and sputter rate at a distance of 86mm. Substrate rotation was used in order to ensure homogeneity of coating thickness and microstructure across all samples. The base pressure of approximately  $2 \times 10^{-7}$  Torr was reached before deposition was initiated.

The initial layer of YSZ was deposited over 8 hours at an RF power of 80 watts, resulting in a thickness of 400-450nm. The HA layer was then deposited over 6 hours at an RF power of 150 watts, resulting in a thickness of 700-800nm. Final coating thickness of the YSZ/HA dual layer coating was approximately 1.2  $\mu\text{m}$ . Deposition parameters are listed in Table 4-1.

Table 4-1. RF Magnetron Sputtering Deposition Parameters

Time (hrs)	Power (Watts)		Deposition Rate (nm/hr)	Ar pressure (mTorr)	Substrate rotation (rpm)
	Gun1 (YSZ)	Gun2 (HA)			
0-8	80	0	50-60	10	3
8-14	0	150	~120		



Figure 4-8. Image of RF Magnetron Sputtering system at NNF Cleanroom of NCSU

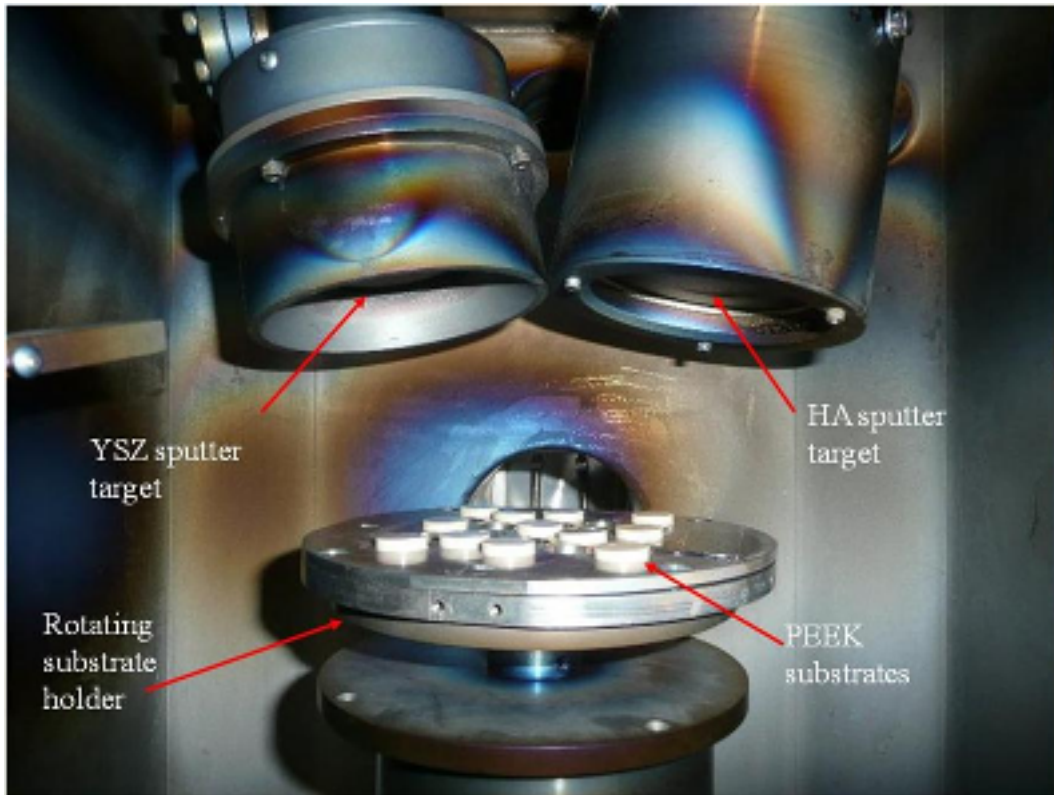


Figure 4-9. Image of inside of RF Magnetron Sputter Chamber

Shown in Figure 4-9, the PEEK substrates sit on a circular substrate stage of 6" diameter which rotates about the vertical axis during deposition. This ensures that each sample is exposed to the same sputter geometry, with respect to its distance and angle to the sputter source, for equal time duration.

After deposition was completed, the chamber was vented using  $N_2$  gas and the samples were allowed to cool naturally before removal. (Although heat is generated by the high energy of sputtered atoms associated with the plasma, samples were examined immediately after deposition and found to be heated to less than  $70^\circ C$ , well below the

glass transition temperature of the PEEK substrates). After removal from the vacuum chamber, the samples were placed in cell culture plates and stored in a dessicator.

#### **4.2.6. Post-deposition heat treatment of coatings**

##### **4.2.6.1. Laser annealing**

Laser annealing was conducted using both KrF and ArF pulsed excimer laser systems (Lambda-Physik). The KrF laser (248nm) was focused using a concave glass lens, resulting in a spot size of  $0.503\text{cm}^2$  at a distance of 2.1m from the sample. Energy was set to 100mJ; although laser energy varies with each pulse, the average energy per pulse was found to be 106 mJ. This equates to a laser fluence of approximately 211 mJ/cm<sup>2</sup>. Pulse duration was 25 ns. For KrF laser attempts, samples were exposed to 1, 2 and 3 pulses; further pulses were not attempted due to visible damage to the samples. (This will be discussed in Section 4.3).

ArF laser (193nm) treatment was conducted in a similar fashion. Spot size was focused down to  $0.11\text{cm}^2$  at a distance of 1.4m. Laser energy was inconsistent and energies above 2mJ were unattainable due to an unknown problem with the laser system. However, pulses of 1, 10, 100 and 1000 were attempted at 25 ns pulse duration using low laser fluence in the range of 10-18 mJ/cm<sup>2</sup>. After laser treatment, all samples were stored in a dessicator for further analysis.

#### 4.2.6.2. Hydrothermal annealing

Hydrothermal annealing treatment uses the aspects of moderately high temperature combined with elevated steam pressure to cause phase change in certain materials. While crystallization of HA coatings has been demonstrated at temperature/pressure combinations as low as 110°C/145kPa, it has been shown that higher pressure and temperature of the steam causes faster crystallization [61].

In this research, hydrothermal annealing was conducted using a large-scale autoclave (Steris Prevac Steam Sterilizer) with interior dimensions of 26"x37.5"x48" and capable of temperatures up to 141°C. The system is operated using deionized water to create the steam. Samples (5 samples per set) were autoclaved using saturated steam of 135°C, corresponding to a pressure of 313 kPa, at time periods of 2, 6, 12, 24, 48 and 72 hours. However, it should be noted that for time periods above 24 hours, the autoclave cycle was interrupted in between 24 hour periods for approximately 30 minutes, in order to prevent damage to door seals, as per manufacturer's recommendation. After hydrothermal treatment, samples were air-dried in ambient atmosphere and then stored in cell culture plates and kept in a desiccator until further analysis was performed.

#### **4.2.6.3. Microwave annealing**

Microwave annealing was done at using the facilities of an outside company. A parametric study was done to study of the effects of varying time, temperature, thermal mass and the use of a susceptor in order to identify the most effective conditions for heating the HA coating without causing significant heating of the PEEK substrate. Details of this system are patent-pending, and as such, have been omitted from this description. Results from XRD, SEM and optical microscopy (shown in Section 4.4), as well as visual observation, enabled the selection of an optimal set of parameters for microwave annealing.

### **4.3. Analysis techniques**

#### **4.3.1. Determination of deposition rate**

Before multiple samples were produced for further study and heat treatment, deposition rate was optimized as a function of RF power and target-to-substrate distance. In general, an increase in RF power results in a proportional increase in sputter rate; however, deposition rate does not necessarily follow sputter rate in all circumstances. For example, high RF power can result in a “re-sputtering” effect from the substrate surface, in which atoms depositing on the substrate surface are removed by the high energy of incoming atoms, lowering the effective deposition rate.

On the other hand, the target-to-substrate distance has a square relation with respect to deposition rate, within an appropriate range. As this distance is decreased,

the deposition rate increases by a square factor; for example, if the distance is halved, the deposition rate generally increases by a factor of 4. However, similar to RF power, if the distance is decreased past a certain distance, the deposition rate will begin to decrease as a result of re-sputtering. In this case, the re-sputtering is caused by the substrate coming into the range of the sputtering plasma.

In order to determine the optimal parameters of RF power and target-to-substrate distance, each value has been varied separately, and the resultant coating thickness has been measured at several time increments. Coating thickness was initially measured by creating a distinct step between uncoated and coated regions of the substrate surface using polyimide tape (Kapton) to mask one region of the sample surface. This step height was then measured by obtaining a surface profile across this step using a Veeco Dektak 150 surface profilometer, shown in Figure 4-10. Deposition rate is then calculated by dividing the total coating thickness (as estimated by step height) by the deposition time in hours, to arrive at a rate in terms of nm/hr. This process was done for HA and YSZ separately, using two sets of samples: one set coated with HA only, and one set coated with YSZ only.

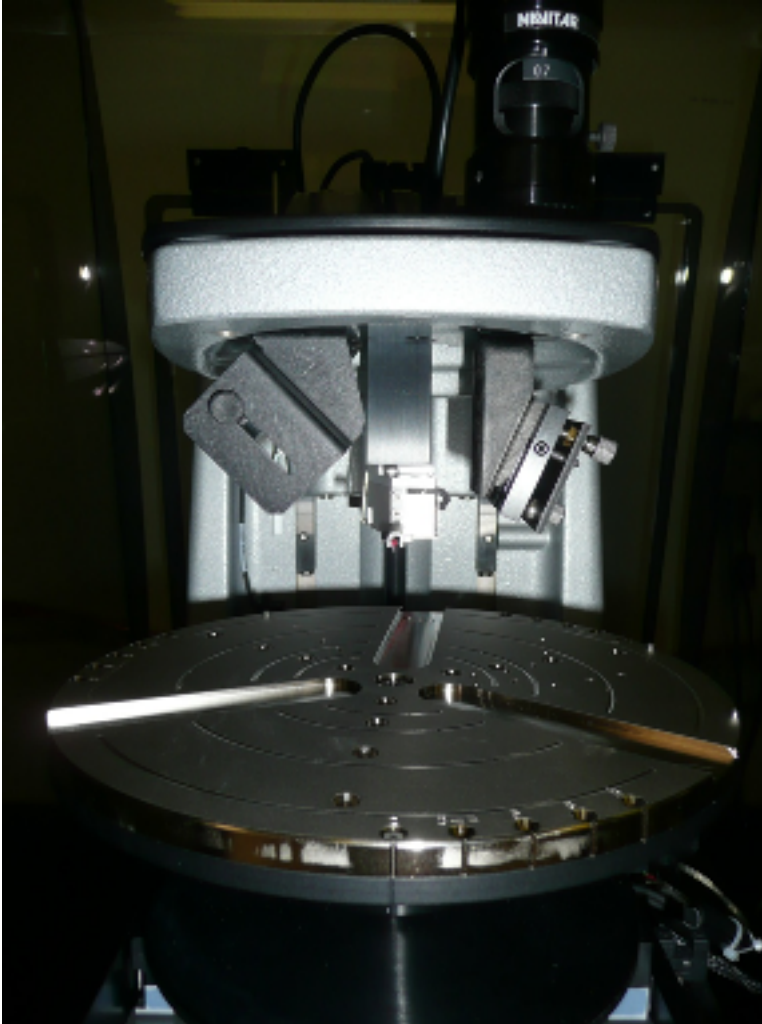


Figure 4-10. Surface Profilometer (Veeco Dektak 150)

Coating thickness was measured on PEEK substrates and on Si wafers (due to their extremely smooth and flat surface that allows accurate coating thickness measurements). Surface scans were performed at 3 adjacent points across each step, and coating thickness was taken as the average of the resulting step heights.

### 4.3.2. Coating adhesion strength

Coating adhesion strengths to the PEEK substrates were evaluated using a Romulus IV materials tester and the Romulus software automated program. Figure 4-11 shows the schematic representation of pull off test. Epoxy coated studs (Quad Group), with a cured adhesive strength of 70 ~ 100 MPa, were secured perpendicular to the coating surface with the stud mounting clips. The mounted samples were cured over 1 hour at 150°C in ambient atmosphere in a programmable oven (Fisher Scientific). Samples were then removed from furnace and allowed to air-cool to room temperature. The stud mounting clips were removed prior to test and each sample was then individually placed into the Romulus IV materials tester. A force controlled by Romulus software automated program was applied onto a stud in order to pull the stud off from coating surface and the adhesion strength was outputted as the required load for failure. The loading rate was set to 10 N/s and the maximum load that can be applied was 445 N. Both the pull off area of coating and stud head were then observed under an optical microscope. Failure modes were classified based on the percentages of one of the following three categories: epoxy failure, coating failure, or coating delamination.

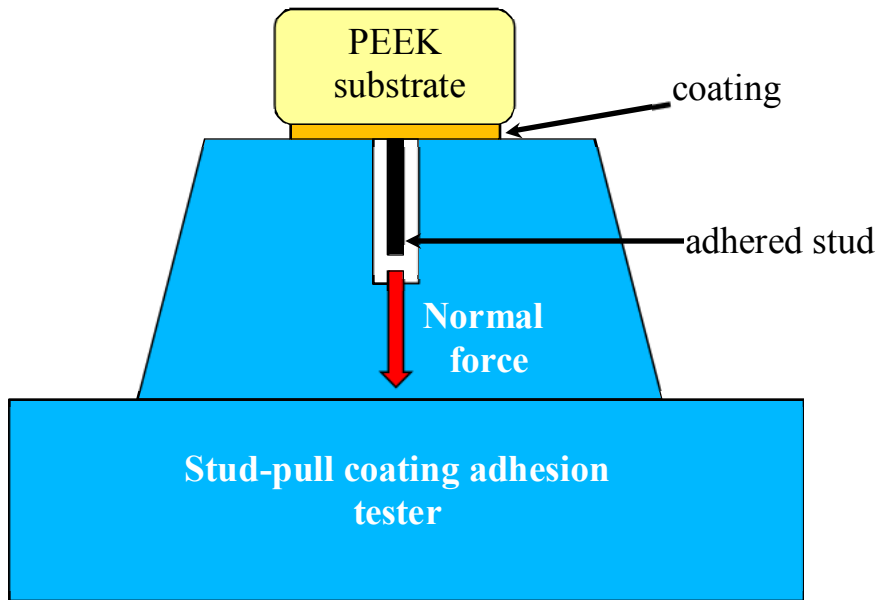


Figure 4-11. Schematic diagram of stud-pull coating adhesion tester.



Figure 4-12. Image of stud-pull coating adhesion tester.

### **4.3.3. Optical Microscopy**

Optical microscopy was performed using an XJP – H100 microscope with a digital camera (Amscope MU500, 5.1MP) attachment to capture digital micrographs. Areas of coating pull-off circles, formed during the stud-pull coating adhesion tests were observed in order to analyze the failure mechanism; from these areas, the amount of coating which was either delaminated, partially removed or fully remaining on the PEEK substrate surface after the stud-pull test was determined. Failure mechanism was then categorized based on these visual observations of pull-off areas.

Coating surfaces were also analyzed on undamaged regions of each coating type (as-deposited, microwave-annealed, laser-annealed, and hydrothermally annealed), in order to view differences between samples undergoing different post-deposition heat treatments and to search for evidence of crystallization or deterioration of the coating top surface.

### **4.3.4. X-ray diffraction**

Chemical composition, crystal structure and phases were analyzed using X-ray diffraction (XRD). XRD was performed on both untreated and heat treated coated samples, as well as on the HA target using a Rigaku Smartlab powder diffractometer at the Analytical Instrumentation Facility (AIF) of NCSU to verify the presence of crystalline HA. Coatings were analyzed using glancing angle mode with Cu K $\alpha$  ( $\lambda=0.1542$  nm) radiation at 40 kV and 20 milliamps. Samples were scanned between 25° and 60° 2 $\theta$  at a scan rate of 1 degree per

minute. Results were then compared to JCPDS powder diffraction standards using PDXL software to confirm the presence of crystalline HA or any other calcium phosphate compounds that might be present in the coating.

#### **4.3.5. Scanning Electron Microscopy**

Scanning electron microscopy (SEM) was used to observe the HA/YSZ coatings through the cross-section and at the coating/substrate interface. Coating porosity, homogeneity, presence of crystalline features, and the quality of the substrate/coating interface were determined by analyzing several areas of each. Cross-sectional samples were prepared by freezing thin samples of HA/YSZ-coated PEEK with liquid nitrogen (LN<sub>2</sub>) and then fracturing to produce a sharp break with a clear view of the coating from the substrate interface to the top coating surface. Magnifications were varied from 1000X to 50,000X in order to observe all microstructural characteristics from coating thickness uniformity to crystalline grain size.

#### **4.3.6. Scanning Electron Microscopy with energy dispersive X-ray (EDX)**

##### **Spectroscopy**

The surface composition of the coatings were evaluated using a scanning electron microscope (SEM, Hitachi S-3200N) equipped with energy dispersive X-ray spectroscopy (EDX) at AIF of NCSU. Areas from the outer edge to the center of the coating surface were selected and measured. Quantitative elemental composition was

then determined by averaging values from all measured areas; this was used to determine the Ca:P ratio of the hydroxyapatite coating.

#### **4.3.7. Fourier transform infrared spectroscopy**

A Nicolet Nexus 470 Fourier transform infrared spectrophotometer (FTIR) with a smart orbit diamond attenuated total reflectance (ATR) insert at the department of Textile Engineering of NCSU was used to evaluate the structural and molecular composition of the coatings and HA target in order to identify presence of chemical group OH<sup>-</sup> and PO<sub>4</sub><sup>3-</sup>. Each sample was scanned with a resolution of 2 cm<sup>-1</sup> with a scan number of 64.

#### **4.3.8. Cell Culture Tests**

Biological response to the samples of as-deposited and microwave-annealed coating groups was conducted by an outside collaborator (at the University of Texas at San Antonio) and compared with a control surface (uncoated PEEK) using a human fetal osteoblast cell line (bone-forming cells). The specific cell line is identified as CRL 1486 human embryonic palatal mesenchyme (HEPM) cells, which were obtained from a commercial supplier (ATCC). These cells were cultured in a growth medium of Eagle's Minimum Essential Medium (ATCC), with 10% fetal bovine serum and kept in a humidified CO<sub>2</sub> atmosphere at a temperature of 37.0°C. Two cell culture assays were performed using this cell line:

1. Initial cell attachment: samples (n=6) were seeded with human fetal osteoblast cells at 40,000 cells per square centimeter only on the top surface of each sample. Six hours after seeding, the media was removed and the number of unattached cells was counted using a cell culture counter.

2. Cell growth: samples (n=6) were again seeded with the osteoblast cells and cultured for periods of up to 3 days. At the end of days 1 and 3, cells were fixed on the sample surfaces using glutaldehyde and then stained with a QuantiFlour fluorescent dye (Promega). Double-stranded DNA (dsDNA) content was quantified by visual observation of the cell surfaces using fluorescent microscopy. DNA content is related to the growth of healthy cells present.

#### **4.4. Results**

##### **4.4.1. Deposition Rate**

Deposition rate was evaluated over a three target-to-substrate distances and at three different power levels in order to reduce deposition time and allow for coatings to be produced in the least number of steps (access to the RF magnetron sputter system is only available during the normal operating hours of the NNF cleanroom facility for safety reasons). In determining the deposition rate, only the HA target was used; the effect of target-to-substrate distance and RF power on sputtering is assumed to be the same with the YSZ target.

As expected, HA coating thickness at each time point was found to be highest at the highest power level used of 150 Watts, shown in Figure 4-13. It is assumed that this trend would continue; increasing power should result in even higher deposition rate. However, power was limited to 150 W, as recommended by the sputter target manufacturer (Kurt J. Lesker Co.) in order to avoid overheating the target, possibly resulting in cracking of the brittle HA ceramic, as the copper backing plate to which it is bonded expands at a higher rate due to their different thermal expansion coefficients.

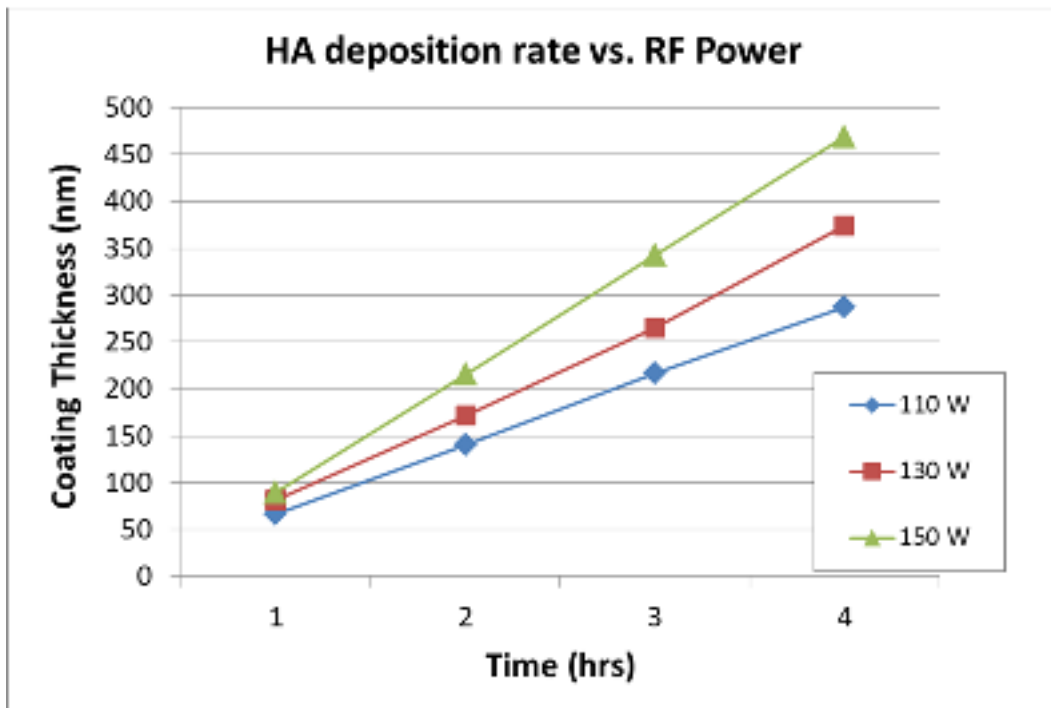


Figure 4-13. HA deposition rate vs. RF Power

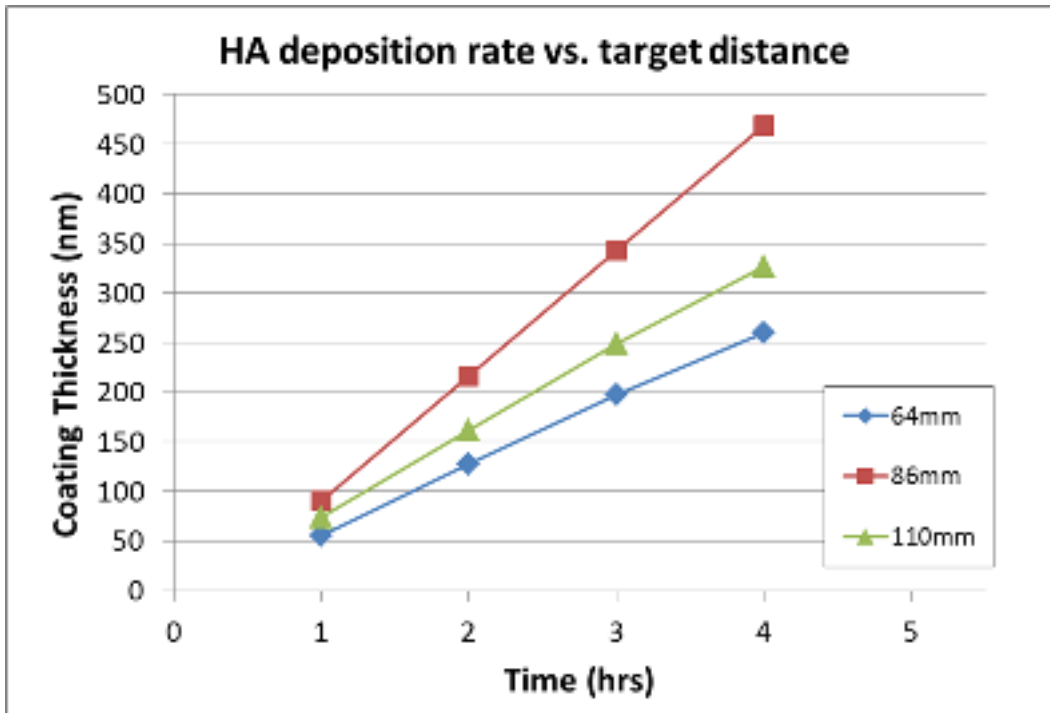


Figure 4-14. HA deposition rate vs. Time

Power density was recommended not to exceed 20-25 Watts/in<sup>2</sup> of the target surface to avoid these risks; as such, maximum power supplied to the HA target (3" diameter) was 150 Watts, and the maximum power used for the YSZ target (2" diameter) was 80 Watts.

Using an RF power of 150 W, target-to-substrate distance was then optimized in a similar manner, choosing three distances, equally spaced, which were thought to be within the appropriate range of high density of sputtered atoms without being so close as to be significantly heated by the sputter target. Figure 4-14 shows the HA coating thickness after time periods up to 4 hours, in one hour increments, at target-to-

substrate distances of 64, 86 and 110mm. It was found that a distance of 86mm resulted in the highest deposition rate (117nm/hr).

Using the optimized target-to-substrate distance of 86mm and using maximum recommended RF power settings for YSZ and HA (80W and 150W, respectively), both YSZ and HA coatings were deposited up to 10 hours and 12 hours, respectively. This was done in order to ensure that deposition rate remained consistent over longer time periods, as sputter deposition processes can reach a maximum coating thickness, after which addition deposition time does not result in a significant increase in coating thickness. As seen in Figure 4-15, this saturation in deposition rate was not encountered within the range of deposition times studied in this research. Table 4-2 lists average deposition rates for YSZ and HA; both materials remained consistent over deposition periods of 10 and 12 hours, respectively, with the deposition rate changing less than 5% over any interval.

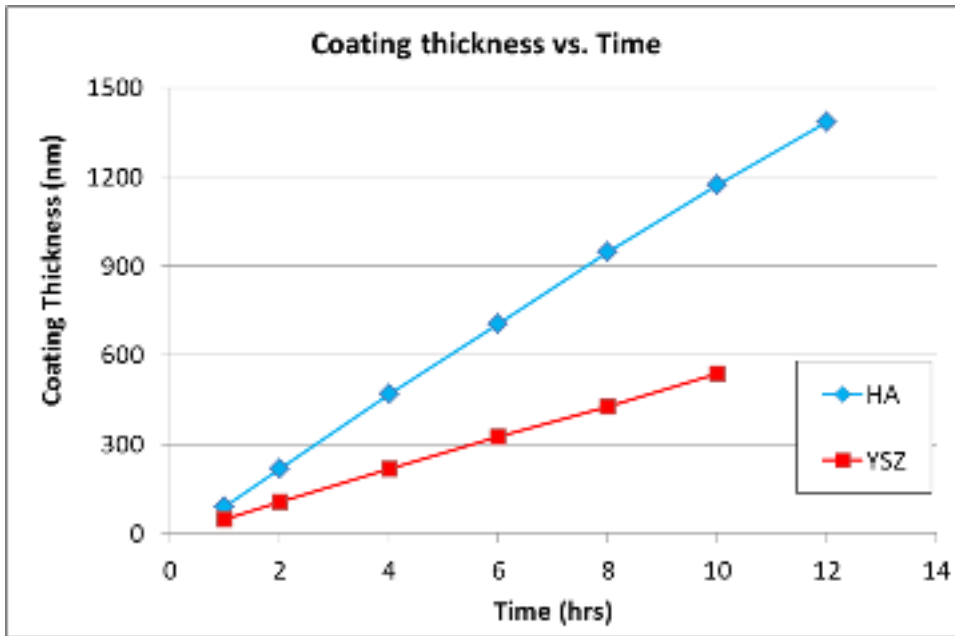


Figure 4-15. Coating thickness vs. time for YSZ and HA targets

Table 4-2. Deposition rates for YSZ and HA coatings

Deposition Time (hrs)	YSZ coating		HA coating	
	Total Coating Thickness (nm)	Average Deposition Rate (nm/hr)	Total Coating Thickness (nm)	Average Deposition Rate (nm/hr)
1	46	46	90	90
2	107	53.5	216	108
4	216	54	469	117.3
6	324	54	705	117.5
8	428	53.5	947	118.4
10	539	53.9	1172	117.2
12			1354	115.5

#### 4.4.2. Physical and Mechanical Properties

Once deposition rate was established, the coating adhesion to the PEEK substrates was measured as a function of surface preparation by the varying roughness of the SiC grinding paper and the alumina particle size of the polishing paste, shown in Table 4-3.

Table 4-3. Coating adhesion strength on PEEK substrates of varied surface roughness

PEEK Surface Preparation	Coating Adhesion Strength (MPa)
600-grit SiC paper	15.1
800-grit SiC paper	13.4
1200-grit SiC paper	11.3
9 $\mu\text{m}$ $\text{Al}_2\text{O}_3$ paste	11.9
6 $\mu\text{m}$ $\text{Al}_2\text{O}_3$ paste	9.1
Sub-micron $\mu\text{m}$ $\text{Al}_2\text{O}_3$ paste	6.0

For imaging purposes, PEEK surfaces were polished to 800-grit SiC paper. This produces a surface that is sufficiently flat for subsequent observation by cross-sectional SEM.

In order to further improve the coating adhesion, pre-treatment of the PEEK substrates by reaction with  $\text{O}_2$  plasma was employed. As previously described, this has shown to increase surface energy and wettability of polymer surfaces, ultimately

leading to better coating adhesion. This effect is shown in Table 4-4; coating adhesion strength, measured using the stud-pull coating adhesion tester, was improved from 0 to 10 minutes. After 10 minutes, adhesion strength did not exhibit any significant improvement or deterioration.

Table 4-4. Effect of plasma treatment on coating adhesion strength

<b>O<sub>2</sub> Plasma pre-treatment time</b>	<b>Adhesion Strength (MPa)</b>
1 min	6.65 +/- 1.34
3 min	16.23 +/- 5.09
5 min	19.73 +/- 2.34
10 min	31.63 +/- 8.79
15 min	28.24 +/- 7.38
20 min	33.31 +/- 5.32
25 min	31.34 +/- 6.02

This trend is also seen graphically in Figure 4-16.

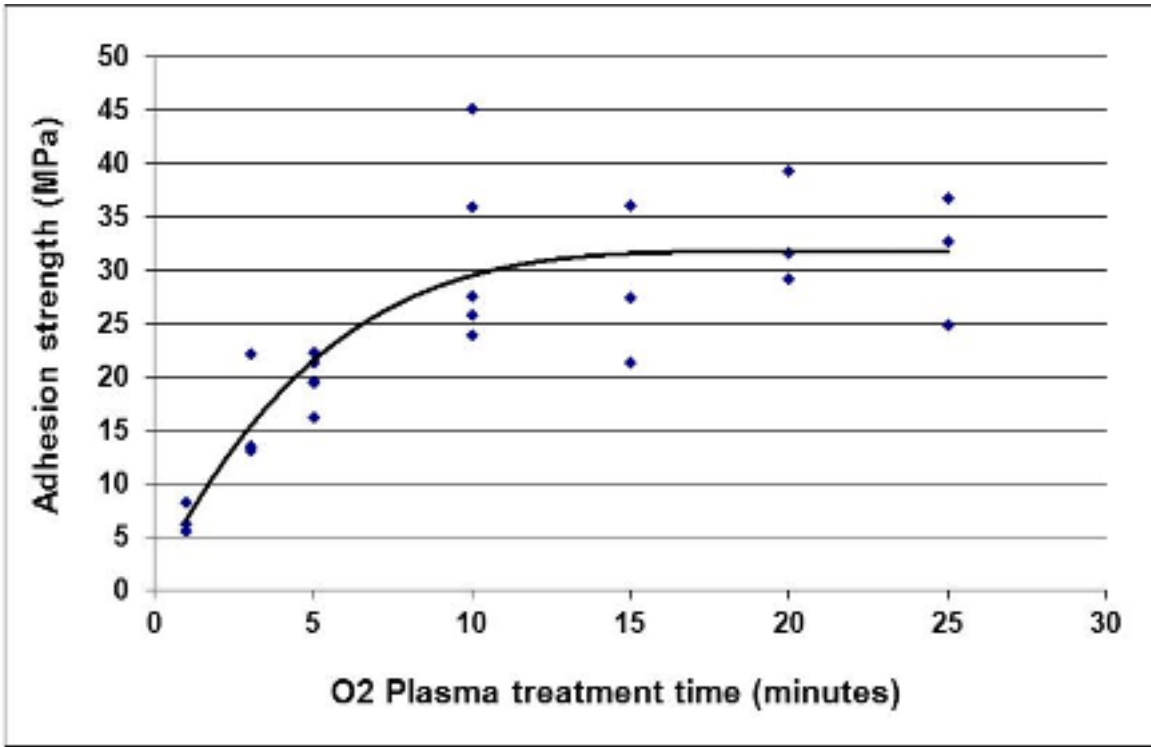


Figure 4-16. Plot of plasma treatment time versus coating adhesion strength

Coating adhesion strength was again measured after each of the post-deposition heat treatment methods in order to determine whether any degradation at the coating-substrate interface had occurred. Several samples (at least 5) of each set were tested. Results are shown in Table 4-5.

Table 4-5. Coating Adhesion strength before and after heat-treatment methods

Heat Treatment Method	Average Coating Adhesion Strength (MPa)
Untreated	33.4
ArF pulsed laser	33.1
KrF pulsed laser	7.7
Hydrothermal anneal	30.9
Microwave anneal	32.5

It was demonstrated that only the KrF laser-annealed samples had significantly lower coating adhesion strength, suggesting that ArF laser annealing, hydrothermal annealing and microwave annealing methods had no adverse effect on the substrate/coating interface.

#### 4.4.3. Optical Microscopy

Optical microscopy was performed for two reasons: 1) To analyze the failure mechanism encountered during stud-pull coating adhesion tests; 2) To observe the physical appearance of the coating top surface at magnifications from 10X to 100X for evidence of any crystalline features (visible grain boundaries, etc.) or damage to the coating.

#### **4.4.3.1. Coating pull-off area from stud-pull adhesion tests**

Coating pull-off areas, resulting from the stud-pull coating adhesion tests, were analyzed in order to characterize the failure mechanism of the coatings. Failure mechanism can be categorized based on the percentages of: 1) Coating delamination; the coating is completely removed from the PEEK substrate by the normal force exerted by the stud-pull 2) Cohesive failure; the fracture occurs within the coating, and the coating is partially removed by the stud, while partially remaining adhered to the substrate (this indicates a weak cohesive strength within the coating itself) 3) Epoxy failure; the coating remains completely intact to the substrate and the de-bonding occurs at the epoxy/coating interface or the epoxy/stud interface (in this case, epoxy failure is either a result of the coating adhesion strength being higher than the epoxy adhesion strength (above 85 MPa), or the epoxy fails at low strength due to improper curing of the epoxy stud to the sample surface; the latter type of failure is not a measure of the coating adhesion strength and is removed from the average to eliminate any invalid data). Examples of each of these failure mechanisms can be seen in the optical micrographs to follow. Figure 4-17 shows a coating pull-off area in which the coating was completely removed from the PEEK substrate. In this case, the coating cohesive strength (within the coating itself) is stronger than the adhesive strength at the coating/substrate interface. Also, the coating adhesion strength calculated by stud-pull tester is accurate for failures of this type, as the adhered area of the stud represents the area of coating removed by the applied force.

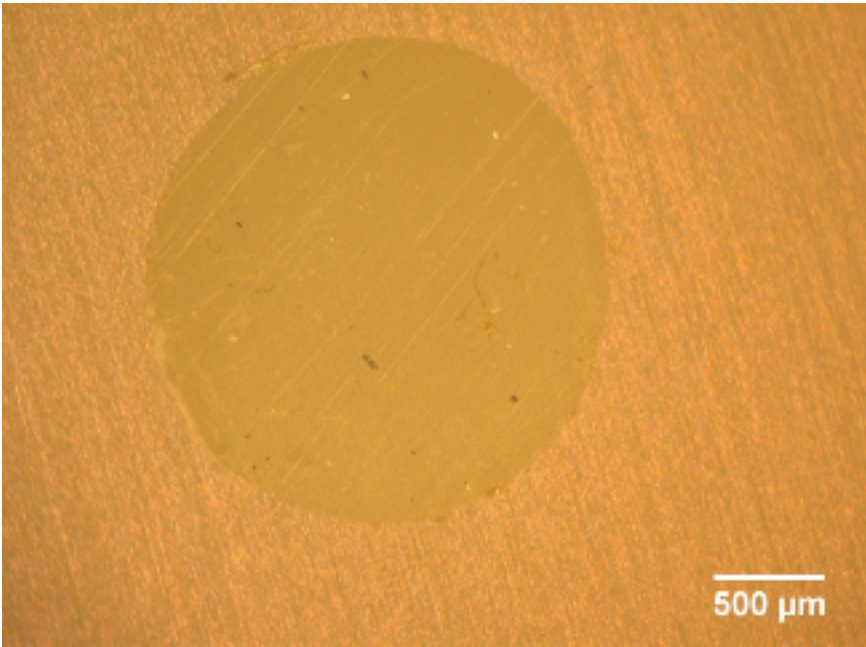


Figure 4-17. Coating pull-off area for fully delaminated coating

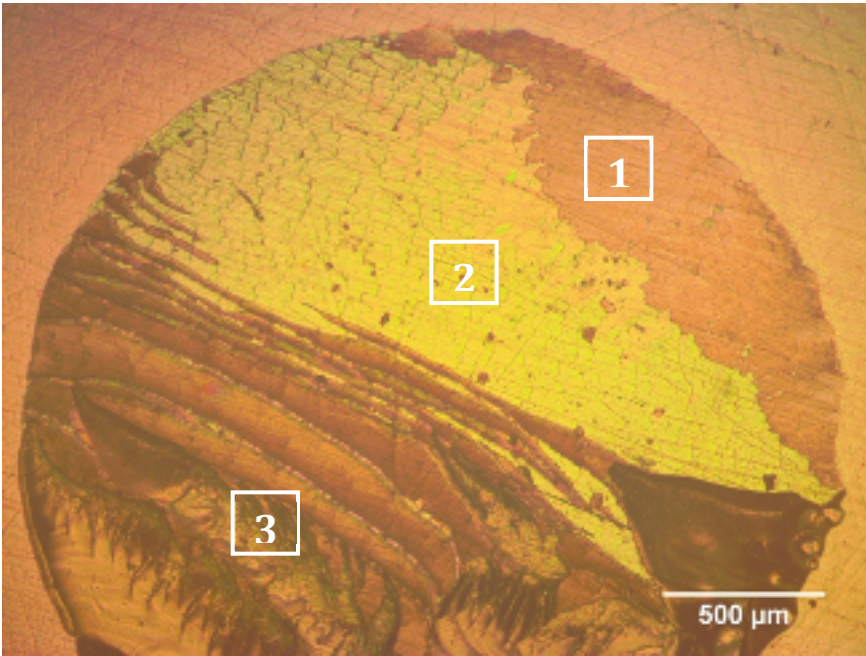


Figure 4-18. Coating pull-off area for partially delaminated coating

Figure 4-18 shows a coating pull-off area in which the failure mechanism is a combination of coating delamination and cohesive failure. Within the circular area of the coating surface to which the stud was initially adhered, three distinct regions can be seen, corresponding to different failure mechanisms; area 1) epoxy failure – the coating remains fully adhered (the epoxy from the stud has transferred to the coating surface, resulting in a slightly darker appearance); area 2) cohesive failure – the coating is partially removed, failing within coating itself; area 3) mixed region – the coating is fully removed in some areas, while exhibits cohesive failure in others (this is apparent from the 3-dimensional appearance in this region).

A summary of the average failure types observed among the various coating sample groups is listed in Table 4-6. Abbreviations are used to indicate failure type (CD = coating delamination, CF = cohesive failure).

Table 4-6. Summary of Coating Adhesion Tests

<b>Heat Treatment Method</b>	<b>Average Coating Adhesion Strength (MPa)</b>	<b>Coating Failure Type</b>
Untreated	33.4	92% CD, 8% CF
ArF pulsed laser	33.1	90% CD, 10% CF
KrF pulsed laser	7.7	44% CD, 56% CF
Hydrothermal anneal	30.9	78% CD, 22% CF
Microwave anneal	32.5	86% CD, 14% CF

#### 4.4.3.2. Coating top surface

In addition to coating pull-off areas, several areas of the top coating surface of each sample type were observed using optical microscopy. Figure 4-19 shows the as-deposited coating top surface. Microwave-annealed and KrF laser-annealed coating top surfaces are shown in Figure 4-20 through 4-23. (Optical images of coating top surface are now shown for hydrothermal-annealed and ArF laser-annealed samples, as they are identical in appearance to the as-deposited coating surface, shown in Figure 4-19).

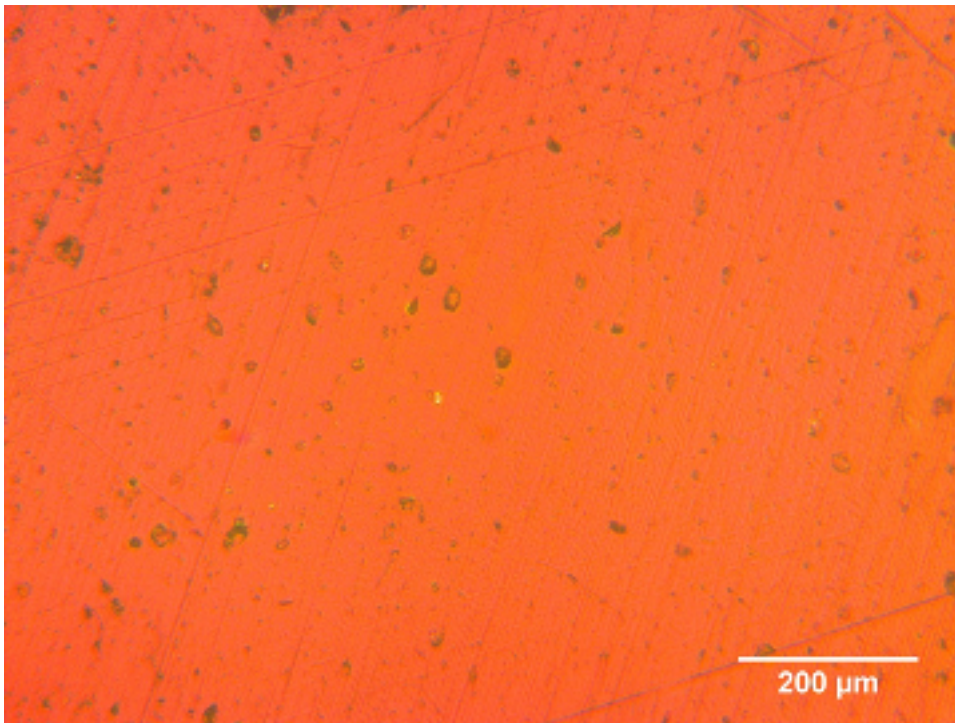


Figure 4-19. Optical micrograph of as-deposited coating top surface

Seen in Figure 4-19, the as-deposited coating surface contains small porosities and appears to have no distinct features. The coating appears uniform throughout the

viewing area, in terms of porosity and in its reflected color; because of the semi-transparency of many types of thin films, coated samples will reflect different wavelengths of light depending on their thickness. This coating appears to have an orange to rose color, which corresponds to a coating thickness of approximately 1100-1200 nm, for films of this type. While this is not a reliable method of determining coating thickness (due to effects such as wavelength of light used, color of underlying substrate and phase composition), it does suggest that the coating thickness is uniform across the sample.

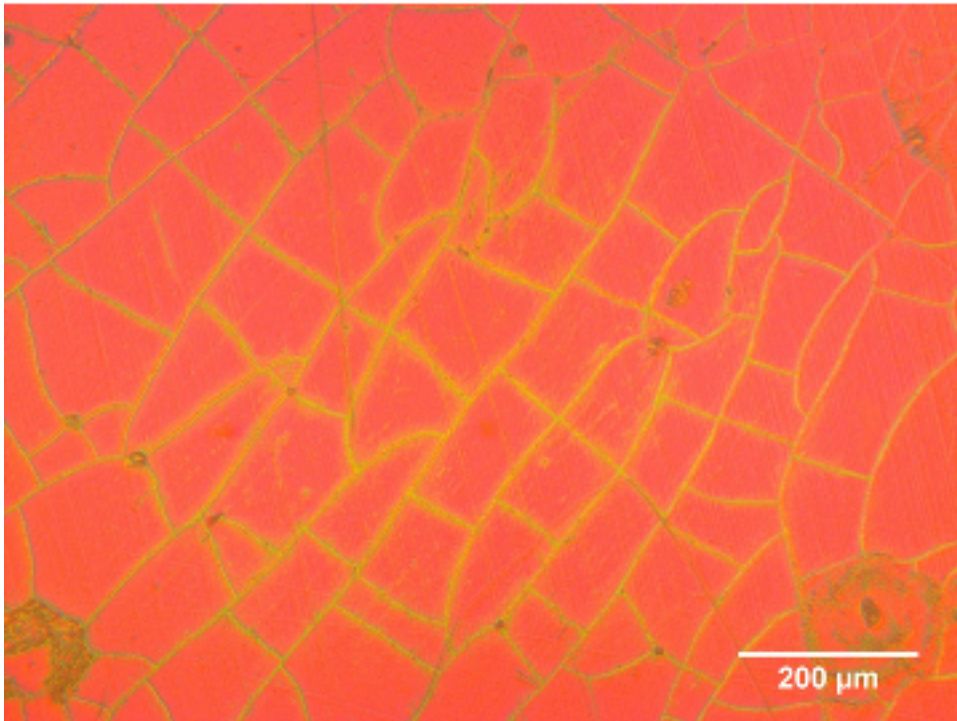


Figure 4-20. Optical micrograph of microwave-annealed coating top surface

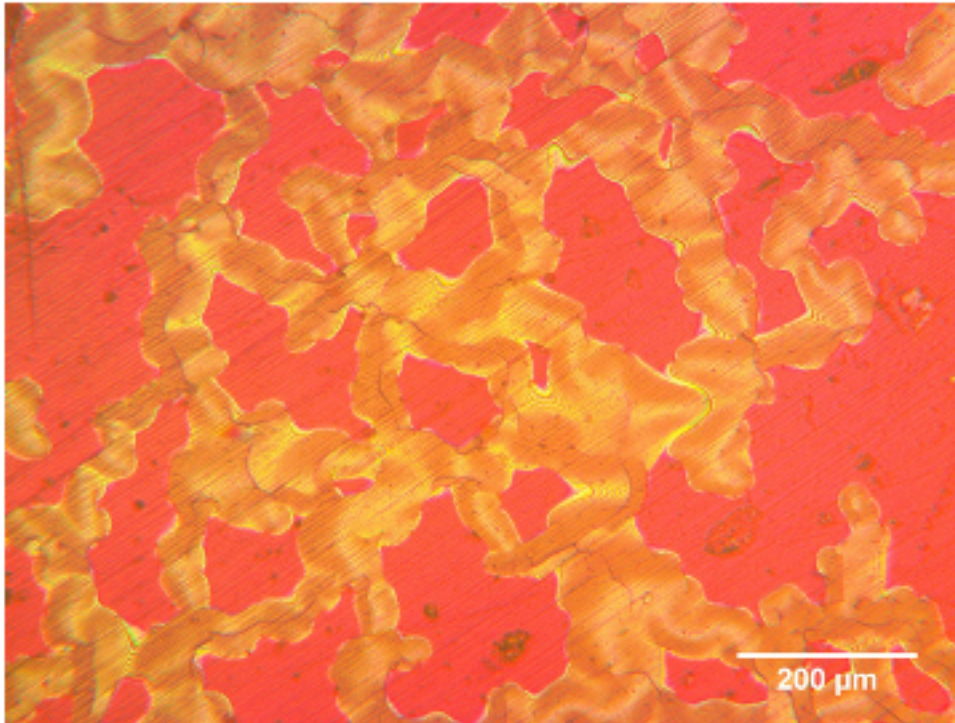


Figure 4-21. Optical micrograph of coating removal caused by microwave annealing

Figures 4-20 and 4-21 display coating top surfaces of samples undergoing microwave annealing. In Figure 4-20, the coating is observed to have separated into “islands” of dimensions between 100 and 300  $\mu\text{m}$ , possibly due to densification of the coating. In Figure 4-21, this effect has progressed even further and the bare PEEK substrate is now highly exposed due to large uncoated regions. These samples are selected from the microwave-annealed coatings before optimization of the microwave parameters and exhibited weak coating adhesion strength. The exact cause of the coating deterioration seen on these samples is not known, but is suspected to arise from excessive power and time applied during the microwave treatment.

Similarly, Figure 4-22 shows the coating surface of a sample after KrF laser annealing. The coating removal is clearly observed and area of laser incidence on the sample can be seen. Due to the visually observed damage of the coatings exposed to KrF laser annealing, this heat treatment method was deemed unsuccessful. Further analysis of this sample set was discontinued.

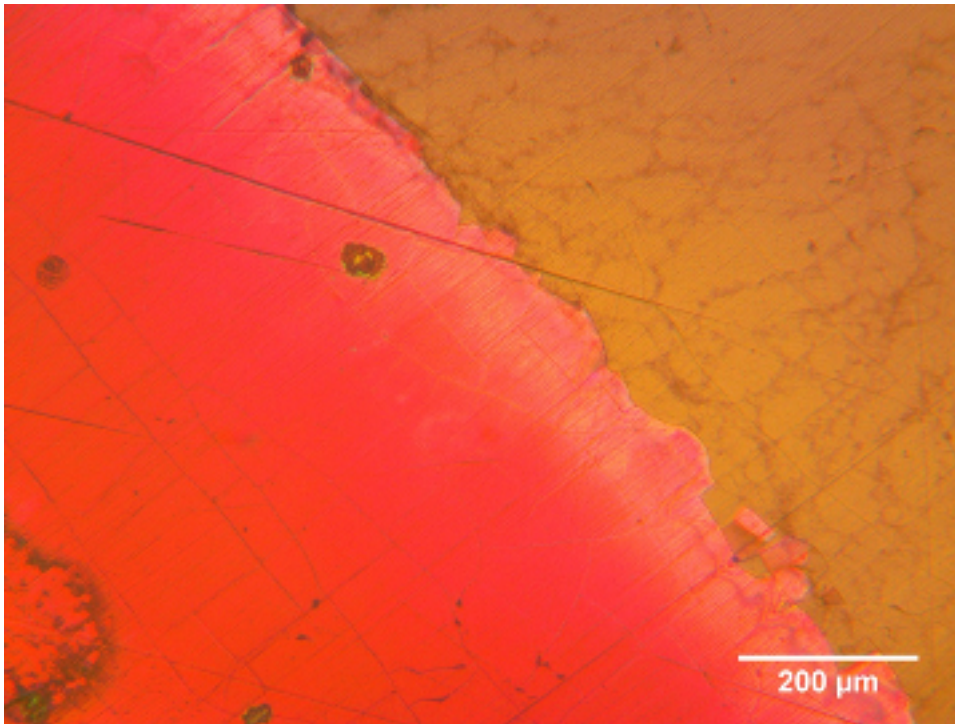


Figure 4-22. Optical image of coating ablation by KrF laser

Finally, Figure 4-23 shows the coating top surface of a sample after optimized microwave treatment. Compared with optical images of as-deposited coating surfaces (Figure 4-19), which displays no obvious features other than porosity, this coating

surface is seen to have distinct regions, comprising a “mosaic-like” structure, without exposing the PEEK substrate. It is suggested that this change is due to the formation of a crystal structure and grain boundaries in the HA layer.

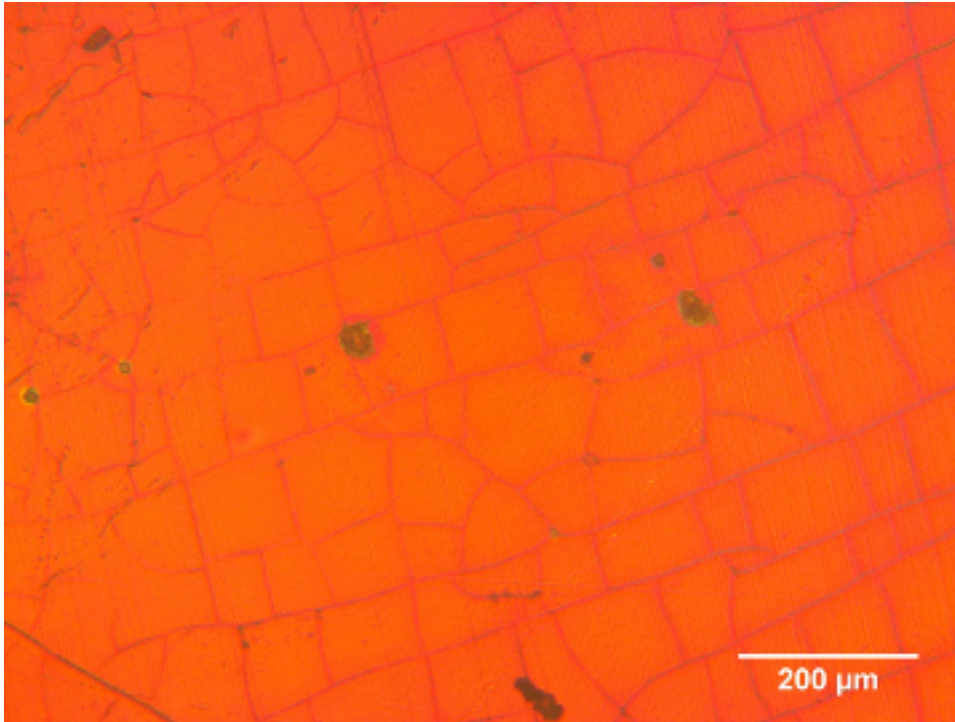


Figure 4-23. Optical image of top coating surface after microwave anneal

In all of the optical images displayed, the color of the coatings remained constant, suggesting that the coating thickness remained unchanged during these treatments.

#### 4.4.3. Microstructural Observation

Observation of the YSZ/HA coating cross-section and coating interface was accomplished using SEM. Digital micrographs of the HA/YSZ coating as-deposited and after post-deposition heat treatments are shown in the following images.

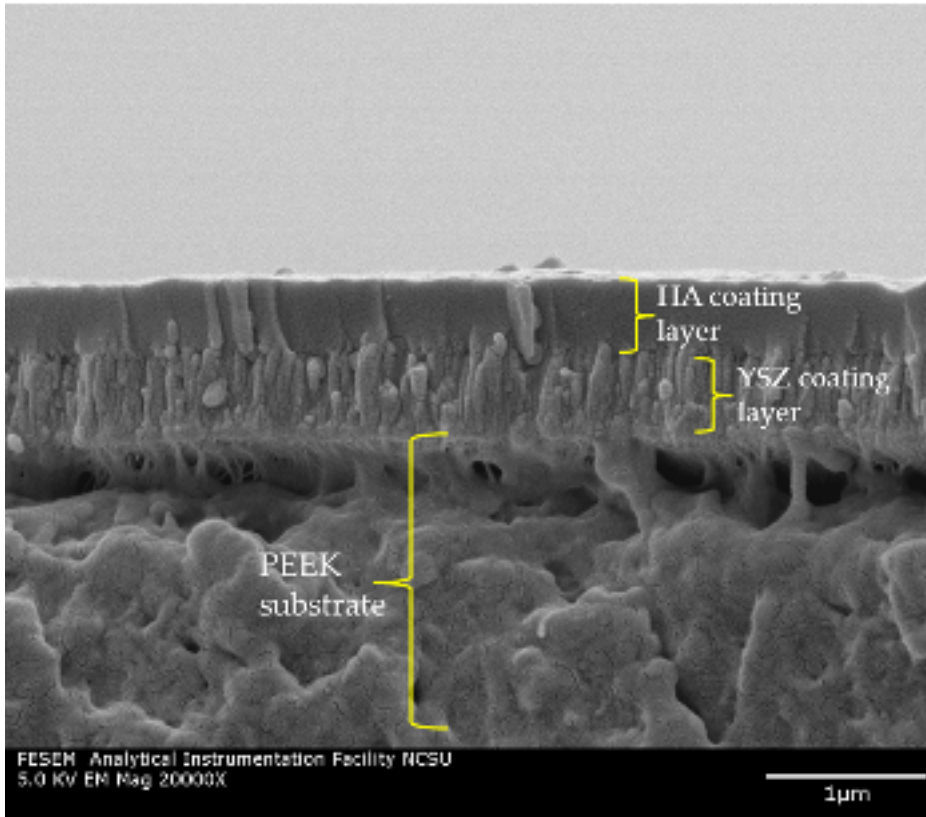


Figure 4-24. SEM Image of as-deposited YSZ/HA coating and PEEK substrate

Shown in Figure 4-24, the as-deposited YSZ/HA coating has a total coating thickness of approximately 1.1 to 1.2  $\mu\text{m}$ , which is uniform through the viewed area, and contains very low porosity through the coating thickness. YSZ and HA layers are easily

distinguished by their different microstructural features; the YSZ layer is composed mostly of a columnar crystal structure with growth direction normal to the substrate surface and crystals of 50-100nm in diameter, while the HA layer does not exhibit any clear crystalline features. Examination of the PEEK substrate/YSZ coating interface reveals a dense layer of small isotropic YSZ grains of diameter 30-60nm within the first 100nm of the coating, without any visible voids or porosity. On top of the interfacial layer of spherical YSZ grains, equiaxed columnar YSZ grains of diameter 30-100nm and length 200-400nm oriented perpendicular to the interface. The YSZ/HA interface is shown to have minimal porosity, as the HA layer deposited directly on top of the YSZ layer fills in voids between the existing YSZ grains. The HA layer is homogeneous in terms of thickness and lack of crystalline features, and is shown to have little or no porosity.

A higher magnification SEM micrograph, shown in Figure 4-25, facilitates measurement of the two coating layers, with the use of Revolution analytical software (4 Pi Analysis, Inc.). The measured YSZ and HA coatings exhibit thicknesses of 486nm and 731nm, respectively. It should also be noted that the interfacial void between the YSZ coating and the PEEK substrate is an artifact of the SEM sample preparation method, in which the sample was frozen in LN<sub>2</sub>, and then broken by bending. Due to the flexibility of PEEK, even at very low temperatures, the PEEK substrate was able to bend significantly before breaking, whereas the YSZ/HA coating was not able to

accommodate this flexion and consequently delaminated from the PEEK substrate in the process.

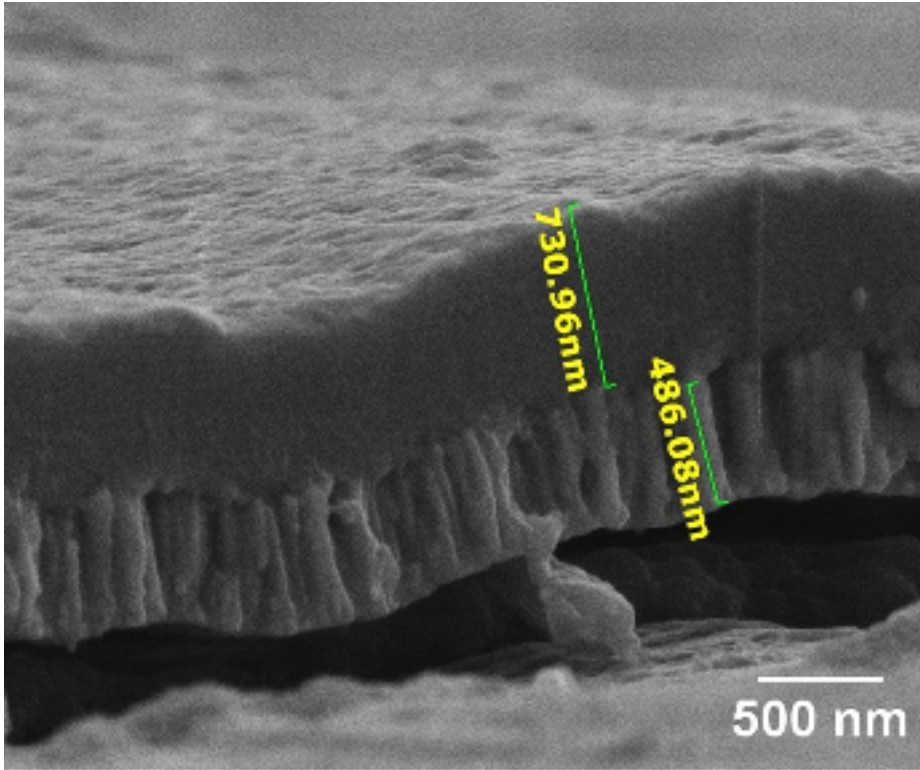


Figure 4-25. SEM Image of as-deposited YSZ/HA coating cross-section

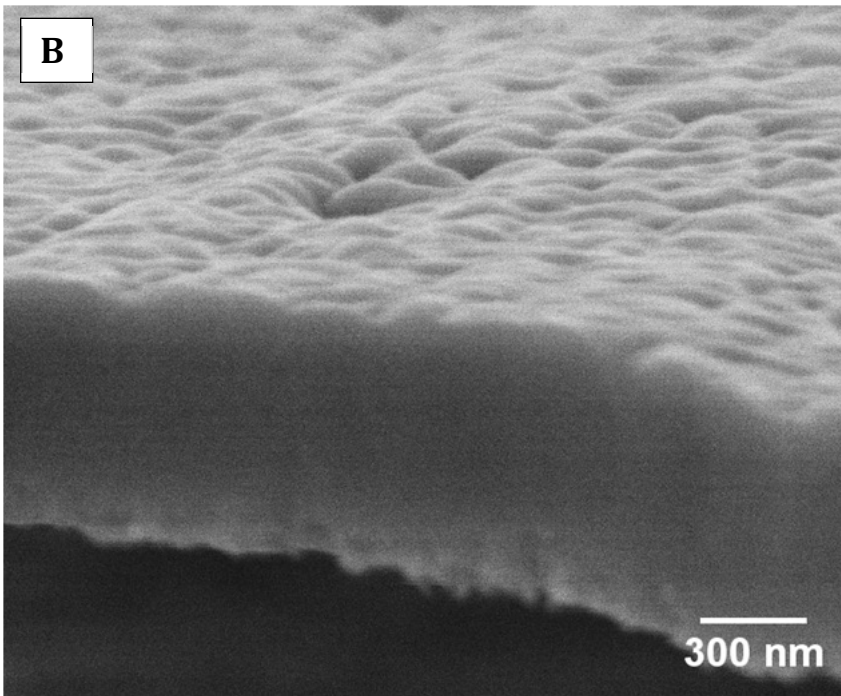
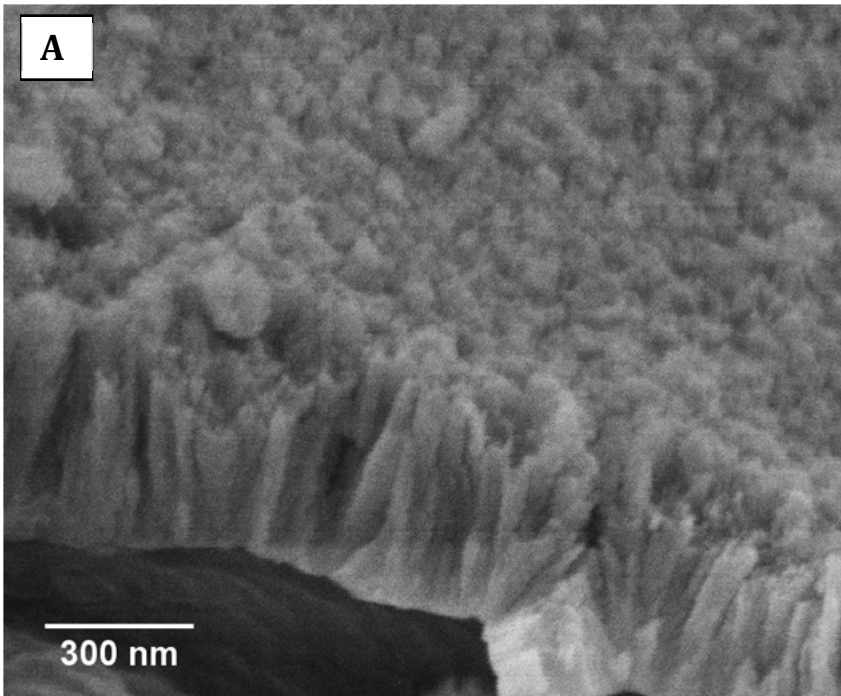


Figure 4-26. SEM images of A) YSZ and B) HA coatings separately

As seen in Figure 4-26a, the YSZ coating top surface exhibits a high surface roughness due to the columnar grain structure forming many local peaks and voids, while the HA coating (Figure 4-26b), exhibits a smoother surface owing to its lack of features. It is observed that the as-deposited YSZ coating layer is crystalline, while the HA coating layer is observed to be amorphous or nanocrystalline.

Shown in Figure Figure 4-27, the YSZ/HA coating after undergoing hydrothermal treatment for 48 hours appears unchanged compared with the as-deposited sample, with the exception of a small region of possibly developing columnar HA crystals, at the YSZ/HA interface (circled in red). It is not clear whether this crystallization is the result of hydrothermal treatment, as this feature was not consistently seen in the microstructures of all hydrothermally-treated samples.

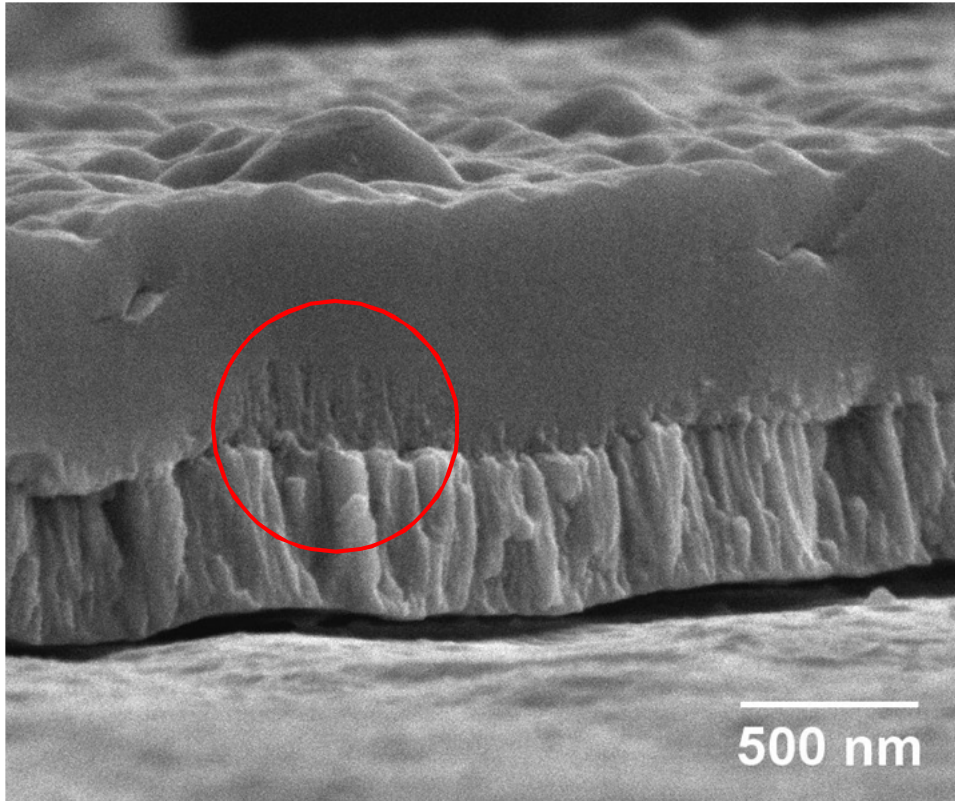


Figure 4-27. SEM image of HA/YSZ coating cross section after hydrothermal treatment

Finally, SEM images of microwave-annealed YSZ/HA coating cross section are shown in Figures 4-28 and 4-29.

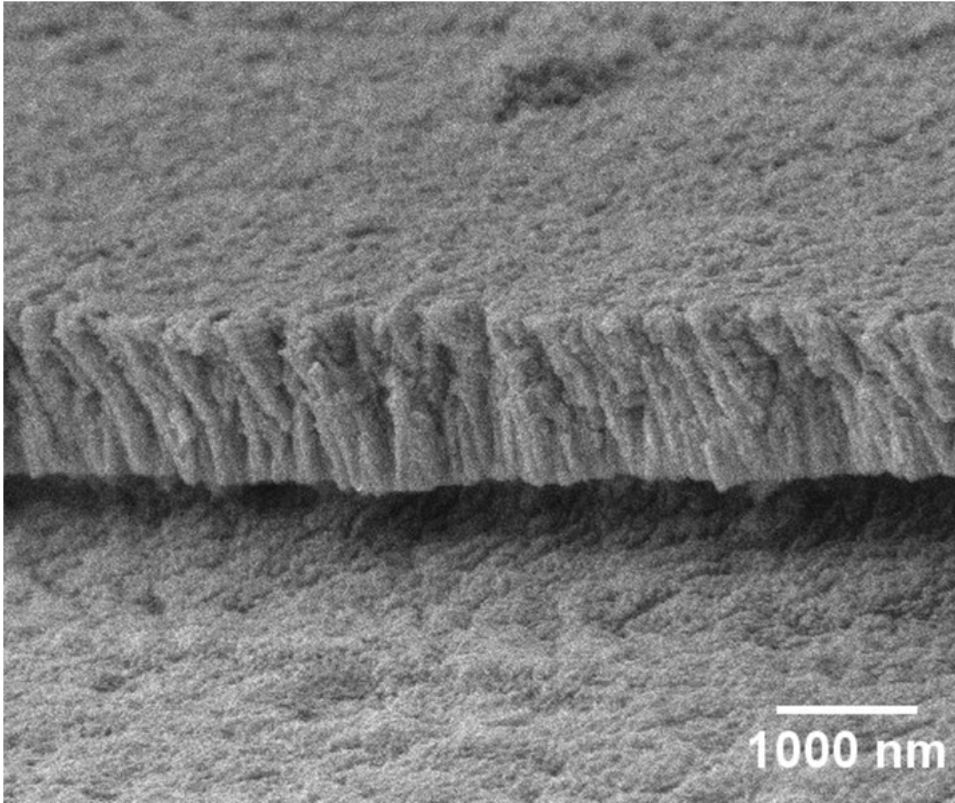


Figure 4-28. SEM image of HA/YSZ coating cross section after microwave annealing

From Figure 4-28, a significant change in the microstructure of HA coating layer is seen after microwave annealing; the HA coating now exhibits columnar features similar to those observed in the YSZ coating layer; this is assumed to be due to the formation of a crystalline structure as a result of the microwave heating. The YSZ coating layer has no visual changes as compared with this layer in the as-deposited samples. HA columnar grains exhibit similar orientation to the underlying YSZ columnar grains, with similar diameter and shape. The YSZ/HA coating thickness remains unchanged at

approximately 1.2 $\mu\text{m}$ , as displayed in a higher magnification image, shown in Figure 4-29.

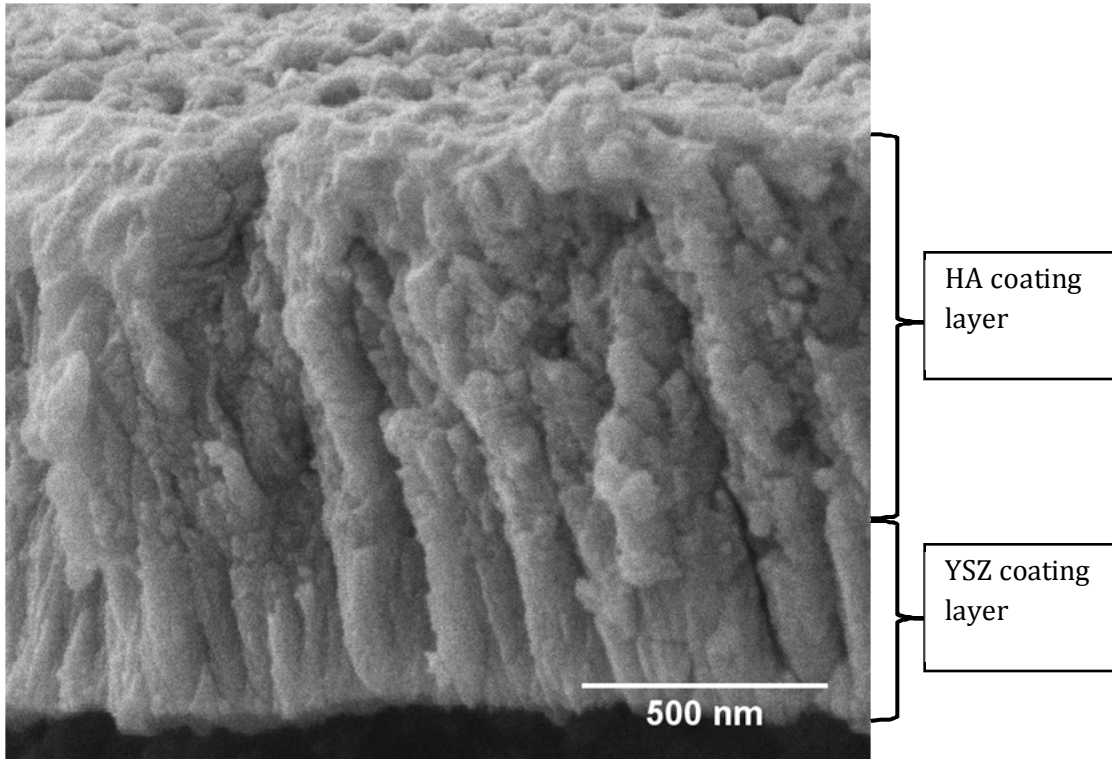


Figure 4-29. High magnification SEM image of microwave-annealed YSZ/HA coating cross-section

As displayed in Figure 4-29, the YSZ and HA coating layers appear to be well adhered to each other; HA crystals appear to form directly at the top grain boundaries of YSZ crystals. While the YSZ coating layer appears to consist primarily of long, equiaxed columnar grains, the HA coating layer appears to contain a combination of columnar-shaped grains as well as some more spherical or cubic-shaped grains.

#### **4.4.5. Compositional Analysis**

X-ray diffraction spectra from 25 to 60 degrees are displayed in the following graphs. For each sample, peaks are labeled by a number, with the exception of peaks corresponding to the PEEK substrate, which are labeled as “P”. The numbered peaks, corresponding to crystalline phases in the YSZ/HA coatings, are then identified and compared to JCPDS standards in a table following each spectrum.

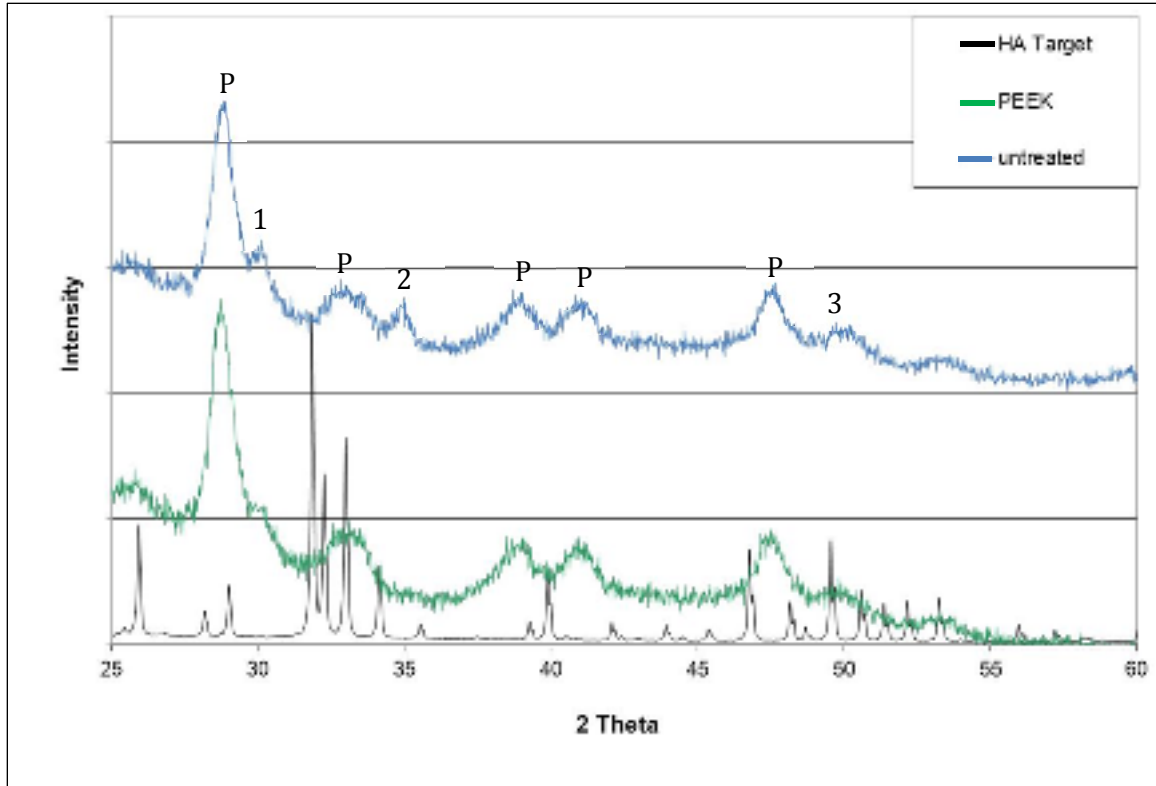


Figure 4-30. XRD Spectrum of as-deposited YSZ/HA coating on PEEK substrate

Table 4-7. Crystalline peaks identified in as-deposited YSZ/HA coating

Peak number	Measured $2\theta$ (degrees)	Theoretical $2\theta$ (degrees)	Phase / Material	(hkl)
1	29.82	30.14	YSZ	101
2	34.82	34.98	YSZ	110
3	49.6	50.23	YSZ	112

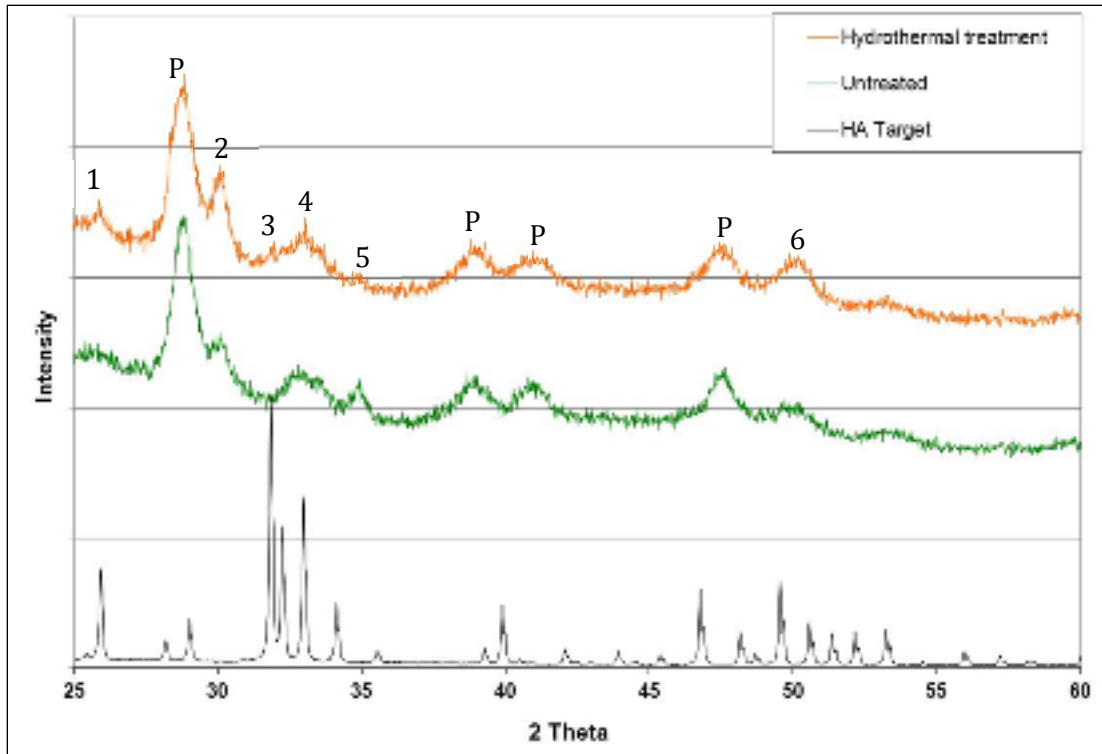


Figure 4-31. XRD Spectrum of 48-hour hydrothermally-annealed YSZ/HA coating

Table 4-8. Crystalline peaks identified in hydrothermally-annealed YSZ/HA coating

Peak number	Measured $2\theta$ (degrees)	Theoretical $2\theta$ (degrees)	Phase / Material	(hkl)
1	25.82	25.88	HA	002
2	29.96	30.14	YSZ	101
3	31.76	31.74	HA	211
4	33.0	32.87	HA	300
5	34.66	34.98	YSZ	110
6	49.98	50.23	YSZ	112

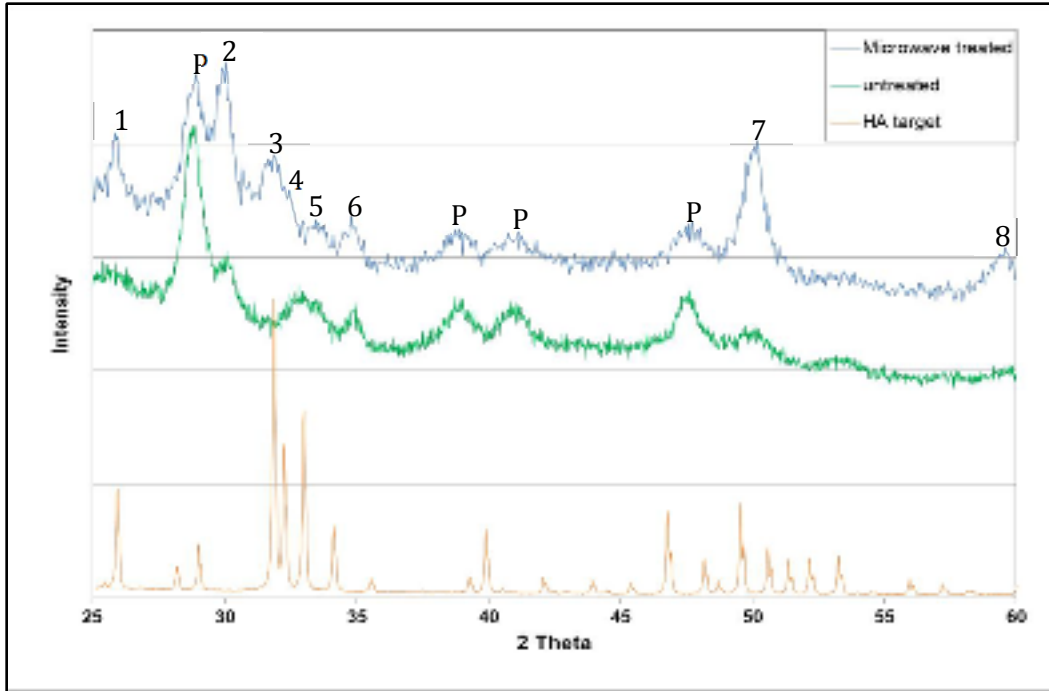


Figure 4-32. XRD Spectra of HA/YSZ coating after microwave annealing

Table 4-9. Crystalline peaks identified in microwave-annealed YSZ/HA coating

Peak number	Measured $2\theta$ (degrees)	Theoretical $2\theta$ (degrees)	Phase / Material	(hkl)
1	25.8	25.88	HA	002
2	29.85	30.14	YSZ	101
3	31.65	31.74	HA	211
4	32.3	32.18	HA	112
5	33.2	32.87	HA	300
6	34.8	34.98	YSZ	110
7	49.9	50.23	YSZ	112
8	59.35	59.76	YSZ	211

From Figure 4-30 and Table 4-7, the as-deposited YSZ/HA coating does not produce any strong reflections corresponding to crystalline HA. YSZ reflections of (101), (110) and (112) are present, but exhibit low intensity and the peaks are rather broad. These data suggest that the HA coating is either amorphous or contains a nanocrystalline structure. The YSZ coating layer is most likely partially crystalline, with some percentage of amorphous phase or nanocrystalline structure contributing to peak broadening.

XRD data of the hydrothermally-annealed YSZ/HA coating are shown in Figure 4-31 and Table 4-8. HA peaks corresponding to (002), (211) and (300) crystallographic planes are slightly distinguishable above the background spectrum, and correspond very closely to theoretical  $2\theta$  values for these reflections; it is possible that the HA coating layer of this sample contains a small increase in crystallinity percentage as compared with the untreated sample, or that the nanocrystalline HA grains have grown slightly, but are still in the nanocrystalline regime. YSZ peaks are again observed, corresponding to (101), (110) and (112) crystallographic planes, and match well with theoretical  $2\theta$  values. Intensity of these reflections is increased in comparison with those of the un-treated sample, indicating either an increase in the crystalline content or grain growth of the YSZ coating as a result of the hydrothermal treatment.

Lastly, results from XRD of the microwave-annealed YSZ/HA coating are shown in Figure 4-32 and Table 4-9. HA peaks of this spectra exhibit much greater intensity at (002), (211), (112) and (300) reflections and correspond very closely to theoretical  $2\theta$

values. YSZ peaks are observed, corresponding to (101), (110), (112) and (211) reflections, also having much higher intensity compared with the un-treated and hydrothermally annealed samples. This data suggests that the microwave treatment was effective in either forming crystalline HA from amorphous HA or in increasing a nanocrystalline HA phase to a crystallite size which is detectable using XRD.

SEM-EDX determined that Ca:P ratio of as-deposited coatings was 1.92, whereas microwave annealed coatings exhibited an average Ca:P ratio of 1.81, approaching the stoichiometric value of 1.67 for crystalline HA.

Evaluation of molecular groups on the surface of as-deposited, hydrothermally-annealed and microwave-annealed samples was performed using FTIR.

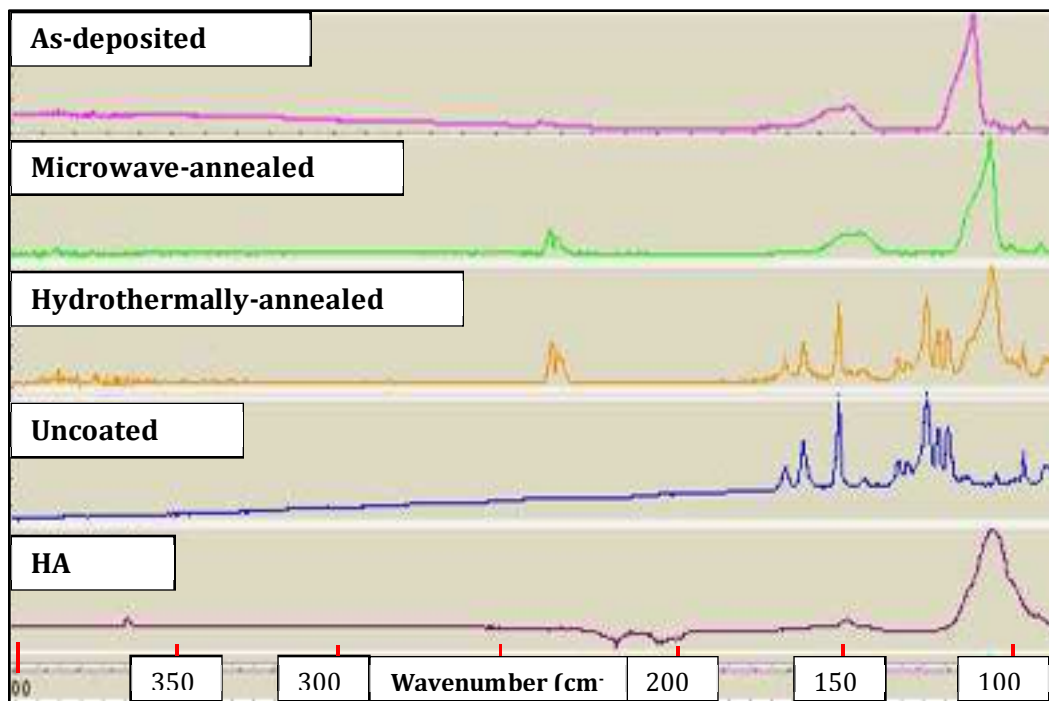


Figure 4-33. FTIR Spectra on various surfaces

Figure 4-33 shows resulting spectra from FTIR measurements on as-deposited (AD), hydrothermally-treated (HT) and microwave-annealed (MW) YSZ/HA coating surfaces. HA target material and uncoated PEEK were also scanned for use as references in identifying functional groups within the coatings. The HA target exhibits an absorption peak at approximately  $3650\text{cm}^{-1}$ , corresponding to the hydroxyl group ( $\text{OH}^-$ ) of crystalline hydroxyapatite, as well as absorption peaks of the phosphate group at approximately  $1084\text{cm}^{-1}$ . Comparatively, IR spectra of as-deposited and microwave-annealed YSZ/HA coating surfaces do exhibit the phosphate peak, but only broad slopes of low height are seen between  $3500$  and  $3700\text{cm}^{-1}$ , indicating a dehydroxylated state (removal of  $\text{OH}^-$  group) of the deposited hydroxyapatite coating that is often resulted from sputter deposition process and heat treatment methods. The hydrothermally-annealed coating surface exhibits the phosphate group around  $1084\text{cm}^{-1}$  as well peaks of low intensity between  $3600$  to  $3800\text{cm}^{-1}$ , which may be indicative of a nanocrystalline HA coating phase on this surface. All coating surfaces displayed some absorption peaks corresponding to the underlying PEEK substrate, which are seen in the range of  $1300$  to  $1700\text{cm}^{-1}$  and at approximately  $900\text{cm}^{-1}$ . Peaks associated with the YSZ coating layer were not observed in these FTIR spectra, due to the low wavenumber associated with YSZ absorption peaks (monoclinic YSZ –  $740\text{cm}^{-1}$ , tetragonal YSZ –  $164$ ,  $467$  and  $339\text{cm}^{-1}$ , cubic YSZ –  $358$  and  $628\text{cm}^{-1}$ ) [187] which fall outside the range of detection of the attenuated total reflectance (ATR) insert used in this research.

#### 4.4.6. Biological Response

Biological tests were conducted on surfaces of uncoated PEEK, as-deposited YSZ/HA coating and microwave-annealed YSZ/HA coating; these sample sets were selected after HA crystallinity of each sample type was determined using microstructural observation and compositional analysis. In this way biological response was measured on a control surface (uncoated PEEK), amorphous HA surface (as-deposited coating), and crystalline HA surface (microwave-annealed).

Figure 4-34 demonstrates the percentage of osteoblast cells attached to the surface of each sample type after an initial period of 6 hours. The microwave-annealed coating surface performed the best out of the three sample types, having 59.3% of cells attached after 6 hours, followed by the as-deposited coating surface with 52.8% and the uncoated PEEK surface with 49.8%.

The growth of these cells on each surface was measured at longer time periods of 1 and 3 days by measurement of dsDNA produced. Shown in Figure 4-35, dsDNA content (in  $\mu\text{g}/\mu\text{L}$ ) increased exponentially on each sample surface between days 1 and 3, which is the normal growth behavior of healthy cells. Among the three surfaces, the microwave-annealed YSZ/HA coating surface had a much higher dsDNA content at the end of the three-day period, with an average of  $7.7 \mu\text{g}/\mu\text{L}$ , compared to 2.8 and  $1.8 \mu\text{g}/\mu\text{L}$ , on uncoated PEEK and as-deposited YSZ/HA coating surfaces, respectively. The microwaved coating surface is shown to encourage the highest number of healthy cells growing on its surface, at least within a 3 -day initial attachment and growth process.

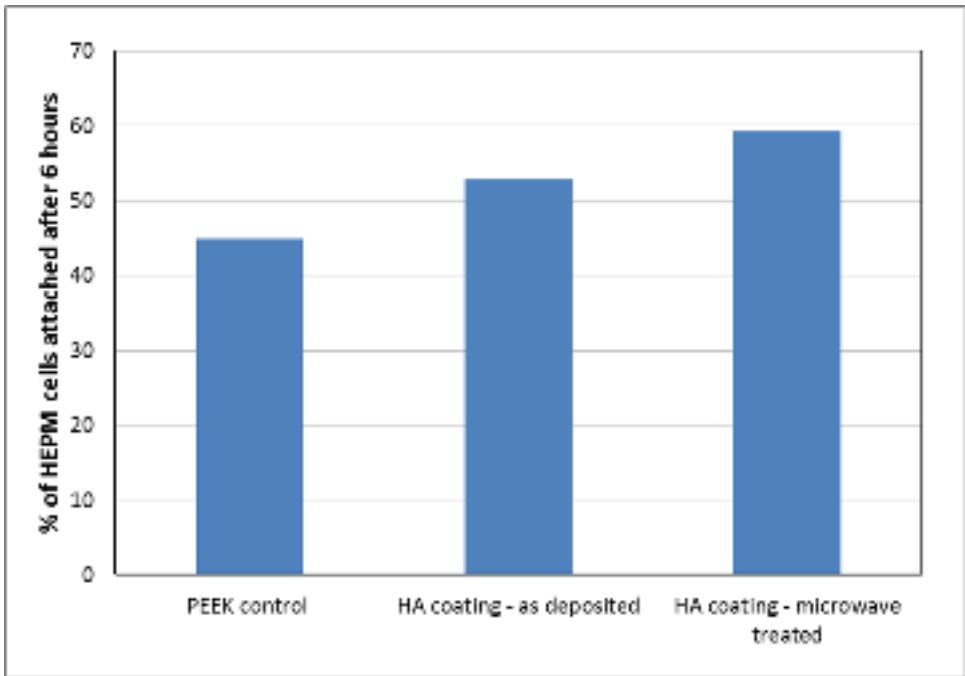


Figure 4-34. Initial osteoblast cell attachment to sample surfaces

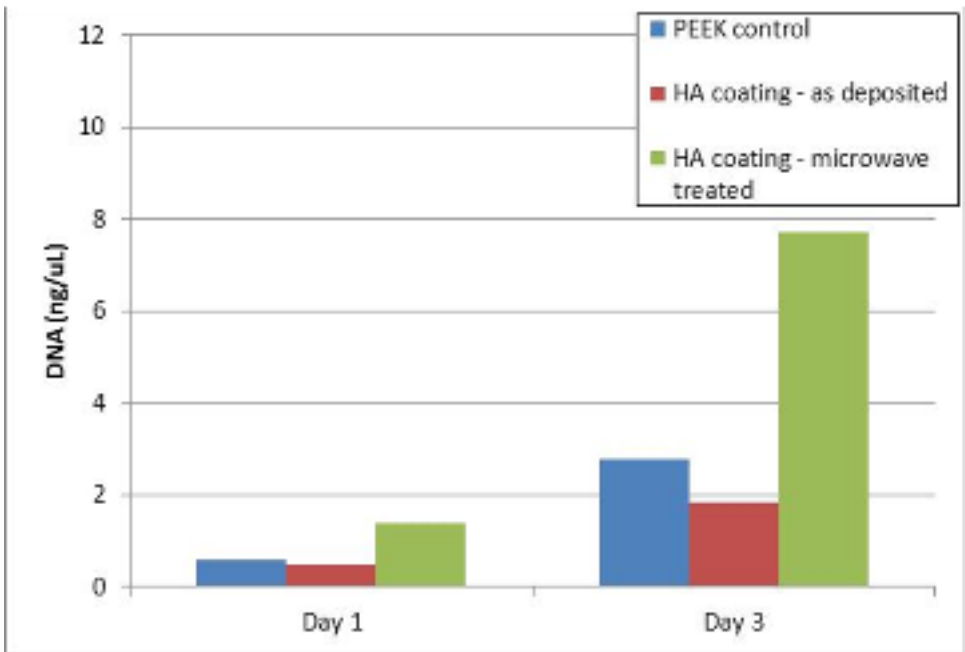


Figure 4-35. dsDNA concentration on sample surfaces at day 1 and day 3

#### 4.5. Discussion

Physical and mechanical properties of the 2-layer YSZ/HA coating were initially studied before attempting to establish a method of crystallization for the HA layer. Coating adhesion strength was initially very low as a result of the vast differences in chemical and mechanical properties between the two interface materials, PEEK and YSZ; adhesion was attributed only to mechanical bonding between the YSZ coating and the PEEK substrate. Adhesion strength was increased initially by increasing surface roughness, and ultimately enhancing the mechanical interlocking as surface area is increased, resulting in an average adhesion strength of 15.1 MPa. In order to be considered for load-bearing implant surfaces, coating adhesion strength should be at least 30MPa, to be able to withstand shear and normal forces encountered while in service and to develop a coating with improved adhesion strength compared with those of commercially-produced implants. While in situ heating has been proven effective for maximizing coating adhesion strength of physical vapor-deposited coatings on metallic substrates, by inducing diffusion and causing an atomically-intermixed coating/substrate interface to be formed, the use of excessive heat during coating of polymers is not suitable. Plasma activation, performed before deposition of the YSZ/HA coating, was effective in significantly enhancing the coating adhesion strength compared with surface roughening alone, raising the average adhesion strength from 15.1 MPa to 33.4 MPa without the use of elevated temperature. This method is thought to be particularly effective in the case of enhancing YSZ adhesion strength to the PEEK

substrate surface due to the prevalence of a large number of oxygen bonds contained in each material. Exposure of PEEK with O<sub>2</sub> plasma has been shown to modify its surface chemistry breaking carbon-carbon double bonds and creating new carbon-oxygen bonds, effectively increasing the oxygen content of the polymer surface [119]. This highly oxidized surface has a higher functionality and is able to bond more intimately with oxygen-containing thin films. The improvement in adhesion strength due to plasma activation was found to be maximized after 10 minutes of exposure to the O<sub>2</sub> plasma, after which adhesion strength was unaffected. It is suggested that after 10 minutes the PEEK surface is saturated in terms of the number of oxygen bonds that can be created.

YSZ has been proven to be biocompatible and, when incorporated into bioactive coatings, the intention is primarily to increase toughness of a brittle ceramics [49]. The inclusion of YSZ in the coating of PEEK substrates in this research was initially implemented with the goal of providing a heat-shielding effect to the PEEK surface during post-deposition heat treatments aimed at forming a crystalline HA coating. Traditional thermal barrier coatings of YSZ exhibit thicknesses of 100µm or more in order to withstand exposure to elevated temperature, highly oxidizing environments for long durations. However, when used as a thermal barrier coating on micro- and nano-scale components where heat is often experienced in shorter time durations, such as in integrated circuits, YSZ thin films of less than 2µm have been proven effective [152,153]. Stud-pull coating adhesion testing of the YSZ/HA-coated PEEK samples as-

deposited and after the various heat treatment methods demonstrated that coating adhesion was not altered as a result of the heat treatments, with the exception of the KrF laser-annealed samples, indicating that the PEEK surface was not melted or otherwise degraded during heating of the coatings.

Additionally, it was observed that the YSZ coating layer is deposited in a crystalline form, exhibiting columnar-shaped grains which are equiaxed, oriented perpendicular to the substrate surface, as predicted by the structure-zone model (Figure 2-13) for crystalline films produced by sputtering at low pressures with low substrate temperatures. As seen in Figure 4-25a, an SEM image of the YSZ coating without HA shows the YSZ crystal grains having a diameter of 30-100nm, resulting in a top coating surface that contains a small percentage of local porosity, resulting from voids between columnar grains, and exhibits a nano-scale surface roughness. These properties of the YSZ top coating surface are suggested to play a role in enhancing the mechanical interlocking of the HA coating layer and in increasing the cohesive strength within the total YSZ/HA coating; as demonstrated in Table 4-6, most sample types exhibited less than 15% occurrence of cohesive failure during the stud-pull coating adhesion strength test, indicating a high average cohesive strength within the coatings. An additional and unforeseen benefit of the YSZ coating layer is the possible role of acting as a nucleation site for the formation of HA crystal grains growing on top of the YSZ surface upon heating. Figures 4-28 and 4-29 show that the HA crystals formed as a result of microwave annealing have similar orientation and diameter as those of YSZ. It

is suggested that the presence of an existing crystal structure beneath the HA coating may act to lower the activation energy for the formation of an HA crystalline layer during heat treatment processes.

As opposed to YSZ which forms a crystalline structure upon sputter deposition, HA coatings deposited using sputtering techniques are known to be amorphous. Microstructural observation of the as-deposited YSZ/HA coating cross-sections revealed that the HA coating layer did not contain any crystalline features; XRD spectra also exhibited a lack of any peaks associated with crystalline HA. Among the heat treatment methods attempted in this research, microwave annealing was shown to be the most effective in causing a transformation of the amorphous as-deposited HA coating layer into crystalline HA. Crystalline features, of similar shape and orientation to those of the YSZ coating layer were observed in SEM images of cross-sections; crystallinity of the HA layer was confirmed by the XRD spectrum (Figure 4-32) of the microwave-treated sample, which exhibited clear peaks associated with the major phases of crystalline HA (Table 4-9) at  $2\theta$  values close (with 0.1 degrees) to those of theoretical values from JCPDS standards.

Laser annealing of the YSZ/HA coatings in this research did not prove to be effective. While it has been shown that pulsed excimer laser treatment can cause a phase transformation of amorphous CaP thin films into crystalline HA, the success of this treatment is highly dependent on selection of an appropriate laser wavelength; as previously described, HA has an optical absorption threshold of approximately 200nm

[159,160], such that lasers of lower wavelength are absorbed within the HA, while higher wavelength lasers are expected to pass through the film without causing the required atomic vibration to produce heating. Due to the scarcity and cost associated with excimer laser systems, only KrF (248nm) and ArF (193nm) lasers were accessible in this research. As shown in Figure 4-22, exposure to KrF laser, even at short duration (25ns) and low fluence ( $200\text{mJ}/\text{cm}^2$ ), caused ablation of the coating, leaving the PEEK substrate completely exposed, and resulting in low coating adhesion in the coating area surrounding the laser-treated region of the sample (Table 4-5). ArF laser treatment did not cause damage to the coating or to the coating/substrate interface as shown in Table 4-5, however the laser energy of this system was unable to be tuned to a high enough level to cause sufficient laser fluence; laser fluence of the ArF laser pulses used were in the range of  $10\text{-}18\text{ mJ}/\text{cm}^2$ , much lower than the required values of laser systems reported in literature [160, 161].

Hydrothermal annealing of the YSZ/HA coatings resulted in very minor changes in the HA coating microstructure, as shown in coating cross-section images and XRD spectra. As seen in Figure 4-24, microstructural observation of the YSZ/HA coating revealed that while some areas of the HA coating layer appeared to show beginnings of possible HA crystal growth, the HA layer appeared mostly unaffected, having almost no microstructural features. XRD analysis (Figure 4-30) also demonstrated very low intensity peaks associated with HA crystallographic planes, suggesting that the HA coating layer was still mostly amorphous or composed of a finely nano-grained crystal

structure. It is suspected that hydrothermal annealing with longer exposure or elevated temperature/pressure steam can result in a higher degree of crystallinity within the HA coating.

FTIR analysis was performed on the coatings to evaluate the presence of phosphate [PO<sub>4</sub>-] and hydroxyl [OH-] groups to confirm the presence of HA. FTIR spectra (Figure 4-33) show the peaks of phosphate groups present in all coating at 1084cm<sup>-1</sup>, while the [OH-] peak, seen at 3650cm<sup>-1</sup> in the spectrum of the HA target, is non-distinguishable in the spectra of the coatings. The absence of OH groups in the spectra of coatings suggests a dehydroxylated state of the HA coating layers. It has reported that HA can be decomposed into other calcium phosphate compounds while deposited using low pressure physical vapor deposition methods, such as IBAD or sputtering, or during post-deposition heat treatment [33, 63]. The HA is converted to oxyhydroxyapatite (OHA), with the formula Ca<sub>10</sub>(PO<sub>4</sub>)<sub>6</sub>(OH)<sub>2-2x</sub> \* O<sub>x</sub>Δ<sub>x</sub>, in which Δ represents the vacancy, and x is less than 1 [188,189]. While this effect is detrimental due to the higher solubility of OHA compared with HA, it has been proven that dehydroxylated HA coatings can be returned to stoichiometric HA by exposure to water vapor during or after heat treatment [190]. This suggests that while hydrothermal treatment may not be as effective in crystallizing HA as microwave annealing, it may serve a purpose in the rehydroxylation of HA after microwave treatment. It is also suggested that water vapor may be introduced into the microwave cavity during microwave annealing to prevent further dehydroxylation of the sputtered HA coating

and to provide an excess of [OH<sup>-</sup>] during the phase transformation from amorphous to crystalline HA.

The Ca:P ratio was lowered from 1.92 to 1.81 as a result of microwave annealing. It has been reported that the Ca/P ratio on the top coating surfaces of sputtered coatings is in the range of 1.6 to 2.6, which, on average, is higher than the stoichiometric value of 1.67 for HA [191,192,193,194]. These higher Ca/P ratios occur in the coating, even when the sputtering target is confirmed to be stoichiometric HA. It has been hypothesized that the differences in Ca/P ratio between the target and sputtered coatings are attributed to preferential sputtering of calcium [191]. There is a possibility of the lighter phosphorus ions being pumped away in the presence of very high vacuum levels before it reaches the substrate surface [195]. It has also been suggested that the phosphorus ions maybe weakly bound to the substrate surface and are therefore easily sputtered away, or “re-sputtered”, by incoming ions or electrons [196].

Finally, biological response was measured using a human osteoblast cell line, comparing the bioactivity of the amorphous HA top coating layer with that of the microwave-annealed crystalline HA top coating layer, as well as an uncoated PEEK surface as a control group. Shown in Figures 4-34 and 4-35, the amorphous HA coated samples and the PEEK control group exhibited similar attachment of osteoblast cells at all measured time points, while the crystalline HA top layer of the microwave-annealed samples exhibited a much higher number of cells attached at 6 hours, 1 day and 3 days, suggesting that this surface is favorable in terms of cell affinity. Cellular response,

especially in the initial stages of attachment and proliferation, is dependent up on a number of factors, including surface chemistry and surface roughness. It is suggested that the preferred biological response to the microwave-annealed samples is not only due to the bioactive HA surface, but also to the increased nanoscale surface roughness, resulting from the microstructure of the crystalline HA top surface (Figure 4-29). Reduced solubility of the crystalline HA coating may also explain its increased cell attachment, while the amorphous HA coating dissolves rapidly following introduction into the physiological fluid, possibly explaining its slightly lower cell attachment compared with the PEEK control (Figure 4-35).

#### **4.6. Summary**

To summarize, dual layer coatings of YSZ and HA with total coating thickness of approximately 1.2 $\mu$ m were deposited onto PEEK substrates by radio-frequency magnetron sputtering. Initial coating adhesion strength of 15.1 MPa, measured by stud-pull coating adhesion testing, was increased to 33.4 MPa as a result pre-deposition exposure of the PEEK substrates with an O<sub>2</sub> plasma. Microstructural and compositional analysis by SEM and XRD revealed that the YSZ layer (400-450nm) exhibited a crystalline structure as-deposited, with columnar shaped grains oriented along the growth direction, while the HA layer (700-800nm) was shown to be amorphous as-deposited. Various post-deposition heat treatments were attempted for the purpose of forming a crystalline HA coating layer, including laser annealing, hydrothermal

annealing and microwave annealing, all of which have been studied as lower temperature alternatives to the traditional furnace annealing technique used in post-deposition crystallization of HA coatings. Of the three methods, microwave annealing was determined to be the most effective, producing a crystalline HA microstructure without causing damage to the PEEK substrates or weakening the adhesive or cohesive strengths of the coating. SEM observation of the coating cross-sections revealed that after microwave annealing, the HA coating exhibited a columnar crystalline microstructure, similar to that of the underlying YSZ crystalline layer. It is suggested that the existence of the crystalline YSZ layer aids in the formation of the HA layer upon heating, possibly lowering the activation energy for crystallization as the YSZ crystal grains act as nucleation sites for the subsequent HA grain formation. SEM-EDX showed that the HA coating layer has a Ca:P ratio close to that of stoichiometric HA, before and after crystallization, while FTIR revealed that the HA is hydroxyl-deficient, indicating a need for water vapor exposure, either during or after heat treatment. Finally, culture tests showed a significant increase in initial cell attachment and growth on the microwave-annealed coating samples, suggesting that this surface is more stable and provides increased surface area for cell attachment as compared with uncoated PEEK and amorphous HA surfaces.

## CHAPTER 5: CONCLUSIONS

In the preliminary study, functionally-graded hydroxyapatite coatings doped with silver (FGHA-Ag) on titanium substrates, which had been previously developed, were studied in terms of dissolution behavior and biological response. It was determined that the release of Ag from the FGHA-Ag coatings was controlled by the functionally graded microstructure, with Ag being released rapidly at first, as a result of the mostly amorphous top coating layer, and then gradually decreasing as the coating microstructure became more crystalline towards the substrate/coating interface. This Ag release profile is desired for biomedical implants, as the infection chances associated with commonly found bacteria are highest within the initial stages after implantation. FGHA-Ag1 and FGHA-Ag2 coatings, with 1 and 3 wt% Ag respectively, were found to promote optimal osteoblast attachment and growth, compared with FGHA and control surfaces, whereas FGHA-Ag3 coating was determined to exhibit toxicity to osteoblast cells, as a result of its high Ag content (6.6 wt%). From these studies, it was concluded that the optimal Ag-doping for FGHA coatings is within the range exhibited by FGHA-Ag1 and FGHA-Ag2 (between 1 and 3 wt%), in order to release Ag at a sufficient rate as to produce an antibacterial effect, while maintaining an Ag concentration that does not inhibit the growth of osteoblast cells.

The main focus of this research has been on the development and optimization of a similar hydroxyapatite coating on polymer (PEEK) substrates. Recently, PEEK has emerged as an optimal substitute for titanium in the development of spinal fusion

cages. While titanium has a proven record of biocompatibility and represents the most common metallic material used in biomedical implants, it possesses major limitations for use in spinal fusion cages, due to its high stiffness compared with vertebral bone and most importantly, to its incompatibility with radiographic methods used in the clinical assessment of bone fusion after spinal implant surgery. PEEK has been shown to possess suitable mechanical properties, radiolucency, and has been recognized by the FDA as an implantable biomaterial. As with titanium, PEEK is a bioinert material which is tolerated biologically, but is incapable of forming direct functional and chemical bonds with newly forming bone. Therefore, bioactive coatings are applied to PEEK spinal implants in order to increase its bioactivity and lead to faster osseointegration of PEEK implants. Few studies have been reported on the coating of PEEK implants; most attempts have used the plasma-spraying method, following the commercial method for coating titanium implants. While plasma-sprayed HA coatings can promote greater bone attachment, several problems have been cited including weak coating adhesion and non-homogenous microstructure strength, which lead to rapid dissolution of the coating and can ultimately cause implant loosening and failure. In an effort to improve the HA coating characteristics on PEEK implants, this research has investigated HA coating of PEEK by RF magnetron sputtering in order to produce thin, well-adhered coatings with uniform, homogenous microstructures. Due to the amorphous nature of sputtered HA films and the temperature sensitivity of PEEK, alternative methods of HA crystallization were explored in order, and YSZ was used as an intermediate thermal

barrier coating between the PEEK substrate and the HA coating to provide heat shielding during the post-deposition heat treatments.

The dual-layer coating of approximately 1.2 $\mu\text{m}$ , consisting of a YSZ layer of  $\sim$  450nm and an HA layer of  $\sim$  750nm, initially exhibited an average adhesion strength of 15.1 MPa to the PEEK substrate. In order to produce a coating with sufficient adhesion for use on implants, plasma activation was employed on the PEEK substrates before deposition and resulted in an increase in coating adhesion strength to 33.4 MPa, which is significantly higher than that of existing HA-coated PEEK materials, and higher than commercially produced HA-coated metallic implants; this increase in coating adhesion is attributed to a higher oxygen content as a result of the high energy O<sub>2</sub> plasma, which increases wettability, surface energy and affinity of coating materials.

Microstructural and compositional analysis by SEM and XRD revealed that the YSZ layer exhibited a crystalline structure as-deposited, with columnar shaped grains oriented along the growth direction, while the HA layer was shown to be amorphous as-deposited. Post-deposition heat treatments of hydrothermal, laser and microwave annealing were studied for the purpose of forming a crystalline HA coating layer, which is necessary in order to provide long-term stability of the coating. Of the three methods, microwave annealing was determined to be the most effective, producing a crystalline HA microstructure without causing damage to the PEEK substrates or weakening the adhesive or cohesive strengths of the coating. SEM observation of the coating cross-sections revealed that after microwave annealing, the HA coating exhibited a columnar

crystalline microstructure, similar to that of the underlying YSZ crystalline layer. It is suggested that the existence of the crystalline YSZ layer aids in the formation of the HA layer upon heating, possibly lowering the activation energy for crystallization as the YSZ crystal grains act as nucleation sites for the subsequent HA grain formation. SEM-EDX showed that the HA coating layer has a Ca:P ratio close to that of stoichiometric HA, before and after crystallization, while FTIR revealed that the HA is hydroxyl-deficient, indicating a need for water vapor exposure, either during or after heat treatment. Finally, culture tests showed a significant increase in initial cell attachment and growth on the microwave-annealed coating samples, suggesting that this surface is more stable and provides increased surface area for cell attachment as compared with uncoated PEEK and amorphous HA surfaces.

## CHAPTER 6: SUGGESTIONS FOR FUTURE RESEARCH

It is suggested that future research investigate and compare the coating of PEEK with HA by similar physical vapor deposition methods, such as ion beam assisted deposition (IBAD), which has been shown to produce dense and uniform HA coatings on titanium with excellent coating adhesion owing to the atomically intermixed interface produced by high energy ion bombardment. It is possible that the combination of plasma activation of the PEEK surface along with IBAD coating of HA can further increase the coating adhesion strength.

There is also a need to improve the dehydroxylated state of the HA coatings produced in this research. Development of a microwave system with a method of introducing water vapor into the chamber during heating may result in a crystalline HA coating without dehydroxylation.

Finally, it seems necessary to improve the HA coatings produced on PEEK substrates to the level of those developed on titanium by forming a functionally graded hydroxyapatite (FGHA) coating, in order to take advantage of the desirable properties associated with a crystalline HA layer near the substrate interface with crystallinity decreasing towards the top coating surface. This may be accomplished by a step-wise coating/crystallization procedure, in which the HA is deposited, followed by a crystallization heat treatment, followed by deposition of subsequent HA layers. Similarly, Ag incorporation into HA coatings on PEEK should be studied in order to add an antibacterial effect to these coatings as well.

## REFERENCES

1. Andersson G. Epidemiology of spinal disorders. In: Frymoyer JW, ed. *The Adult Spine: Principles and Practice*. New York: Raven Pr; 1991.
2. Frymoyer J, Durett C. The economics of spinal disorders. In: Frymoyer JW, ed. *The Adult Spine: Principles and Practice*. 2d ed. Philadelphia: Lippincott-Raven; 1997:143-50.
3. Birkmeyer N, Weinstein J. *Effective Clinical Practice*. 1999;2(5);218-227.
4. Walker B: The Prevalence of Low Back Pain: A Systematic Review of the Literature from 1966 to 1998. *Journal of Spinal Disorders* 2000, 13(3):205-217.
5. Freburger J, Jackman A, Castel L, The rising prevalence of chronic low back pain. *Arch Intern Med*. 2009;169(3):251-258.
6. <http://www.mdguidelines.com/spinal-fusion/definition>
7. Kurtz, S. *Spine Technology Handbook*. Boston: Elsevier Academic Press; 2006.
8. Pichelmann M, Lenke L, Bridwell K, Good C, O'Leary P, Sides B. Revision rates following primary adult spinal deformity surgery: six hundred forty-three consecutive patients followed-up to twenty-two years postoperative. *Spine* 2010(35)2:219-226.
9. Michelson G, Griffith, L. (2005). BAK/C Interbody Fusion System: A Threaded Cylindrical Cage for Cervical Fusion. In Kim D, Vaccaro A, Fessler R. (Eds.), *Spinal Instrumentation: Surgical Techniques* (232-240). New York: Thieme Medical Publishers.
10. McAfee PC. Current Concepts Review — Interbody Fusion Cages in Reconstructive Operations on the Spine". *The Journal of Bone and Joint Surgery* 1999(81);6: 859–880.
11. [http://www.merries.com.tw/product\\_2.html](http://www.merries.com.tw/product_2.html)
12. [http://www.umm.edu/spinecenter/education/anterior lumbar interbody fusion with intervertebral cages.htm](http://www.umm.edu/spinecenter/education/anterior_lumbar_interbody_fusion_with_intervertebral_cages.htm)
13. <http://www.spineuniverse.com/exams-tests/bone-grafts-new-developments>

14. [http://www.spine.org/Documents/bone\\_grafts\\_2006.pdf](http://www.spine.org/Documents/bone_grafts_2006.pdf)
15. <http://www.cdc.gov/OralHealth/Infectioncontrol/faq/allografts.htm>
16. Hench, LL. Bioceramics: From Concept to Clinic. *Journal of the American Ceramic Society* 1991(74):1487.
17. Jaffe WL, Scott DF. Current concepts review: total hip arthroplasty with hydroxyapatite-coated prostheses. *J Bone Jt Surg* 1996(78A):1918–1934.
18. Thomas KA. Hydroxyapatite coatings. *Orthopedics* 1994(17): 267–78.
19. Ducheyne P, Cuckler JM. Bioactive ceramic prosthetic coatings. *Clin Orthop Rel Res* 1992(276):102–114.
20. Kushner A. Evaluation of Wolff's Law of bone formation. *The Journal of Bone & Joint Surgery* 1940(22):589-596.
21. Taddei EB, Henriques VA, Silva CR, Cairo CA. Production of new titanium alloy for orthopedic implants. *Materials Science and Engineering C* 2004(24);5:683-687.
22. Söderlund CH, Pointillart V, Pedram M, Andrault G, Vital JM. Radiolucent cage for cervical vertebral reconstruction: A prospective study of 17 cases with 2-year minimum follow-up. *European Spine Journal* 2004(13);8: 685-690.
23. Senegas J. Mechanical supplementation by non-rigid fixation in degenerative intervertebral lumbar segments: the Wallis system. *European Spine Journal* 2002(11);S2:S164–9.
24. Hench, LL. Bioceramics. *J Am Ceram Soc* 1998(81):1705–1728.
25. Suchanek W, Yoshimura M. Processing and properties of hydroxyapatite-ased biomaterials for use as hard tissue replacement implants. *J Mater Res* 1998(13):94–117.
26. LeGeros RZ. Biodegradation and bioresorption of calcium phosphate ceramics. *Clin Mater* 1993(14):1221–1227.
27. Darimont G, Cloots R, Heinen E, Seidel L, Legrand R. In vivo behaviour of hydroxyapatite coatings on titanium implantsa quantitative study in the rabbit. *Biomaterials* 2002(23);12:2569–2575.

28. Webster, T.J., C. Ergun, R.H. Doremus, R.W. Siegel, and R. Bizios, Enhanced osteoclast-like cell functions on nanophase ceramics. *Biomaterials* 2001 (22);11: 1327-1333.
29. Webster, T.J., C. Ergun, R.H. Doremus, R.W. Siegel, and R. Bizios, Enhanced functions of osteoblasts on nanophase ceramics. *Biomaterials*, 2000(21);17: 1803-1810.
30. Darimont G, Cloots R, Heinen E, Seidel L, Legrand R. In vivo behaviour of hydroxyapatite coatings on titanium implants a quantitative study in the rabbit. *Biomaterials* 2002(23);12:2569–2575
31. Epinette JA, Manley MT. Fifteen years of clinical experience with hydroxyapatite coating in joint arthroplasty. Paris: Springer; 2004.
32. Donaldson AJ, Thomson HE, Harper NJ, Kenny NW. Bone cement implantation syndrome. *British Journal of Anaesthesia* 2009(102):12–22.
33. Blalock TL, Bai X, Narayan R, Rabiei A. Effect of substrate temperature on mechanical properties of calcium phosphate coatings. *J Biomed Mater Res B* 2008(85):60–67.
34. Radin S, Ducheyne P. Plasma spraying induced changes of calcium phosphate ceramic characteristics and the effect on in vitro stability. *Mater Med* 1992(3):33–42.
35. Filiaggi MJ, Coombs NA, Pilliar RM. Characterization of the interface in the plasma-sprayed HA coating/Ti-6Al-4V implant system. *J Biomed Mater Res* 1991(25):1211–1230.
36. Rabiei A, Thomas B. Processing and Development of Nano-Scale HA Coatings for Biomedical Application. *Proceedings of the Materials Research Society* 2004 (845):193-199.
37. Cooley DR, Vandellen AF, Burgess JO, Windeler AS. The advantages of coated titanium implants prepared by radiofrequency sputtering from hydroxyapatite. *Journal of prosthetic dentistry* 1992(67);1:93-100.
38. Rabiei A, Thomas B, Neville B, Lee JW, Cuomo J. A novel technique for processing functionally graded HA coatings. *Mater Sci Eng C* 2007(27):523–528.

39. Rabiei A, Thomas B, Jin C, Narayan R, Cuomo J, Yang Y, Ong JL. A study on functionally graded HA coatings processed using ion beam assisted deposition with in situ heat treatment. *Surf Coatings Technol* 2006(200):6111–6116.
40. Bai X, Sandukas S, Appleford M, Ong JL, Rabiei A. Deposition and investigation of functionally graded calcium phosphate coatings on titanium. *Acta Biomaterialia* 2009(5):3563-3572.
41. Chopra, I. The increasing use of silver-based products as antimicrobial agents: a useful development or a cause for concern?. *The Journal of antimicrobial chemotherapy* 2007(59);4:587–590.
42. Klueh U, Wagner V, Kelly S, Johnson A, Bryers J. Efficacy of Silver-Coated Fabric to Prevent Bacterial Colonization and Subsequent Device-Based Biofilm Formation. *Journal of Biomedical Materials Research Part B: Applied Biomaterials* 2000(53):621-631.
43. Yamanaka M, Hara K, Kudo J. Bactericidal Actions of a Silver Ion Solution on *Escherichia coli*, Studied by Energy-Filtering Transmission Electron Microscopy and Proteomic Analysis. *Applied and Environmental Microbiology* 2005(71);11:7589-7593.
44. Campoccia D, Montanaro L, Arciola C. The significance of infection related to orthopedic devices and issues of antibiotic resistance. *Biomaterials* 2006(27);11:2331-2339.
45. Chen W, Liu Y, Courtney H, Bettenga M, Agrawal C, Bumgardner J, Ong J. In vitro anti-bacterial and biological properties of magnetron co-sputtered silver-containing hydroxyapatite coating. *Biomaterials* 2006(27);32:5512-5517.
46. Noda I, Miyaji F, Ando Y, Miyamoto H, Shimazaki T, Yonekura Y, Miyazaki M, Mawatari M, Hotokebuchi T. Development of novel thermal sprayed antibacterial coating and evaluation of release properties of silver ions. *Journal of Biomedical Materials Research Part B: Applied Biomaterials* 2008(89B):2.
47. Chang E, Chang W, Wang B, Yang C. Plasma spraying of zirconia-reinforced hydroxyapatite composite coatings on titanium, Part I. Phase, microstructure and bonding strength. *Journal of Materials Science: Materials in Medicine* 1997(8);4:193-200.

48. Chou B, Chang E. Plasma-sprayed zirconia bond coat as an intermediate layer for hydroxyapatite coating on titanium alloy substrate. *Journal of Materials Science: Materials in Medicine* 2002(13);6:589-595.
49. T. Kasuga, Yoshida M, Ikushima A, Tuchiya M, Kusakari H. Stability of Zirconia-Toughened Bioactive Glass/Ceramics: In Vivo Study Using Dogs, *Journal of Materials Science: Materials in Medicine*. 1993(4);36-39.
50. Chou B, Chang E. Plasma sprayed hydroxyapatite coating on titanium alloy with ZrO<sub>2</sub> second phase and ZrO<sub>2</sub> intermediate layer. *Surface and Coatings Technology* 2002(153): 84-92.
51. Wasa K, Kitabatake M, Adachi H. *Thin Film Materials Technology: Sputtering of Compound Materials*. New York: William Andrew, Inc. 2004. 71-78.
52. Lacefield W. (1988), Hydroxyapatite Coatings. *Annals of the New York Academy of Sciences*, 523: 72-80.
53. Hong Z, Luan L, Paik S, Deng B, Ellis D, Ketterson J, Mello A, Eon J, Terra J, Rossi A. Crystalline hydroxyapatite thin films produced at room temperature; an opposing radio frequency magnetron sputtering approach. *Thin Solid Films* 2007(515);17: 6773-6780.
54. Clark DE, Floz DC, West JK. Processing materials with microwave energy. *Materials Science and En Eng A* 2000(287): 153-158.
55. Chou SY, Lo SL, Li NH. Thermal treatment of MSWI fly ash with different additives by microwave heating. *Electric Technology and Civil Engineering (ICETCE)*, 2011 International Conference on 2011(4):808-1812.
56. Zhang G, Leparoux S, Liao H, Coddet C. Microwave sintering of poly-ether-ether-ketone (PEEK) based coatings deposited on metallic substrate. *Scripta Materialia* 2006(55): 621-624.
57. Adams D, Malgas G, Smith R, Massia S, Alford T, Mayer J. Microwave annealing for preparation of crystalline hydroxyapatite thin films. *J Mater Sci* 2006(41):7150-7158.
58. Smith PM, Carey PG, Sigmon TW. Excimer laser crystallization and doping of silicon films on plastic substrates. *Applied Physics Letters* 1997(70):342-344.

59. Tong W, Chen J, Cao Y, Lu L, Feng J, Zhang X. Effect of water vapor pressure and temperature on the amorphous-to-crystalline HA conversion during heat treatment of HA coatings. *Journal of Biomedical Materials Research* 1997(36): 242–245.
60. Ozeki K, Mishima A, Yuhta T, Fukui Y, Aoki H. Bone bonding strength of sputtered hydroxyapatite films subjected to a low temperature hydrothermal treatment. *Bio-Med. Mater. Eng* 2003(13):451-457.
61. Yang C, Lui T, Chang E. Low temperature crystallization and structural modification of plasma-sprayed hydroxyapatite coating with hydrothermal treatment. *Advanced Materials Research* 2007(15): 147–152.
62. Tong W, Chen J, Cao Y, Lu L, Feng J, Zhang X. Effect of water vapor pressure and temperature on the amorphous-to-crystalline HA conversion during heat treatment of HA coatings. *Journal of Biomedical Materials Research* 1997(36): 242–245.
63. Bai, X. (2010). Processing and Characterization of Functionally Graded Hydroxyapatite Coatings for Biomedical Implants. (Doctoral dissertation). Retrieved from ProQuest Dissertations and Theses.
64. Kurtz, SM. "An overview of PEEK Biomaterials." In *PEEK Biomaterials Handbook*. Kurtz, SM (ed). Oxford: Elsevier, 2012. pp2.
65. Green, Stuart and John Devine. "PEEK-OPTIMA Polymer: An Alternative Material for the Development of Long-Term Medical Implant Applications." *BONEZone*. (2004) 3-5.
66. Parker D, Bussink J, van de Grampe HT, Wheatley GW, Dorf EU, Ostlinning E, Reinking K. Polymers, High-Temperature. in *Ullmann's Encyclopedia of Industrial Chemistry*, Wiley-VCH, Weinheim, 2002.
67. Kemmish D. Update on the Technology and Applications of Poly-Aryl-Ether-Ketones 2010. ISBN 978-1-84735-408-2.
68. Victrex PEEK, Product Guide Medical, 1999.
69. Charles E. Carraher, Raymond Benedict Seymour (2003). Seymour/Carraher's polymer chemistry. CRC Press. pp. 43–45.

70. Kumar S, Anderson DP. Crystallization and morphology of poly(aryl-ether-etherketone). *Polymer* 1986(27):329.
71. Blundell DJ, Osborn BN. The morphology of poly(aryl-etherketone). *Polymer* 1983(24):953.
72. Oberg, Erik; Jones, Franklin D.; Horton, Holbrook L.; Ryffel, Henry H. (2000), *Machinery's Handbook* (26th ed.), New York: Industrial Press,
73. Todd, R. H., Allen, D. K., & Alting, L. (1994). *Manufacturing Processes Reference Guide*. New York, NY: Industrial Press Inc.
74. Talbott MF, Springer GS, Berglund LA. The Effects of Crystallinity on the Mechanical Properties of PEEK Polymer and Graphite Fiber Reinforced PEEK. *Journal of Composite Materials* 1987(21);11:1056-1081.
75. Rae PJ, Brown EN, Orlor EB. The mechanical properties of poly(ether-etherketone) (PEEK) with emphasis on the large compressive strain response. *Polymer* 2007(48):598-615.
76. Ferguson S, Visser J, Polikeit, A. The long-term mechanical integrity of non-reinforced PEEK-OPTIMA polymer for demanding spinal applications: experimental and finite-element analysis. *European Spine Journal* 2006(15):149-16.
77. Converse GL, Yue W, Roeder, RK. Processing and tensile properties of hydroxyapatite-whisker-reinforced polyetheretherketone. *Biomaterials* 2007(28);6:927-935.
78. Wang ST, Goel VK, Fu CY, Kubo S, Choi W, Liu CL, Chen TH. Comparison of two interbody fusion cages for posterior lumbar interbody fusion in a cadaveric model. *International Orthopaedics* 2006(30):299-304.
79. Parsons JR, Bhayani S, Alexander H, Weiss AB. Carbon fiber debris within the synovial joint. A time-dependent mechanical and histologic study. *Clinical Orthopaedics and Related Research* 1985(196):69-76.
80. Scholes SC, Unsworth A. Wear studies on the likely performance of CFR-PEEK/CoCrMo for use as artificial joint bearing materials. *J Mater Sci Mater Med* 2009(20):163- 170.

81. Abu Bakar MS, Cheng MHW, Tang SM, Yu SC, Liao K, Tan CT, et al. Tensile properties, tension-tension fatigue and biological response of polyetheretherketone-hydroxyapatite composites for load-bearing orthopedic implants. *Biomaterials* 2003;24(13):2245-50.
82. Abu Bakar MS, Cheang P, Khor KA. Tensile properties and microstructural analysis of spheroid hydroxyapatite-poly (etheretherketone) biocomposites. *Materials Science and Engineering* 2003;A345:55-63.
83. Abu Bakar MS, Cheang P, Khor KA. Mechanical properties of injection molded hydroxyapatite-polyetheretherketone biocomposites. *Composite Science Technology* 2003;63:421-5.
84. Petrovic L, Pohle D, Munstedt H, Rechtenwald T, Schlegel KA, Rupprecht S. Effect of beta-TCP filled polyetheretherketone on osteoblast cell proliferation in vitro. *Journal of Biomedical Science* 2006;13(1):41-6.
85. Yu S, Hariram Kithva P, Kumar R, Cheang P, Aik Khor K. In vitro apatite formation and its growth kinetics on hydroxyapatite/polyetheretherketone biocomposites. *Biomaterials* 2005;26(15):2343-52.
86. Tang SM, Cheang P, AbuBakar MS, Khor KA, Liao K. Tension-tension fatigue behavior of hydroxyapatite reinforced polyetheretherketone composites. *International Journal of Fatigue* 2004;26:49-57.
87. Hansen, DC. Metal Corrosion in the Human Body: The Ultimate Bio-Corrosion Scenario. *The Electrochemical Society Interface* 2008(S);31-34.
88. [http://www.netmotion.com/htm\\_files/advisory/advisor\\_peekmedi.htm](http://www.netmotion.com/htm_files/advisory/advisor_peekmedi.htm)
89. "The effect of sterilization methods on plastics and elastomers." *Plastic Design Library*. 1994 p.173.
90. Jahan MS, Wang C, Schwartz G, Davidson JA. Combined chemical and mechanical effects on free radicals in UHMWPE joints during implantation. *Journal of Biomedical Materials Research* 1991;25(8):1005-17.
91. Li HM, Fouracre RA, Given MJ, Banford HM, Wysocki S, Karolczak S. Effects on polyetheretherketone and polyethersulfone of electron and gamma irradiation. *IEEE Transactions on Dielectrics and Electrical Insulation*. 1999;6(3):295-303.

92. Heiland K, Hill DJ, O'Donnell JH, Pomery PJ. Radiation degradation of poly(arylene ether ketone)s. *Polymers for Advanced Technologies* 1994(5): 116–121.
93. Cizek GR, Boyd LM. Imaging pitfalls of interbody spinal implants. *Spine* 2000;25(20):2633–6.
94. McAfee PC, Boden SD, Brantigan JW, et al. Symposium: a critical discrepancy—a criteria of successful arthrodesis following interbody spinal fusions. *Spine* 2001;26;3:320–34.
95. Modic MT, Steinberg PM, Ross JS, Masaryk TJ, Carter JR. Degenerative disk disease: assessment of changes in intervertebral body marrow with MR imaging. *Radiology* 1988(166):193-199.
96. Onesti ST, Ashkenazi E. The Ray Threaded Fusion Cage for posterior lumbar interbody fusion. *Neurosurgery* 1998(42):200–205.
97. Liao JC, Niu CC, Chen WJ, Chen LH. Polyetheretherketone (PEEK) cage filled with cancellous allograft in anterior cervical discectomy and fusion. *International Orthopaedics* (2008) 32:643–648.
98. Jockish KA, Brown SA, Bauer TW, Merrit K. Biological response to chopped-carbon-fiber-reinforced PEEK. *Journal of Biomedical Materials* 1992;26:133–146.
99. William DF, Mcnamara A. Potential of polyetheretherketone (PEEK) and carbon-fibre-reinforced PEEK in medical applications. *Journal of Materials Science Letters* 1987;6:188–190.
100. Morrison C, Macnair R, MacDonald C, Wykman A, Goldie I, Grant MH. In vitro biocompatibility testing of polymers for orthopaedic implants using cultured fibroblasts and osteoblasts. *Biomaterials* 1995;16:987–992.
101. Wenz LM, Merritt K, Brown SA, Moet A, Steffee AD. In vitro biocompatibility of polyetheretherketone and polysulfone composites. *Journal of Biomedical Materials Resesearch* 1990;24:207–215.
102. Sagomyants KB, Jarman-Smith ML, Devine JN, Aronow MS, Gronowicz GA. The in vitro response of human osteoblasts to polyetheretherketone (PEEK) substrates compared to commercially pure titanium. *Biomaterials* 2008(29): 1563-1572.

103. Rivard CH, Rhalmi S, Coillard C. In vivo biocompatibility testing of PEEK polymer for a spinal implant system: a study in rabbits. *Journal of Biomedical Materials Research* 2002;62(4):488–98.
104. Nieminen T, Kallela I, Wuolijoki E, Kainulainen H, Hiidenheimo I, Rantala I. Amorphous and crystalline polyetheretherketone: mechanical properties and tissue reactions during a 3-year follow-up. *Journal of Biomedical Materials Research* 2008(84A);377-383.
105. Kurtz, S.M., Devine, J.N. PEEK Biomaterials in trauma, orthopedic and spinal implants. *Biomaterials* 2007; 28:4845–4869.
106. Brantigan JW, Steffee AD, Geiger JM. A carbon fiber implant to aid interbody lumbar fusion; mechanical testing. *Spine* 1991;16(6th supplement);S277-S282.
107. McMillin C. Evaluation of PEKEKK composites for spine implants. In: 38th international SAMPE symposium, 1993: p. 591–598.
108. Brantigan JW, Steffee AD. A carbon fiber implant to aid interbody lumbar fusion; two-year clinical results in the first 26 patients. *Spine* 1993;18(14);2106-2107.
109. Cho DY, Liao WR, Lee WY, Liu JT, Chiu CL, Sheu PC. Preliminary experience using a polyetheretherketone (PEEK) cage in the treatment of cervical disc disease. *Neurosurgery* 2002;51(6);1343-1350.
110. Spruit M, Falk RG, Beckmann L, Steffen T, Castelein RM. The in vitro stabilising effect of polyetheretherketone cages versus a titanium cage of similar design for anterior lumbar interbody fusion. *European Spine Journal* 2005;14(8):752-758.
111. van Dijk M, Tunc DC, Smit TH, Higham P, Burger EH, Wuisman PI. In vitro and in vivo degradation of bioabsorbable PLLA spinal fusion cages. *J Biomed Mater Res.* 2002;63(6):752-9.
112. Melnyk A, Chak J, Cripton P, Dvorak M, Oxland T. Shear force measurements on low- and high-stiffness posterior fusion devices. *Medical Engineering and Physics* 2012; in press, doi: <http://dx.doi.org/10.1016/j.medengphy.2011.12.016>.
113. Jiya T, Smit T, Deddens J, Mullender M. Posterior Lumbar Interbody Fusion Using Nonresorbable Poly-Ether-Ether-Ketone Versus Resorbable Poly-L-Lactide-Co-D,L-Lactide Fusion Devices. *Spine* 2009(34);3:233–237.

114. Smit TH, Engels TA, Wuisman PI, et al. Time-dependent mechanical strength of 70/30 Poly(L, DL-lactide): shedding light on the premature failure of degradable spinal cages. *Spine* 2008;33:14–18.
115. Ha S, Kirch M, Birchler F, Eckert K, Mayer J, Wintermantel E, Sittig C, Pfund-Klingenfuss I, Textor M, Spencer N, Guecheva M, Vonmont H. Surface activation of polyetheretherketone (PEEK) and formation of calcium phosphate coatings by precipitation. *Journal of Materials Science: Materials in Medicine* 1997(8): 683-690.
116. Ozeki K, Kobayashi S, Hirakuri K, Aoki H, Fukui Y. Oxygen plasma pre-treatment improves the wear properties of a diamond-like carbon film coated on UHMWPE and PMMA for biomaterials. *Bio-Medical Materials and Engineering* 17 (2007) 175–182.
117. Feddes B, Wolke J, Vredenberg A, Jansen J. Initial deposition of calcium phosphate ceramic on polyethylene and polydimethylsiloxane by rf magnetron sputtering deposition: the interface chemistry. *Biomaterials* 25 (2004) 633–639
118. Shard AG, Badyal JP. Surface oxidation of polyethylene, polystyrene, and PEEK: the synthon approach. *Macromolecules* (1992)25(7);2053–2054.
119. Baalman A, Vissing KD, Born E, Gross A. Surface Treatment of Polyetheretherketone (PEEK) Composites by Plasma Activation. *The Journal of Adhesion* (1994);46:57- 66.
120. Awaja F, Zhang S, James N, McKenzie DR. Enhanced Autohesive Bonding of Polyetheretherketone (PEEK) for Biomedical Applications Using a Methane/Oxygen Plasma Treatment. *Plasma Processes and Polymers* 2010;7:1010–1021.
121. Merrit K, Rodrigo J. Immune Response to Synthetic Materials: Sensitization of Patients Receiving Orthopaedic Implants. *Clinical Orthopaedics & Related Research* 1996(326):71-79.
122. Thomas P, Maier S, Summer B. Allergic reactions to metal implants. *Materialwissenschaft und Werkstofftechnik* 2004(35);12:997-1000.
123. Hallab NJ, Cunningham BW, Jacobs JJ. Spinal Implant Debris-Induced Osteolysis. *Spine* 2003(28);20S:125-138.

124. Wu GM, Hsiao WD, Kung SF. Investigation of hydroxyapatite coated polyether ether ketone composites by gas plasma sprays. *Surface & Coatings Technology* 203 (2009) 2755–2758.
125. Leon B, Jansen JA (eds). *Thin calcium phosphate coatings for medical implants*. 2009 Springer science and business media; New York. Page 2
126. Massas R, Pitarui S, Weinreb MM. Dry-process surface modification for titanium dental implants. *Journal of Dental Research* 1993(72):1005-1008.
127. Martin JY, Schwartz Z, Hummert TW, Schraub DM, Simpson J, Lankford J, Cochran DL, Boyan BD. Effect of titanium surface roughness on proliferation, differentiation, and protein synthesis of human osteoblast-like cells (MG63). *Journal of Biomedical Materials Research* 1995(29):389-401.
128. Lackner JM, Waldhauser W. Inorganic PVD and CVD Coatings in Medicine - A Review of Protein and Cell Adhesion on Coated Surfaces. *Journal of Adhesion Science and Technology* 2010(24):925–961.
129. Rabiei A, Thomas B, Neville B, Lee JW, Cuomo J. A Novel Technique for Processing Functionally Graded HA coatings", *Materials Science & Engineering C* 2001(27):523-528.
130. Sun LM, Berndt CC, Gross KA, Kucuk A. Material fundamentals and clinical performance of plasma-sprayed hydroxyapatite coatings: A review. *Journal of Biomedical Materials Research* 2001(58)5:570-592.
131. LeGeros RZ. Biodegradation and bioresorption of calcium phosphate ceramics. *Clin Mater* 1993;14:65–88.
132. LeGeros RZ. Properties of osteoconductive biomaterials: calcium phosphates. *Clin Orthop Relat Res* 2002;395:81–98.
133. Ito A, Onuma K. (2003) *Crystal Growth Technology*. New York. p525-552.
134. Epinette JA, Manley MT. *Fifteen years of clinical experience with hydroxyapatite coating in joint arthroplasty*. Paris: Springer; 2004.
135. Donaldson AJ, Thomson HE, Harper NJ, Kenny NW. Bone cement implantation syndrome. *British Journal of Anaesthesia* 2009; 102: 12–22.

136. Yang Y, Kim K, Ong JL. A review on calcium phosphate coatings produced using a sputtering process—an alternative to plasma spraying. *Biomaterials* 26 (2005) 327–337.
137. V. Guipont et al. “Bond strength determination of hydroxyapatite coatings on Ti-6Al-4V substrates using the Laser Shock Adhesion Test (LASAT).” *J Biomed Mater Res A*. (2010);95(4):1096-104.
138. R. Y. Whitehead, W. R. Lacefield, and L. C. Lucas. Structure and integrity of a plasma sprayed hydroxylapatite coating on titanium. *Journal of Biomedical Materials Research* 1993(27):1501-1507.
139. Klein C, Patka P, Van Der Lubbe H, Wolke J, De Groot K. *Journal of Biomedical Materials Research* 1991(25):53.
140. Fernandez-Pradas JM, Cleries L, Martinez E, Sardin G, Esteve J, Morenza JL. Influence of thickness on the properties of hydroxyapatite coatings deposited by KrF laser ablation. *Biomaterials* 2001;22:2171–2175.
141. Trommer R, Santos L, Bergmann C. Alternative technique for hydroxyapatite coatings. *Surface and Coatings Technology* 2007(201):9587-9593.
142. Weng WJ, Baptista JL. Sol gel derived porous hydroxyapatite coatings. *Journal of Materials Science-Materials in Medicine* 1998(9);3:159-163.
143. Wie H, Hero H, Solheim T. Hot isostatic pressing-processed hydroxyapatite-coated titanium implants: light microscopic and scanning electron microscopy investigations. *International Journal of Oral and Maxillofacial Implants* 1998(13):837–844.
144. von Wilmowsky C, Lutz R, Meisel U, et al. 2009. In vivo evaluation of b-TCP containing 3D laser sintered poly(ether ether ketone) composites in pigs. *Journal of Bioactive Compatible Polymers* 2009(24);169–184.
145. Cook SD, Rust-Dawicki AM. Preliminary evaluation of titanium-coated PEEK dental implants. *J Oral Implantology*. 1995;21(3):176–81.
146. Ha SW, Gisep A, Mayer J, Wintermantel E, Gruner H, Wieland M. Topographical characterization and microstructural interface analysis of vacuum-plasma-sprayed titanium and hydroxyapatite coatings on carbon fibre-reinforced poly(etheretherketone). *Journal of Materials Science: Materials in Medicine*. 1997;8:891–6.

147. Sprio S, Guicciardi S, Bellosi C, Pezzotti G. Yttria-stabilized zirconia films grown by radiofrequency magnetron sputtering: Structure, properties and residual stresses. *Surface & Coatings Technology* 2006(200);4579-4585.
148. Zhao H, Yu F, Bennett TD, Wadley HN. Morphology and thermal conductivity of yttria-stabilized zirconia coatings. *Acta Materialia* 2006(54);5195–5207.
149. Gsell S, Fischer M, Bauer T, Schreck M, Stritzker B. Yttria-stabilized zirconia films of different composition as buffer layers for the deposition of epitaxial diamond/Ir layers on Si(001). *Diamond & Related Materials* 15 (2006) 479 – 485.
150. Ruddell DE, Stoner BR, Thompson JY. The effect of deposition parameters on the properties of yttria-stabilized zirconia thin films. *Thin Solid Films* 2003(445);14-19.
151. Kuo DH, Chien CH, Huang CH. Zirconia and zirconia–silica thin films deposited by magnetron sputtering. *Thin Solid Films* 2002(47);420–421.
152. Shin J, Li P, Mazumder J. Pulsed laser deposition of the yttria-stabilized zirconia films. *Thin Solid Films* 2008(517);2:648-651.
153. Shaula AL, Oliveira JC, Kolotygin VA, Louro C, Kharton VV, Cavaleiro A. Protective YSZ-based thin films deposited by RF magnetron sputtering. *Vacuum* 83 (2009) 1266–1269.
154. Ohring, Milton. *Materials Science of Thin Films*, 2nd ed. 2002. Elsevier
155. Kimura T, Goto T. Thermal conductivities of yttria-stabilized zirconia films measured by a laser-heating AC method. *Surface & Coatings Technology* 2005 (198); 129– 132.
156. H. Aoki, *Medical Applications of Hydroxyapatite*, Ishiyaku EuroAmerica, Inc, St. Louis, 1994.
157. Ozeki K, Aoki H, Fukui Y. Effect of pH on crystallization of sputtered hydroxyapatite film under hydrothermal conditions at low temperature. *Journal of Materials Science* 2005(40);2837 – 2842.
158. Yang CW, Lui TS, Chang E. Low Temperature Crystallization and Structural Modification of Plasma-Sprayed Hydroxyapatite Coating with Hydrothermal Treatment. *Advanced Materials Research* 2007(15-17);147-152.

159. McCulloch, D (2001). US Patent No. 6,169,014 B1. U.S. Patent and Trademark Office.
160. Feddes B, Vredenberg A, Wehner M, Wolke J, Jansen J. Laser-induced crystallization of calcium phosphate coatings on polyethylene (PE). *Biomaterials* 2005;26:1645-1651.
161. Kurella A, Dahotre N. Laser induced hierarchical calcium phosphate structures. *Acta Biomaterialia* 2006;2(6);677-683.
162. Chaffee, J. US Patent (1939). 2147689. US Patent and Trademark Office.
163. Fang Y, Agrawal DK, Roy DM, Roy R. Fabrication of transparent hydroxyapatite ceramics by microwave processing. *Materials Letters* 1995(23);147.
164. Vaudaux PE, Daniel PL, Waldvogel FA. Host Factors Predisposing to and Influencing Therapy of Foreign Body Infections. In: Bisno AL, Waldvogel FA, editors. *Infections associated with indwelling medical devices*. 2nd ed. Washington, D.C.: ASM Press; 1994. p. 1.
165. Chen W, Liu Y, Courtney HS, Bettenga M, Agrawal CM, Bumgardner JD, Ong JL. In vitro anti-bacterial and biological properties of magnetron co-sputtered silver-containing hydroxyapatite coating. *Biomaterials* 2006;27:5512–5517.
166. Steckelberg JM, Osmon DR. Prosthetic Joint Infections. In: Bisno AL, Waldvogel FA, editors. *Infections associated with indwelling medical devices*. 2nd ed. Washington, D.C.: ASM Press; 1994. p. 259.
167. Nasser S. Prevention and treatment of sepsis in total hip replacement surgery. *Orthop Clin North Am* 1992;23:265–277.
168. Rameshbabu N, Kumar TSS, Prabhakar TG, Sastry VS, Murty K, Rao KP. Antibacterial nanosized silver substituted hydroxyapatite: Synthesis and characterization. *J Biomed Mater Res A* 2007;80A:581–591.
169. Bosetti M, Masse A, Tobin E, Cannas M. Silver coated materials for external fixation devices: In vitro biocompatibility and genotoxicity. *Biomaterials* 2002;23:887–892.
170. Chen YK, Zheng XB, Xie YT, Ding CX, Ruan HJ, Fan CY. Anti-bacterial and cytotoxic properties of plasma sprayed silver-containing HA coatings. *J Mater Sci-Mater Med* 2008;19:3603–3609.

171. Ewald A, Gluckermann SK, Thull R, Gbureck U. Antimicrobial titanium/silver PVD coatings on titanium. *Biomed Eng Online* 2006;5:22.
172. Feng QL, Kim TN, Wu J, Park ES, Kim JO, Lim DY, Cui FZ. Antibacterial effects of Ag-HAp thin films on alumina substrates. *Thin Solid Films* 1998;335:214–219.
173. Harges J, Streitburger A, Ahrens H, Nusselt T, Gebert C, Winkelmann W, Battmann A, Gosheger G. The influence of elementary silver versus titanium on osteoblasts behaviour in vitro using human osteosarcoma cell lines. *Sarcoma*. Vol. 2007; Article No.26539;1-5.
174. Yamamoto A, Mishima S, Maruyama N, Sumita M. A new technique for direct measurement of the shear force necessary to detach a cell from a material. *Biomaterials* 1998;19:871–879.
175. Sandukas S, Yamamoto A, Rabiei A. Osteoblast adhesion to functionally graded hydroxyapatite coatings doped with silver. *J Biomed Mater Res A* 2011; 97A(4); 409-497.
176. Yamaguchi T, Chattopadhyay N, Kifor O, Butters RR, Sugimoto T, Brown EM. Mouse Osteoblastic Cell Line (MC3T3-E1) Expresses Extracellular Calcium (Ca<sup>2+</sup>)-Sensing Receptor and Its Agonists Stimulate Chemotaxis and Proliferation of MC3T3-E1 Cells. *Journal of bone and mineral research* 1998(13):1530–1538.
177. Shu R, McMullen R, Baumann MJ, McCabe LR. Hydroxyapatite accelerates differentiation and suppresses growth of MC3T3-E1 osteoblasts. *Journal of biomedical materials research* 2003(67A):1196–1204.
178. Rabionet M, Toque JA, Ide-Ektessabi A. In vitro evaluation of osteoblast-like cells on hydroxyapatite-coated porous stainless steel implants by synchrotron radiation x-ray fluorescence. *X-Ray Spectrometry* 2009(38):278–282.
179. Rasband WS. ImageJ, U.S. National Institutes of Health, Bethesda, Maryland, USA, <http://rsb.info.nih.gov/ij/>, 1997-2009.
180. Eshwar MC, Subrahmanyam B. Extraction-photometric determination of silver by means of 1-(2-pyriylazo)-2-naphtol. *Zhurnal Analiticheskoi Khimii*. 1976; 31(12):2319-2322.
181. Dean, R. B. and Dixon, W. J. Simplified statistics for small numbers of observations. *Analytical Chemistry* 1951;23, 636–638.

182. Bai X, More K, Rouleau CM, Rabiei A. Functionally Graded Hydroxyapatite Coatings Doped with Antibacterial Components. *Acta Biomaterialia* 2010;6:2264–2273.
183. Yamamoto A, Honma R, Sumita M. Cytotoxicity evaluation of 43 metal salts using murine fibroblasts and osteoblastic cells. *J Biomed. Mater. Res. A*.1998;39, 331-340.
184. Drake PL, Hazelwood KJ. Exposure-Related Health Effects of Silver and Silver Compounds: A Review *Ann Occup Hyg* 2005(49);7: 575-585.
185. Deligianni DD, Katsala ND, Koutsoukos PG, Missirlis YF. Effect of surface roughness of hydroxyapatite on human bone marrow cell adhesion, proliferation, differentiation and detachment strength. *Biomaterials* 2001;22(1):87-96.
186. Ergun C, Liu HN, Halloran JW, Webster TJ. Increased osteoblast adhesion on nanograined hydroxyapatite and tricalcium phosphate containing calcium titanate. *Journal of Biomedical Materials Research A* 2007;80A(4):990-997.
187. Amaya C, Caicedo J, Bejarano G, Escobedo CA, Munoz-Saldana J, Zambrano G, Prieto P. Influence of bias voltage on the crystallographic orientation and morphology of sputter deposited yttria stabilized zirconia (YSZ) thin films. *Physica Status Solidi; Current Topics in Solid State Physics* 2007(4);11:4288-4293.
188. Kijima T, Tsutsumi M. Preparation and thermal properties of dense polycrystalline oxyhydroxyapatite. *Journal of the American Ceramic Society* 1979;62:455-60.
189. Tsui YC, Doyle C, Clyne TW. Plasma sprayed hydroxyapatite coatings on titanium substrates; Part 1: Mechanical properties and residual stress levels. *Biomaterials* 1998(19);2015-2029.
190. Yang, Y., K.H. Kim, C.M. Agrawal, and J.L. Ong, Influence of post-deposition heating time and the presence of water vapor on sputter-coated calcium phosphate crystallinity. *Journal of Dental Research* 2003(82);10: 833-837.
191. Ong JL, Lucas LC. Auger electron spectroscopy and its use for the characterization of titanium and hydroxyapatite surfaces. *Biomaterials* 1998(19):455–464.

192. Ong JL, Raikar GN, Smoot TM. Properties of calcium phosphate coatings before and after exposure to simulated biological fluid. *Biomaterials* 1997(18):1271–1275.
193. Yang Y, Agrawal CM, Kim K-H, Martin H, Schulz K, Bumgardner JD, Ong JL. Characterization and dissolution behavior of sputtered calcium phosphate coatings after different post deposition heat treatment temperatures. *J Oral Implantol* 2003;24(6):270–7.
194. Hulshoff JEG, van Dijk K, de Ruijter JE, Rietveld FJR, Ginsel LA, Jansen JA. Interfacial phenomena: an in vitro study of the effect of calcium phosphate (Ca-P) ceramic on bone formation. *J Biomed Mater Res* 1998;40:464–74.
195. Zalm PC. Quantitative sputtering. In: Cuomo JJ, Rossnagel SM, Kaufman HR, editors. *Handbook of ion beam processing technology*. Park Ridge, NJ: Noyes Publications; 1989;78–111.
196. van Dijk K, Schaeken HG, Wolke JGC, Jansen JA. Influence of annealing temperature on RF magnetron sputtered calcium phosphate coatings. *Biomaterials* 1996;17:405–10.